

DEVELOPMENT AND EVALUATION OF CARBON DIOXIDE SENSORS FOR BUILDING APPLICATIONS

by

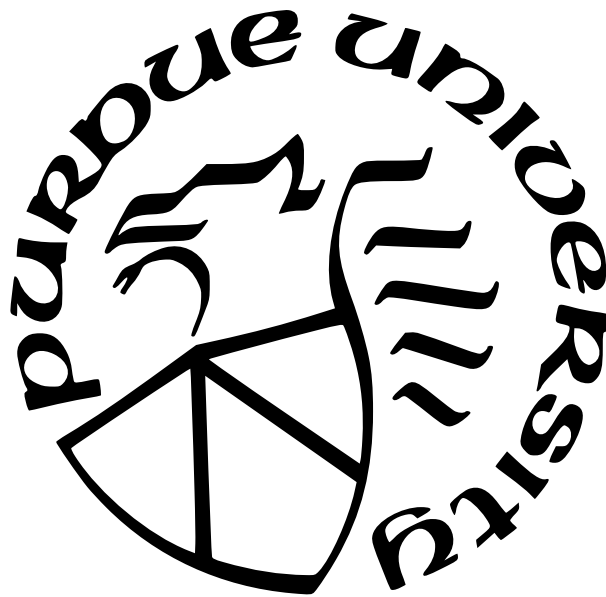
Zachary A. Siefker

A Dissertation

Submitted to the Faculty of Purdue University

In Partial Fulfillment of the Requirements for the degree of

Doctor of Philosophy



School of Mechanical Engineering

West Lafayette, Indiana

May 2022

**THE PURDUE UNIVERSITY GRADUATE SCHOOL
STATEMENT OF COMMITTEE APPROVAL**

Dr. Jeffrey F. Rhoads, Co-Chair

School of Mechanical Engineering

Dr. James E. Braun, Co-Chair

School of Mechanical Engineering

Dr. George T.-C. Chiu

School of Mechanical Engineering

Dr. Bryan W. Boudouris

Davidson School of Chemical Engineering

Approved by:

Dr. Nicole Key

ACKNOWLEDGMENTS

This dissertation would not be possible without the support and contributions of many people. I would like to thank my committee Dr. Jeffrey F. Rhoads, Dr. James E. Braun, Dr. George T.-C. Chiu, and Dr. Bryan W. Boudouris for their support and guidance. Each committee member made significant contributions to this research and my personal development, which will forever be appreciated.

Thank you to my family and friends for your support and encouragement. In particular, I'd like to thank my partner, Dr. Allison K. Murray, for her endless love and support. As well, I'd like to thank many of my research mentors, collaborators, and friends: Dr. Nikhil Bajaj, Abhi Boyina, Nikhil Carniero, Carsten Flores-Hansen, Eugenio Frias-Miranda, John Hodul, and Joseph Meseke.

The information, data, or work presented herein was funded in part by the Advanced Research Projects Agency-Energy (ARPA-E), U.S. Department of Energy, under Award Number DE-AR0000943. The views and opinions of authors expressed herein do not necessarily state or reflect those of the United States Government or any agency thereof. Additionally, this work was funded, in part, by the Center for High Performance Buildings at Purdue University.

TABLE OF CONTENTS

LIST OF TABLES	7
LIST OF FIGURES	8
ABSTRACT	14
1 INTRODUCTION	15
1.1 CO ₂ Sensing in Building Applications	15
1.2 Low-Cost Commercial CO ₂ Sensors	16
1.3 Polymer-Functionalized Sorption-Based CO ₂ Sensors	17
1.4 Overview of the Dissertation	18
2 A CARBON NANOTUBE-FUNCTIONAL POLYMER COMPOSITE FILM FOR LOW-POWER INDOOR CO ₂ MONITORING	20
2.1 Introduction	20
2.2 Materials and Methods	22
2.2.1 Material Sourcing	22
2.2.2 Device Fabrication	22
2.2.3 Testing Procedure	23
2.3 Results and Discussion	25
2.3.1 Dynamic Range of Sensor	25
2.3.2 Sensing in the Built Environment	27
2.3.3 Sensor Responsiveness	30
2.3.4 Sensor Selectivity	31
2.3.5 Comparison with Other CO ₂ Sensors	31
3 A RESONANT CO ₂ SENSOR FUNCTIONALIZED WITH A POLYMERIZED IONIC LIQUID	34
3.1 Introduction	34
3.2 Material Synthesis	35

3.3	Device Fabrication	36
3.4	Testing Procedure	37
3.5	Results and Discussion	39
4	MANIPULATING POLYMER COMPOSITION TO CREATE LOW-COST, HIGH-FIDELITY SENSORS FOR INDOOR CO ₂ MONITORING	42
4.1	Introduction	42
4.2	Experimental Methods	45
4.2.1	Materials	45
4.2.2	General Methods	45
4.2.3	Device Testing	46
4.2.4	Device Instrumentation	48
4.2.5	Device Functionalization	48
4.3	Results	49
4.3.1	Sensor Response and Dynamic Range	49
4.3.2	Performance in Indoor Environments	50
4.3.3	Sensor Selectivity	53
4.3.4	Polymer Film Properties Impact CO ₂ Detection	53
4.3.5	PEO Hydrophilic Properties Further Enhance CO ₂ Detection	57
4.4	Discussion	59
5	SORPTION KINETICS OF POLY(ETHYLENEIMINE)-POLY(ETHYLENE OXIDE) BLENDS AND THE IMPLICATION FOR LOW-COST, SMALL-SCALE CO ₂ SENSORS	61
5.1	Introduction	61
5.2	Experimental Methods	63
5.2.1	Materials	63
5.2.2	General Methods	63
5.2.3	Experimental Adsorption Apparatus and Procedure	64
5.2.4	Device Fabrication	65
5.2.5	Adsorbed Mass and Resonance Frequency Correlation	66

5.3	Results and Discussion	66
5.3.1	Characterization of Polymer Blend	66
5.3.2	CO ₂ Adsorption-Desorption Profiles	69
5.3.3	Analysis of CO ₂ Sorption Kinetics	72
6	IMPLEMENTING CO ₂ SENSORS IN THE BUILT ENVIRONMENT AND DI- RECTIONS FOR FUTURE WORK	76
6.1	Introduction	76
6.2	Placement of CO ₂ Sensors in the Built Environment	77
6.3	Full-Scale Sensor Testing	79
6.4	Occupant Localization via CO ₂ Sensor Networks	82
6.4.1	Source Localization Approach	82
6.4.2	Experimental Procedure	83
6.4.3	Event Window and Data Preparation	85
6.4.4	Experimental Results	86
6.4.5	Classification Modeling	88
6.4.6	Limitations	89
6.4.7	Discussion	89
7	SUMMARY AND CONCLUSIONS	92
	REFERENCES	95
	VITA	113

LIST OF TABLES

2.1	A comparative study among other PEI-based CO ₂ sensors	33
6.1	The average time to respond to a CO ₂ release event, relative to the first sensor that responded. The time response is defined as a 25 ppm rise above baseline conditions.	87

LIST OF FIGURES

2.1	Step-by-step device preparation including a CNT bath in chlorosulfonic acid, the formation and delamination of a CNT thin-film, the transfer of the CNT thin film to the test substrate, and the polymer casting to complete the composite sensor. The substrate presented shows one set of electrodes with the CNT thin film and a separate set of bare electrodes that are intentionally not covered with CNTs for visual demonstration purposes.	23
2.2	The benchtop testing system for the chemiresistive sensors. An inline flow distribution system fed the test chamber via a side port. The flow exited via a hole in the PCB substrate. Resistance was measured across the functionalized electrodes of the PCB substrate using benchtop DMMs and was recorded via LabVIEW. .	24
2.3	Sensor change in resistance (blue line; left y-axis) when exposed to increased levels of CO ₂ (shaded red bars; right y-axis) in a background of air (78% nitrogen, 21% oxygen, and 0.12% carbon dioxide) and a background of pure nitrogen. A steady background of 40% relative humidity is maintained. The change in resistance with a background of air is offset for visual clarity by 4 Ω	25
2.4	Quantified sensor response and interpolated sensitivity to CO ₂ concentrations ranging from 450-20,000 ppm on a background of 400 ppm CO ₂ and 40% relative humidity (Inset: response at 450 ppm on a background of 400 ppm).	26
2.5	Psychrometric chart highlighting the range of environmental conditions for CO ₂ sensor testing. This region spans across the 0.5 clo and 1.0 clo comfort zones stipulated by ANSI/ASHRAE Standard 55-2010 [98] (Inset: A time series representation of the sensor response to CO ₂ at a central test condition of 24 °C and 50% RH).	27
2.6	Sensor response showing the total resistance change for a range of temperature and relative humidity, typical of indoor air conditions.	29
2.7	Sensor rate of change in resistance at specified temperature and relative humidity points.	29
2.8	Sensor response times and recovery times at CO ₂ concentrations relevant to indoor air monitoring and at the center of the comfort zone (24 °C and 50% RH).	30
2.9	Sensor response when exposed to CO ₂ , acetone, methanol, ethanol, and CO in a background of nitrogen at 40% relative humidity. The sensor was exposed to 500 second pulses at 500 ppm concentration of CO ₂ and the selected confounding species. The sensor displayed selectivity to CO ₂ as compared to the tested confounding species.	32
3.1	Synthesis of the imidazolium-based PIL, PMVBI-PF ₆	36

3.2	The Pierce oscillator topology used for each resonant mass sensor circuit, with the Kyocera CX3225 resonant element shown after the package cap has been removed.	37
3.3	Schematic of gas distribution system and test chamber for PIL functionalized resonator testing.	38
3.4	A representative oscillator response to a high concentration test range (4,000 to 100,000 ppm) with stepped CO ₂ concentration changes for a functionalized oscillator and a reference channel. This concentration range corresponds to applications, such as industrial processes and human respiration monitoring. . . .	39
3.5	(left) Sensor response (frequency shifts) over the 1,000 ppm to 100,000 ppm range, showing relatively linear response in the high concentration (10,000 ppm to 100,000 ppm) range and (right) some deviation from linear response in the low concentration (less than 10000 ppm) range	40
3.6	A representative oscillator response to a lower concentration test range (100 ppm) with stepped CO ₂ concentration changes for a functionalized oscillator and a reference channel. This accuracy range corresponds to concentrations relevant in building occupancy and indoor air quality monitoring.	40
4.1	(a) Schematic of the gas distribution system used for sensor testing. Mass flow controllers (MFCs) modulated supply gases to the test chamber containing functionalized oscillators. Bubblers connected to a MFC were used to moderate distractant analytes and humidity levels inside the testing chamber. A frequency counter, executed on a MyRIO FPGA monitored the frequency of each oscillator in parallel. (b) A schematic of the Pierce oscillator used. The resonant element, outlined by the red box, is shown on the left of the circuit diagram. The remainder of the oscillator circuit, which is contained on the instrumentation board, is outlined by the blue box. This portion of the diagram contains two load capacitors (C_1 and C_2), a feedback resistor (R_1), and an isolation resistor (R_2). A series of inverters between the supply voltage (V_{cc}) and the output voltage (V_{out}) are used to square-off the oscillator output signal to facilitate frequency counting. (c) A single packaged resonant element shown on a US quarter for scale. (d) An exposed quartz crystal resonant element. (e) A resonant mass sensing system with 16 Pierce oscillators. A resonator board (left) containing 16 resonant elements is shown offset from the instrumentation board (right) which completes the Pierce oscillator circuit.	47

4.2	Sensor response to CO ₂ shown as a frequency shift of the resonant element. (a) Sensor response to CO ₂ over time with a background of nitrogen. The resonant frequency shift response is indicated by the blue line (left vertical axis) and the red bars indicate when CO ₂ is present (right vertical axis). (b) Sensor response to CO ₂ over time with a background of air. The resonant frequency shift response is indicated by the blue line (left vertical axis), and the red bars indicate when CO ₂ is present (right vertical axis). The use of air brought the baseline CO ₂ concentration to 1,200 ppm. (c) Total frequency shift of the device after 1 hour of CO ₂ at specified concentrations. Regardless of the baseline conditions, a similar linear response is obtained by the sensor, as demonstrated by the linear regression fit. (d) The dynamic range of the sensor is shown by plotting the resonant frequency shift in response to 1 hour of CO ₂ in a background of nitrogen. For comparison, outdoor air CO ₂ concentrations [142] are indicated by the solid blue line, healthy indoor air CO ₂ levels [8] are indicated by the dashed green line, poor indoor air CO ₂ levels [8], [143] are indicated by the dashed orange line, and toxic CO ₂ levels [141] are indicated by the dashed red line. Additionally, the sensitivity (indicated by the change in frequency per change in CO ₂ concentration, $\frac{\partial f}{\partial c}$) is shown at both low and high concentrations.	51
4.3	(a) Psychrometric chart defining the ‘Comfort Zone’ air temperature and humidity range, as defined by the engineering association, ASHRAE. Testing was performed across this region to simulate environmental conditions expected in high performance buildings. (b) Frequency response of devices functionalized with PEI only, and a 3:1 PEO:PEI blend ranging from 0 to 80% relative humidity (RH). Tests were performed holding temperature at 24 °C. (c) Sensor response to CO ₂ while varying temperature from 22–26 °C and relative humidity from 10-80% to cover the indoor air comfort zones [98]. A baseline condition of 400 ppm CO ₂ in nitrogen was used to simulate outdoor air conditions and a linear response is obtained at each condition, as demonstrated by the linear regression fits. (d) The rate of change in frequency shift after each increase in CO ₂ concentration from a background of 400 ppm. A similar linear response is obtained at each condition, as demonstrated by the linear regression fits.	52
4.4	Sensor response to 1,000 ppm pulses of CO ₂ and various distractants. (a) Zoomed frequency shift response of a sensor in response to CO ₂ in the presence of acetone. The time series data shows 30 minute pulses of CO ₂ with a background of nitrogen, followed by pulses of acetone, pulses of CO ₂ and acetone together, and finally pulses of CO ₂ with a constant background of acetone. (b) Frequency shift responses of a sensor in the presence of various interfering gas analytes.	54
4.5	(a) and (b) SEM images of a PEI film after being drop cast onto a silicon wafer and dried for 12 hours under vacuum. The two panels show the same film at two different magnification levels. (c) and (d) SEM images of a 1:1 PEO:PEI (by weight) blend film after being drop cast onto a silicon wafer and dried for 12 hours under vacuum. The two panels show the same film at two different magnification levels.	55

4.6	(a) SEM images of a 3:1 PEO:PEI blend film. Both images shown are of the same film but in different sections and zoom locations. (b) AFM images of a 3:1 PEO:PEI blend films. (c) XRD patterns of PEO, 3:1 PEO:PEI blend, 2.5:1.5 PEO:PEI blend, 1:1 PEO:PEI blend, 1:3 PEO:PEI blend, and PEI only films. (d) DMA of a 2.5:1.5 and 3:1 PEO:PEI, and PEO only blend films.	56
4.7	(a) FTIR spectra of a 1:1 PEO:PEI polymer blend film after being annealed and dried under vacuum to remove any excess solvent and exposed to 40% relative humidity at room temperature for up to 5 hours. (b) FTIR spectra of a 3:1 PEO:PEI polymer blend film after being annealed and dried under vacuum to remove any excess solvent and exposed to 40% relative humidity at room temperature for up to 5 hours. The broad OH stretch is observed at 3300 cm^{-1}	58
4.8	Proposed mechanisms of CO_2 capture by PEI with and without the presence of water. The intermediate step indicated in red is the key step in this reaction process. Without the presence of water the reaction does not proceed and the amine does not become accessible. With the presence of water the reaction can proceed forward due to a free amine which can capture more CO_2	59
5.1	Schematic of the experimental setup used for sensor characterization. The mass flow controllers (MFCs) modulated supply gases to the test chamber containing the functionalized resonators. A recirculating heater/chiller and a thermal wrap were used to regulate the temperature of the test chamber at the reported conditions.	65
5.2	SEM images of a 3:1 PEO:PEI blend film. (a) Room temperature image of the polymer film. These images are highlighting the micron-sized pores formed in the polymer matrix. All of the images shown are of the same film but in different sections and locations. (b) A polymer film exposed to temperature greater than 343 K, isotherm for 15 minutes, and then imaged. These images are highlighting the melting of the polymer film and the loss of porous structure. All of the images shown are of the same film but in different sections and locations.	67
5.3	(a) FTIR spectra of PEI, PEO, and 3:1 PEO:PEI polymer films. Dashed lines highlight the spectrum peaks at 3270 cm^{-1} , 2880 cm^{-1} , 1580 cm^{-1} , 1475 cm^{-1} , 1380 cm^{-1} , 1310 cm^{-1} , and 1090 cm^{-1} , which occur in the 3:1 PEO:PEI polymer sample corresponding to the peaks in PEO and PEI. (b) XRD patterns of PEI, PEO, 3:1 PEO:PEI blend films. Highlighting the crystal structure of PEO expressed in the 3:1 PEO:PEI polymer film. (c) DSC heating and cooling traces of PEO and 3:1 PEO:PEI polymer films, highlighting that PEO has a T_m of 338.15 K and T_c of 317.15 K while a 3:1 PEO:PEI film has a T_m of 331.15 K and a T_c of 310.15 K. Upon integration, 3:1 PEO:PEI heating and cooling peaks were 70% of the PEO peaks area, respectively.	68
5.4	Representative time-series data showing the response of 3:1 PEO:PEI functionalized resonator to concentrations of CO_2 between 0% and 1% in a 325 K environment.	70

5.5	(a) CO ₂ adsorption-desorption cycles at various temperatures for a 3:1 PEO:PEI functionalized resonator in response to 1 hour on/off pulses of CO ₂ at a concentration of 0.84%. (b) The mean resonance frequency shift after 1 hour of CO ₂ exposure at various concentrations for a 3:1 PEO:PEI functionalized resonator. The error bars represent one standard deviation of the data from the average value.	71
5.6	(a) CO ₂ adsorption-desorption cycles at various temperatures for a PEI functionalized resonator in response to 1 hour on/off pulses of CO ₂ at a concentration of 0.84%. (b) The mean resonance frequency shift after 1 hour of CO ₂ exposure at various concentrations for a PEI-functionalized resonator. The error bars represent one standard deviation of the data from the average value.	71
5.7	(a) A fit of the Langmuir adsorption isotherm (Equation 5.6) to frequency data of a 3:1 PEO:PEI functionalized resonator at a concentration of 0.84% CO ₂ and in a 300 K environment. (b) Fit to calculated k_{obs} for a 3:1 PEO:PEI functionalized resonator in a 300 K environment. (c) Fitted relationship between k_{obs} and CO ₂ concentration for pristine PEI and a 3:1 PEO:PEI blend for temperatures ranging from 300 K to 325 K. (d) Calculated Gibbs free energy at each temperature condition for pristine PEI and a 3:1 PEO:PEI blend.	74
5.8	Arrhenius plot showing (a) k_a and (b) k_d for PEI alone and a 3:1 PEO:PEI functionalized resonator. Notably, k_a is relatively constant while k_d increases with increasing temperature. Thus, the decrease in response can partly be attributed to a faster desorption rate at higher temperatures.	75
6.1	Indoor air quality chamber (IAQC) utilized for full-scale sensor testing.	80
6.2	(a) A zoomed out and (b) zoomed in picture of the prototype CO ₂ sensing system and commercial CO ₂ sensors in the IAQC. A paper filter was placed over the prototype sensing elements to serve as a protective dust shield.	80
6.3	Comparison of prototype sensor with commercial CO ₂ sensors in the IAQC. The left axis and blue line correspond to the frequency shift of the prototype CO ₂ sensor. The right axis and red lines indicate the measured CO ₂ concentration of two commercial CO ₂ sensors that were co-located with the prototype sensor.	81
6.4	(a) A two-stage logical approach to gas source isolation. (b) A disturbance observer to estimate CO ₂ disturbances in a closed room. (c) Classification algorithms to determine a gas source location within the enclosed space.	84
6.5	(a) Commercial IoT air quality sensors installed in the environmental test chamber for propagation modeling and source isolation experiments. (b) A top-down view of sensor placement within the environmental test chamber.	85
6.6	Time series representation of CO ₂ injected into two different locations of the IAQC. As annotated in the figure, these pulses show CO ₂ being released in the upstream supply duct (external source) and in quadrant Q3. A sliding window approach was utilized to identify a gas source release and to bound the data for feature extraction.	88

6.7	Feature space representing the mean CO ₂ concentration at sensors S4 and S8 in a (a) 30-min, (b) 15-min, (c) 5-min, and (d) 2-min time window. As the length of the time window for feature extraction decreases, the cross-validated model accuracy diminishes while utilizing a kNN (k=1) classification approach.	90
-----	---	----

ABSTRACT

Current global efforts in building information research include the development of low-cost, high-reliability sensing systems capable of quantifying metrics such as human occupancy, indoor environmental quality, and building system dynamics. Such information is of high value for model development, building energy management, and improving occupant comfort. Further, indoor air quality (IAQ) has been a growing concern in recent years, only to be expedited by the COVID-19 pandemic. A common provisional measure for IAQ is carbon dioxide (CO_2), which is regularly used to inform the ventilation control of buildings. However, few commercially available sensors exist that can reliably measure CO_2 while being low cost, exhibiting low power consumption, and being easily deployable for use in applications such as occupancy monitoring.

This work presents research related to the initial development and evaluation of low-cost, stable, and easily deployable sensors for monitoring indoor CO_2 levels in buildings. Two different types of sensors are presented that have the potential to perform as well as current commercially available CO_2 sensing technologies, at significantly lower costs. The first is a chemiresistive sensor that is fabricated using a carbon nanotube thin film in conjunction with a blend of branched poly(ethylenimine) (PEI) and poly(ethylene glycol) (PEG), which serves as a CO_2 absorbing layer. The second is a resonant mass sensor, functionalized with similar polymer-based materials, including a blend of PEI and poly(ethylene oxide) (PEO). Prototype sensors were assessed in a bench-top environmental test chamber which varied temperatures, relative humidity levels, CO_2 concentrations, as well as other gas constituents to simulate typical and extreme indoor conditions. The results indicate that the proposed system could ultimately serve as an attractive alternative to commercial CO_2 sensors that are currently available.

1. INTRODUCTION

1.1 CO₂ Sensing in Building Applications

In the United States, buildings account for nearly 40% of total energy consumption [1]. Although the average American spends nearly 90% of their time indoors, individual spaces in buildings typically have low or no occupancy much of the time [2]. Thus, there is significant opportunity for reducing energy use by decreasing ventilation rates and adjusting thermostat temperatures according to measured occupancy. Currently, there is a global effort in building-information research to develop low-cost, high-reliability sensing systems, capable of quantifying metrics such as human occupancy, indoor air quality (IAQ), and building system dynamics. Such information is of high value for model development, building energy management, and improving occupant comfort. In particular, a promising technology for improving sensing systems in smart buildings is low-cost and easily deployable CO₂ sensors.

CO₂ concentration is a common surrogate measure for both human occupancy and IAQ monitoring [3]–[7]. In the process of metabolizing food, humans consume oxygen and expel CO₂. The rate at which oxygen is consumed and CO₂ is generated depends on physical activity. As such, CO₂ can be an indicator of both occupancy and overall activity within a space. Further, since baseline CO₂ concentrations are much lower than baseline oxygen concentrations (0.0004% vs 21% respectively), an environmental change in CO₂ is much more significant than an environmental change in oxygen [8].

Additionally, CO₂ monitoring is important from an IAQ perspective. CO₂ concentrations in buildings can range from those seen in pristine environmental conditions (i.e., ~400 ppm) to 3,000 ppm, depending on the occupancy of the confined space [9], [10]. Moreover, CO₂ exposure at as low of a concentration as 1,000 ppm, has been shown to affect cognitive performance, including decision making and problem resolution [11]–[13]. Thus, appropriate indoor air quality monitoring and building ventilation is extremely important for ensuring healthy buildings.

As the Internet of Things (IoT) technologies begin to translate into the buildings sector, new opportunities are arising with the advent of distributed sensing networks to improve building operation [14]. For example, some studies have shown the possibility of estimating

building air leakage by monitoring CO₂ concentration decay patterns [15], [16]. Others have suggested using CO₂ sensing for occupancy detection to provide localized comfort control [17]–[19]. Thus, there is a need for low-cost and easily deployable sensors for monitoring indoor CO₂ levels in buildings. There are many successful commercial CO₂ sensors on the market; however, few were designed with building systems in mind or show long-term reliability while remaining low cost and low power.

1.2 Low-Cost Commercial CO₂ Sensors

Considering low-cost CO₂ sensors, metal-oxide and nondispersive infrared (NDIR) sensors, are among the most common commercially available technologies. Metal-oxide sensors operate by measuring a change in the resistance of a metal oxide film, due to the adsorption of a target analyte. This change may result in an increase or decrease in resistance, depending on the target analyte and the sensing material being used. Since CO₂ is an oxidizing gas, an n-type material, such as the tin dioxide used by Mizuno *et al.*, results in an increased material resistance in the presence of CO₂ [20]. Alternatively, works such as Chapelle *et al.*, which used a p-type material (copper oxide and spinel ferrite) resulted in a decreased resistance in the presence of CO₂ [21]. Metal-oxide sensors are a relatively low-cost option for CO₂ monitoring and thus, material enhancements for improved sensing performance continues to be a topic of research [22]–[26]. However, accuracy below 2,000 ppm tends to be poor, which is insufficient for most indoor CO₂ monitoring applications [27].

For applications below 2,000 ppm, such as indoor air monitoring, NDIR sensors are most common. NDIR sensors operate based on principles of molecular spectroscopy and are commonly used for gas sensing applications. Most gas molecules will absorb infrared light at specific wavelengths. In the case of CO₂, the 4.26 μm absorption band is the strongest and most selective relative to other air constituents. Thus, attenuation of this wavelength is measured to determine CO₂ concentration according to the Beer-Lambert law [28]. The main components of an NDIR sensor include an infrared light source, an infrared detector, and an optical bandpass filter which limits infrared intensity outside the molecule-specific wavelength. The infrared light is directed toward the detector with sample gas filling the

space in between. Since the attenuation of infrared light is proportional to the density of CO₂ molecules in this path, temperature and pressure corrections must be applied for accurate measurement of CO₂ concentration.

NDIR sensors for CO₂ sensing applications have been well documented in the literature and continue to be improved [29]–[33]. Further, their use in building applications, such as indoor air quality monitoring and demand-controlled ventilation, have been demonstrated extensively [34]–[39]. However, even though NDIR sensors have proven successful in several building applications, they have also fallen short in many regards. For example, several studies have shown that commercial NDIR CO₂ sensors are often prone to error when used for indoor air monitoring [40]–[43]. In addition, though still considered low-cost, these sensors typically market for more than \$100; which is a non-trivial cost when considering the number of sample points being selected within a building. Additionally, NDIR sensor power consumption is on the order of hundreds of mW, making battery-powered, wirelessly-deployed operation challenging. This is due, in large part, to the infrared source inherent to the sensor technology. Recently, improvements have been made with the use of light emitting diodes [44]–[46]. However, given the previously noted limitations, alternative methods for CO₂ measurement should be evaluated.

1.3 Polymer-Functionalized Sorption-Based CO₂ Sensors

Several polymers such as poly(aniline) (PANI), poly(pyrrole) (PPy), polyethersulfone (PES), and poly(3,4-ethylenedioxythiophene) (PEDOT) have shown viability for CO₂ sensing applications [47]–[50]. It is proposed that the sensing mechanism of such polymers is based on the reaction between different types of amines and CO₂ [51]. Similarly, an emerging class of CO₂ sensitive materials exists with the use of polymerized ionic liquids (PIL) [52]–[55]. Specifically, imidazolium-based PILs have shown effective with respect to the reversible uptake and high solubility of CO₂ [56]–[59]. These PILs have shown impressive results in sensing applications where, for example, Willa *et al.* demonstrated a sensor that could detect CO₂ at 150 ppm and ambient conditions [60]. Further, Li *et al.* demonstrated a PIL-based CO₂ sensor with sub-ppb sensitivity [61]. The PIL-wrapped carbon nanotubes in this work

were highly sensitive to CO₂; however, there was also a demonstrated cross-sensitivity to oxygen, which may prove problematic for environmental CO₂ monitoring.

Another polymer that has shown high sensitivity to CO₂ is poly(ethylenimine) (PEI). Several studies have shown PEI to be viable for the capture and storage of CO₂ [62]–[66]. Additionally, PEI has been studied for its use in several sensing applications. For instance, Kiga *et al.* developed a field-effect transistor (FET) gas sensor using PEI in conjunction with carbon nanotubes (CNT) and ionic liquids [67]. This sensor detected CO₂ and NH₃ via a change in the source/drain current flowing through the CNTs. Additionally, Ma *et al.* used PEI as the CO₂ sorbent material in a Fabry-Perot cavity for detection with an optical sensor in the range of 7.6-86.9% [68]. A PEI integrated, all-dielectric photonic crystal slab sensing platform was presented by Chang *et al.*, which had quick response times but saturated at CO₂ levels above 600 ppm [69]. PEI combined with starch has been shown by Star *et al.* to be more effective than PEI alone for developing CO₂ sensitive FETs [70]. PEI and poly(ethylene glycol) (PEG) in a combined polymer system have shown promise for the development of CO₂-sensitive chemiresistive devices, in conjunction with graphene [71]. Similar to the starch in Star *et al.*, hygroscopic PEG was found to improve charge transfer in humid air [70].

1.4 Overview of the Dissertation

The work herein presents the development and evaluation of low-cost CO₂ sensors for building applications. Chapters 2-5 present novel, low-cost and low-power CO₂ sensors based on CO₂ sorption on a functional polymer material. Chapter 2 presents a polymer composite-based chemiresistive CO₂ sensor that leverages a blend of PEI and PEG as the CO₂ absorbing layer. This polymer blend was cast onto a carbon nanotube thin-film, which served as the charge carrying sub-layer. Chapter 3 presents a resonant mass CO₂ sensor functionalized with a PIL (poly(1-methyl-3-(4-vinylbenzyl)-1H-imidazol-3-ium)) hexafluorophosphate [PMVBI-PF₆]). Sensors were functionalized via an inkjet printing technique and the resulting devices could detect as low as 100 ppm CO₂. Using a similar sensing platform, Chapter 4 presents a resonant mass sensor functionalized with a polymer blend of PEI and PEO. A rather simple micropipetting technique was used for functionalization; however,

these sensors were found to detect as low as 5 ppm CO₂. Chapter 5 presents a study which characterizes the temperature-dependent kinetics of the PEI-PEO functionalized resonators presented in Chapter 4. Chapter 6 takes the lessons learned from the benchtop testing performed in Chapters 2-5 and explores full-scale implementation of CO₂ sensors in the built environment, while discussing directions for future work. This includes preliminary data on the sensors developed in Chapter 4 in a room-sized environmental test chamber. Additionally, a demonstration on the basic feasibility of using low-cost, low-power CO₂ sensor networks for occupant localization is presented. Finally, Chapter 7 provides a summary of the work presented herein and key conclusions that can be drawn.

2. A CARBON NANOTUBE-FUNCTIONAL POLYMER COMPOSITE FILM FOR LOW-POWER INDOOR CO₂ MONITORING

The following chapter is reprinted, in part, from Z.A. Siefker *et al.* “A Carbon Nanotube-Functional Polymer Composite Film for Low-Power Indoor CO₂ Monitoring” which appeared in *IEEE Sensors Journal* [72]. This chapter was a shared effort in which Z.A. Siefker designed, conducted, and analyzed experiments and data for the sensing system. N. Bajaj and A. Boyina assisted in the conduction of the sensing experiments. X. Zhao designed, conducted, and analyzed experiments associated with the materials preparation, performance, and characterization. J.E. Braun, G.T. Chiu, B.W. Boudouris, and J.F. Rhoads conceived the project, designed experiments, and directed the research.

2.1 Introduction

With the the onset of the COVID-19 pandemic, indoor air quality (IAQ) has been a source of increased concern in the built environment [73]–[75]. Indoor air pollutants such as viruses, molds [76], [77], volatile organic compounds (VOC) [78], [79], and carbon dioxide (CO₂) [80]–[82] gas can be harmful to occupants. Further, poor IAQ has been shown to reduce occupant performance and productivity [83]–[85]. CO₂ is commonly monitored in building heating, ventilation, and air conditioning (HVAC) systems as a proxy measure of IAQ [3]–[5], and for the purposes of occupancy monitoring [6], [7]. Reliable and low-power CO₂ sensing is valuable across this and several other application spaces; however, few commercial CO₂ sensors show long-term reliability while remaining low cost and low power.

Considering low-cost CO₂ sensors, metal-oxide and nondispersive infrared (NDIR) sensors, are among the most common commercially available technologies. Metal-oxide sensors are a relatively low-cost option for CO₂ monitoring; however, accuracy below 2,000 ppm tends to be poor [27]. For applications below 2,000 ppm, such as indoor air monitoring, NDIR sensors are most common. However, several studies have shown that commercial NDIR CO₂ sensors are often prone to error [40]–[42]. Additionally, NDIR sensor power consumption is on the order of hundreds of mW, making battery-powered, wirelessly-deployed operation challenging. Such sensors are outside of the range of power consumption generally considered viable for long-term energy harvesting using, for example, indoor photovoltaic

cells [86], [87]. This is due, in large part, to the infrared source inherent to the sensor technology. Recently, improvements have been made with the use of light emitting diodes [44]–[46]. However, given current limitations, alternative sensing modalities should be evaluated.

Poly(ethylenimine) (PEI) has frequently been shown to be viable for the capture and storage of CO₂ [62]–[66]. Further, given its strong affinity to CO₂, PEI has been researched for use in several sensing applications. For instance, Kiga *et al.* developed a field-effect transistor (FET) gas sensor using PEI in conjunction with carbon nanotubes (CNT) and ionic liquids [67]. This sensor detected CO₂ and NH₃ via a change in the source/drain current flowing through the CNTs. Additionally, Ma *et al.* used PEI as the CO₂ sorbent material in a Fabry-Perot cavity for detection with an optical sensor in the range of 7.6–86.9% [68]. In a final example, a PEI integrated, all-dielectric photonic crystal slab sensing platform was presented by Chang *et al.*, which had quick response times but saturated at CO₂ levels above 600 ppm [69]. Other methods in the literature for CO₂ sensing include resonant sensing using microelectromechanical systems (MEMS) [88], [89] and photoacoustic methods [44], [90]. This work considers another class of sensor, chemiresistive sensors, which offer significant promise in low-cost and low-power sensing [91]–[95].

PEI combined with starch has been shown by Star *et al.* to be more effective than PEI alone for developing CO₂ sensitive FETs [70]. PEI and poly(ethylene glycol) (PEG) in a combined polymer system have shown promise for the development of CO₂-sensitive chemiresistive devices, in conjunction with graphene [71]. Similar to the starch in Star *et al.*, hygroscopic PEG was found to improve charge transfer in humid air [71]. Thus, a blend of PEI and PEG was selected as the functional material for this work. This polymer blend was cast onto a CNT thin film and a printed circuit board (PCB) substrate. The CNT film bridged gold-plated electrode pairs, created via low-cost commercial PCB fabrication processes, which provided an alternative to the graphene layers. Prototype sensors were assessed in a bench-top environmental test chamber that simulated typical and extreme indoor environmental conditions. Among all of the test conditions considered, the sensors performed particularly well and gave a clear response to CO₂.

2.2 Materials and Methods

2.2.1 Material Sourcing

CoMoCATTM Signis® SG65i semiconducting single wall carbon nanotubes, chlorosulfonic acid, polyethylene glycol ($M_n = 300 \text{ g mol}^{-1}$) and branched polyethylenimine ($M_n = 10,000 \text{ g mol}^{-1}$) were purchased from Sigma-Aldrich, and the materials were used as received. Commercially-available CNT systems were screened based on manufacturer specifications. In particular, attention was paid to the relative aspect ratios of the CNTs and the amount of residual surfactant and catalysis present in the CNTs. CoMoCATTM CNTs were selected for this particular application due to the relatively long length and relatively low residual impurity levels that were present in these materials.

2.2.2 Device Fabrication

The PCB substrate consisted of 12 gold-plated electrode pairs, created via low-cost commercial PCB fabrication processes. To prepare the CNT thin film sub-layer, 3 mg of CNTs were added to 3 mL of chlorosulfonic acid. The mixture was allowed to stir under inert conditions for 3 days to form a thick solution of CNTs. 20 μL of solution were sandwiched between two glass slides, and the thin films were generated by manually pressing and sliding across the glass slides, in a manner similar to what has been reported previously [96]. To transfer the thin film, the glass slides were gently placed into water to peel the thin film. The free-floating films were deposited onto the PCB substrates by sliding the substrates below the thin film and gently lifting onto pre-patterned electrodes with 150 μm spacing (Figure 2.1). To make the polymer system, 0.2 g of PEI and 0.6 g of PEG were dissolved in 20 g of methanol to generate a solution of 1% of PEI and 3% of PEG. This solution was then diluted by methanol to generate a solution of 0.1% of PEI and 0.3% of PEG. The polymer solution was then cast onto the CNT thin films over the PCB substrates, followed by the removal of methanol by drying for 5 hr in a fume hood.

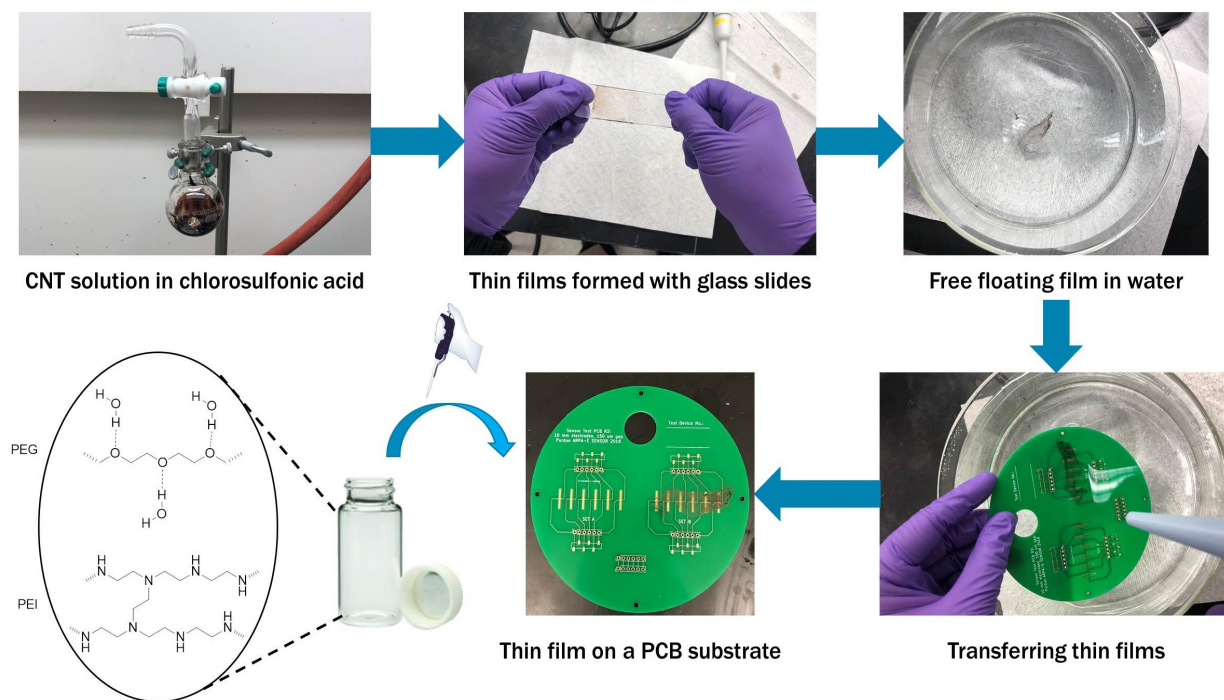


Figure 2.1. Step-by-step device preparation including a CNT bath in chlorosulfonic acid, the formation and delamination of a CNT thin-film, the transfer of the CNT thin film to the test substrate, and the polymer casting to complete the composite sensor. The substrate presented shows one set of electrodes with the CNT thin film and a separate set of bare electrodes that are intentionally not covered with CNTs for visual demonstration purposes.

2.2.3 Testing Procedure

Prototype sensors were tested in a 114 mm-diameter and 20 mm-tall cylindrical aluminum chamber (Figure 2.2). The base was the PCB substrate housing the sensors and the top was a glass window for observation. The 9.5 mm diameter air inlet was located on the aluminum wall and the 9.5 mm diameter air outlet was fixed to the PCB base. The chamber was supplied with gas via an inline flow distribution system with gas sources of nitrogen, air, CO₂, and a mixture of 1% CO₂ balanced with nitrogen. The gas sources were connected to parallel mass flow controllers (MFC, MKS Instruments 1179C) which were used to administer the gas at the reported concentrations. Optional, inline bubblers (ChemGlass, AF-0085) were used to introduce humidity, as well as select confounding vapors. All of the gas lines were connected to a manifold, the output of which was connected directly to the chamber

inlet. Thermoelectric coolers (TEC; Laird CP10-31-05) were attached to the exterior of the test chamber for temperature control of the test environment. A schematic describing the benchtop testing system is shown in Figure 2.2.

Prior to starting each test, the PCB substrate was secured in the testing chamber. At the start of each test, baseline test conditions were developed by flushing the chamber with the carrier gas (air or nitrogen). The chamber was brought to the test-specified temperature and humidity before pulses of CO_2 were introduced. Higher concentration CO_2 pulses were alternated with the reported baseline while maintaining a volumetric flow rate of 500 ccm throughout the test. The sensor resistance was measured using a bench-top digital multimeter (DMM; Keysight 34401A) and a custom LabVIEW program, sampling at a rate of 0.5 Hz.

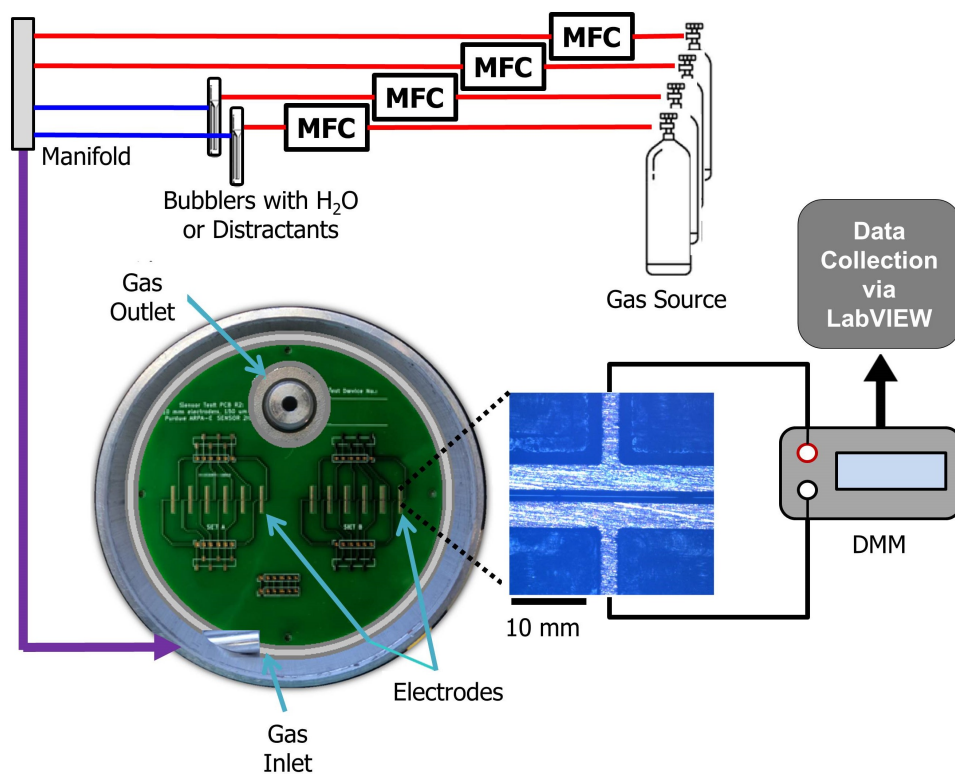


Figure 2.2. The benchtop testing system for the chemiresistive sensors. An inline flow distribution system fed the test chamber via a side port. The flow exited via a hole in the PCB substrate. Resistance was measured across the functionalized electrodes of the PCB substrate using benchtop DMMs and was recorded via LabVIEW.

2.3 Results and Discussion

2.3.1 Dynamic Range of Sensor

Figure 2.3 shows the change in resistance of a device exposed to CO₂ under two different scenarios: one with a background of air and the other with a background of nitrogen. Upon increasing the CO₂ concentration, the device resistance dropped until reaching a steady-state value. When the CO₂ concentration was reduced back to the baseline condition, the device resistance increased and recovered to the initial resistance. The overall response to increased levels of CO₂ is nearly identical with both carrier gases, indicating only a minor influence of non-CO₂ air constituents (e.g., oxygen). As such, nitrogen was favored as the carrier gas to give control of baseline CO₂ levels, which were typically held at 400 ppm as this is the approximate concentration of carbon dioxide in “fresh” outdoor air.

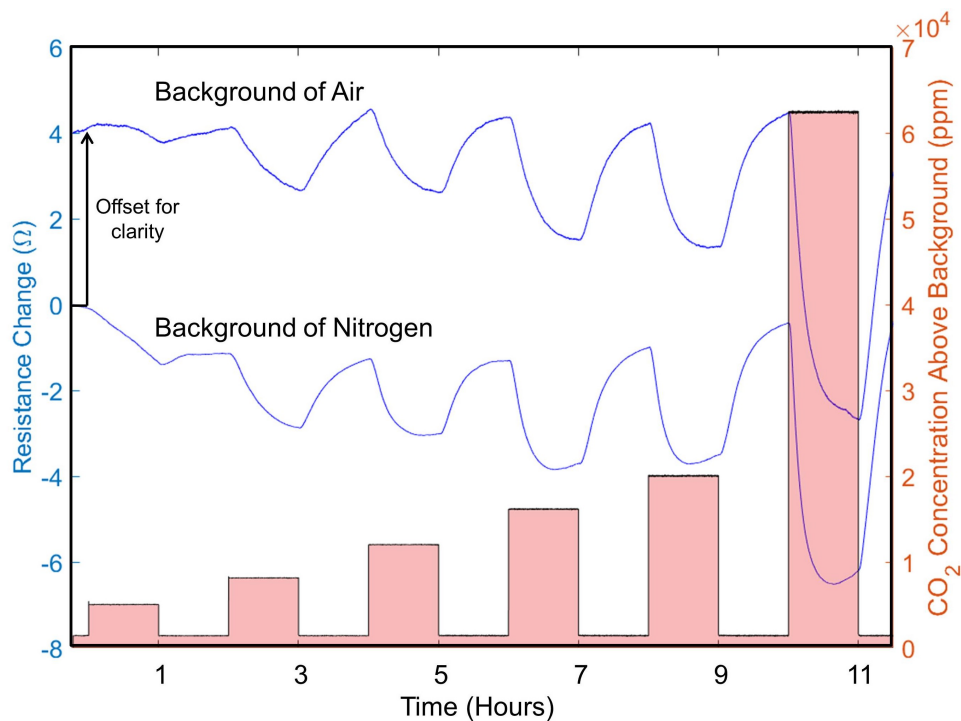


Figure 2.3. Sensor change in resistance (blue line; left y-axis) when exposed to increased levels of CO₂ (shaded red bars; right y-axis) in a background of air (78% nitrogen, 21% oxygen, and 0.12% carbon dioxide) and a background of pure nitrogen. A steady background of 40% relative humidity is maintained. The change in resistance with a background of air is offset for visual clarity by 4 Ω .

Figure 2.4 shows the sensor response to CO₂ in the range of 450-20,000 ppm. Sensor response is defined as

$$\frac{R - R_b}{R_b} \times 100\%, \quad (2.1)$$

where R is the measured electrical resistance, and R_b is the baseline electrical resistance at the start of each 1 hour CO₂ pulse. The range of CO₂ levels includes concentrations relevant to indoor air monitoring (i.e., $\leq 3,000$ ppm [9], [10]) and much higher concentrations, more relevant to industrial applications. As shown by the inset in Figure 2.4, a response is detectable as low as 450 ppm on a background of 400 ppm, which is beyond the resolution necessary for indoor air monitoring. Also noteworthy is that, across this range of concentrations, a relatively linear response is demonstrated with an interpolated sensitivity of $2 \times 10^{-4}\%$ (ppm of CO₂)⁻¹; which is competitive with some commercial NDIR CO₂ sensors [97].

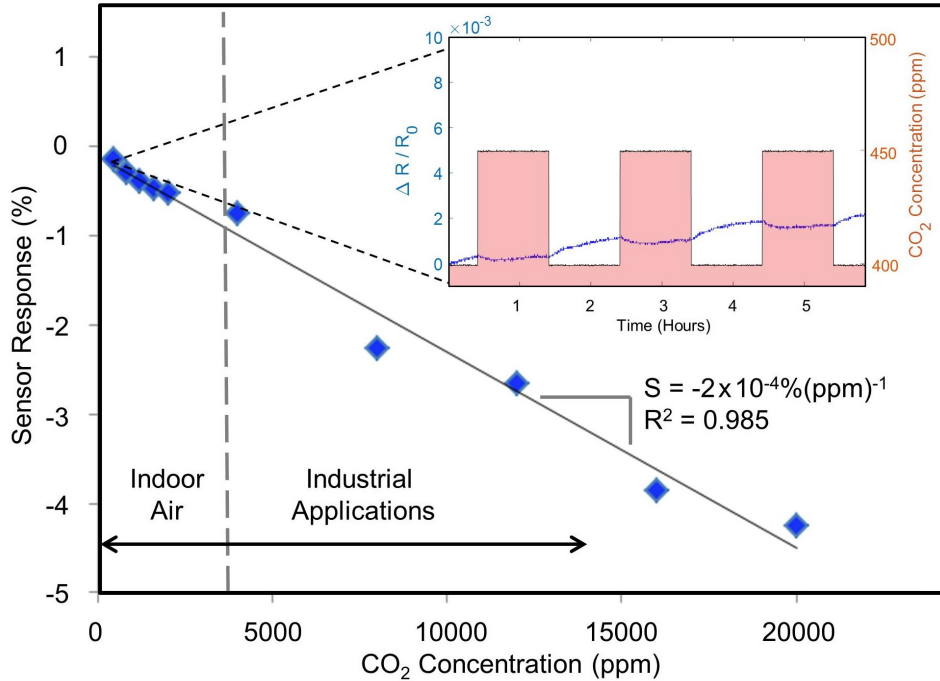


Figure 2.4. Quantified sensor response and interpolated sensitivity to CO₂ concentrations ranging from 450-20,000 ppm on a background of 400 ppm CO₂ and 40% relative humidity (Inset: response at 450 ppm on a background of 400 ppm).

2.3.2 Sensing in the Built Environment

CO₂ sensors for the built environment must operate across a particular range of temperature, humidity, and CO₂ levels. These conditions have been thoroughly studied by the engineering society, ASHRAE, which specializes in advancing the built environment. Therefore, a test region was developed using the 0.5 clo and 1.0 clo comfort zones stipulated by ASHRAE Standard 55 [98]. This region of interest is depicted on the psychrometric chart in Figure 2.5 and spans 22 – 26 °C and from 20%-80% relative humidity (RH). Testing was performed near the extremes of this region, as well as near the center, at CO₂ concentrations between 400 ppm and 2,000 ppm. A background of 400 ppm CO₂ was maintained to simulate fresh outdoor air.

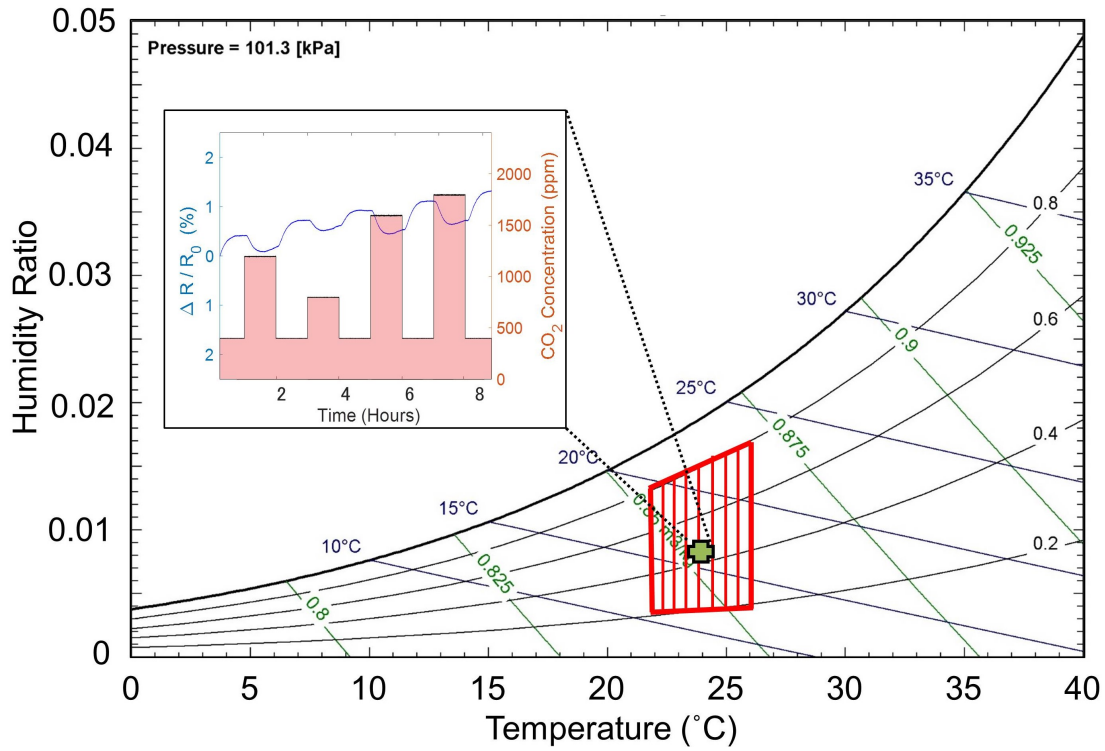


Figure 2.5. Psychrometric chart highlighting the range of environmental conditions for CO₂ sensor testing. This region spans across the 0.5 clo and 1.0 clo comfort zones stipulated by ANSI/ASHRAE Standard 55-2010 [98] (Inset: A time series representation of the sensor response to CO₂ at a central test condition of 24 °C and 50% RH).

The inset of Figure 2.5 represents a snapshot of temporal results at a central test condition of 24 °C and 50% RH which, is a typical indoor condition. The resistance change (line) at each CO₂ concentration (shaded regions) was calculated as

$$\frac{\Delta R}{R_0} = \frac{R - R_0}{R_0} \times 100\%, \quad (2.2)$$

where R is the measured electrical resistance, in ohms, and R_0 is the electrical resistance at the start of the temporal data set. CO₂ was increased to the specified concentrations for 1 hour and likewise reduced back to the 400 ppm baseline condition for 1 hour; however, steady-state conditions were typically achieved after approximately 20 minutes.

Figure 2.6 shows the resistance change at specified CO₂ concentrations for extremes of the temperature/humidity test region as well as at the central test condition. The narrow temperature band had little effect on the sensor response, but the sensitivity increased at higher humidity levels. The increased sensitivity is unsurprising because the reaction of PEI and CO₂ is facilitated by water. This is indicative of more CO₂ molecules interacting with the amino groups present.

As an alternative measure of sensor response, the rate of change in resistance is shown in Figure 2.7. The rate of resistance change was calculated as the change in resistance over the course of 60 seconds or

$$\frac{\Delta R}{\Delta t} = \frac{R_i - R_f}{60 \text{ seconds}} \times 100\%, \quad (2.3)$$

where R_i is the initial electrical resistance, and R_f is the final electrical resistance, 60 seconds after R_i . The data were taken 120 seconds after changing the upstream concentration to allow for gas flow to the test chamber and diffusion within the test chamber.

The total resistance change is slightly more distinct as an indicator of CO₂ concentration than the rate of resistance change. However, these shifts take nearly 20 minutes to reach a steady-state value, which may be an undesirable response time. The rate of change in resistance, however, has a similar degree of accuracy in quantifying CO₂ concentration, and this can be computed within 1 minute of CO₂ concentration change. Therefore, sensor logic

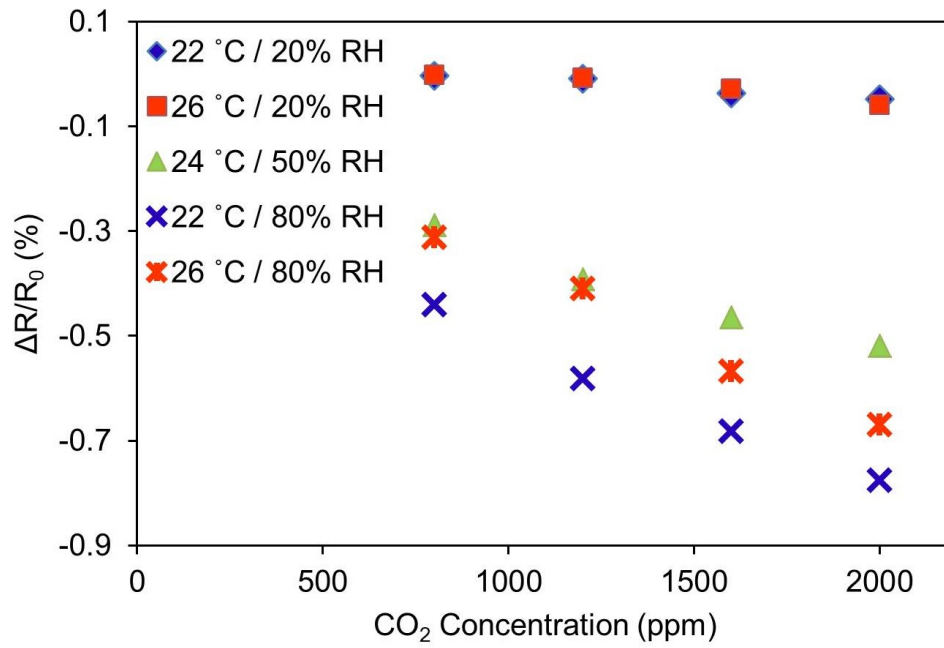


Figure 2.6. Sensor response showing the total resistance change for a range of temperature and relative humidity, typical of indoor air conditions.

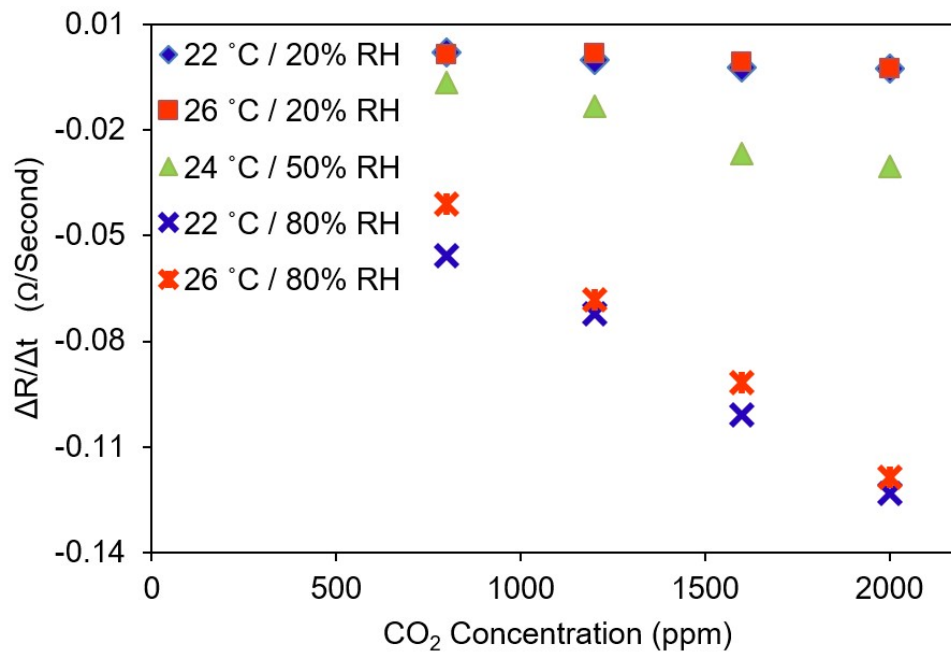


Figure 2.7. Sensor rate of change in resistance at specified temperature and relative humidity points.

may be developed such that the rate of change in resistance will provide a more immediate output and the total change in resistance can be used to maintain long-term accuracy.

2.3.3 Sensor Responsiveness

The response time (τ_{response}) of a CO₂ sensor can be defined as the time to reach 90% of the maximum response after the introduction of additional CO₂. The recovery time (τ_{recovery}) of a CO₂ sensor can be defined as the time to reach 10% of the preceding response after removing CO₂ and returning to baseline conditions. The response and recovery times of the sensor were calculated at a central test condition of 24 °C and 50% RH with a background of nitrogen and 400 ppm CO₂ (Figure 2.8). A slight upward trend is noticeable for both the response and recovery times to increasing CO₂ concentrations. However, for concentrations relevant to indoor CO₂ monitoring (400-2,000 ppm) there is little variance in the response and recovery times independently.

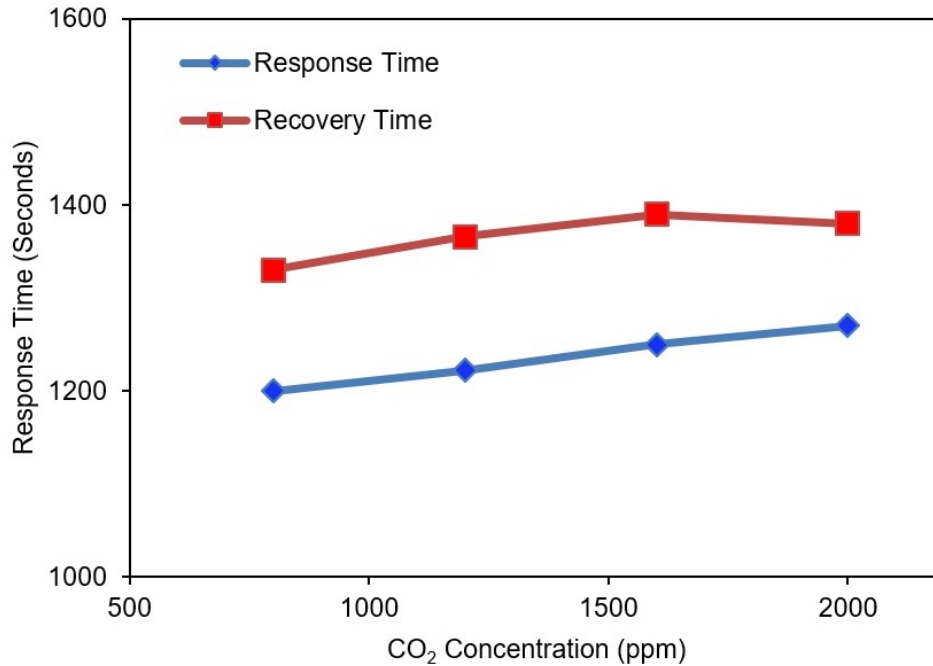


Figure 2.8. Sensor response times and recovery times at CO₂ concentrations relevant to indoor air monitoring and at the center of the comfort zone (24 °C and 50% RH).

Notably, the recovery time of the device is longer ($\sim 10\%$) than the response time, which is consistent with previous studies of CO_2 sorption using PEI [99]. As compared to NDIR sensors, this response time is longer [43]. However, for building applications, such as HVAC control, the rise and decay of CO_2 in a space has time constants on the order of several minutes to hours [100], which makes fast response times less beneficial. Likewise, control action may be taken before the steady state is obtained and the rate of change in resistance may be used as a faster surrogate measure.

2.3.4 Sensor Selectivity

Sensor selectivity to CO_2 is important to prevent false readings in the built environment where VOCs can be prevalent [101], [102]. Prototype sensors were subjected to potentially confounding vapors and gases, including acetone, methanol, ethanol, and carbon monoxide. The sensor is specific to the uptake of CO_2 , as compared to ketones, alcohols, and a simpler oxocarbon. Figure 2.9 shows the sensor response to CO_2 and each of the selected confounding species at a concentration of 500 ppm. Though some drift was present, the sensor responded to pulses of CO_2 , while having a negligible response to the selected confounding species. This result is promising for the application of indoor CO_2 monitoring where VOCs are of growing concern [103].

2.3.5 Comparison with Other CO_2 Sensors

To evaluate the sensing properties of this work, a comparative study with other PEI-based CO_2 sensors is listed in Table 2.1. From Table 2.1, it is noticeable that the PEI-PEG-CNT sensor used in this work exhibits a wide range of functional operating conditions, as well as selectivity. The calculated sensitivity remains competitive among the other PEI-based sensors considered and may be improved by optimizing device geometries. Further advantages are apparent when one considers the low power consumption inherent to many room temperature chemiresistive sensors; however, this measure is often not quantified in the literature for our direct comparison. NDIR sensors are the most common commercially available CO_2 sensors given their accuracy at a relatively low cost. However, the infrared light inherent to

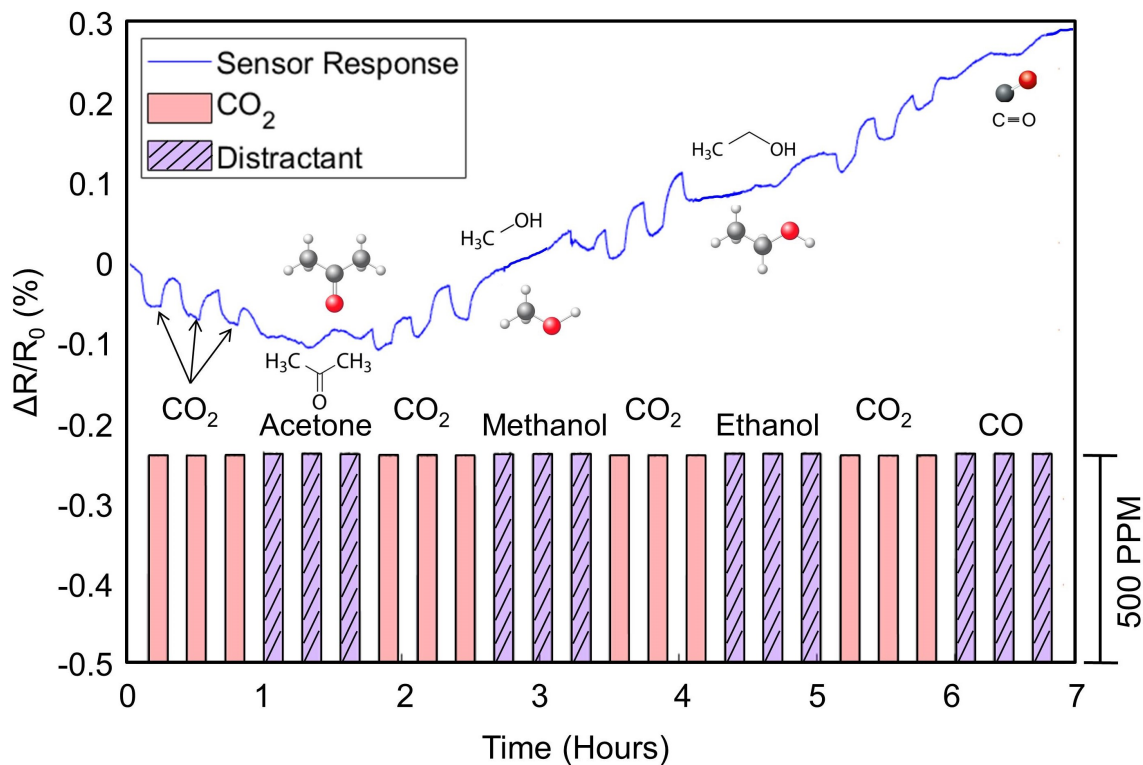


Figure 2.9. Sensor response when exposed to CO₂, acetone, methanol, ethanol, and CO in a background of nitrogen at 40% relative humidity. The sensor was exposed to 500 second pulses at 500 ppm concentration of CO₂ and the selected confounding species. The sensor displayed selectivity to CO₂ as compared to the tested confounding species.

NDIR sensors requires relatively high power consumption and a large sensor footprint, making them difficult to implement in embedded applications. While most commercial NDIR sensors consume hundreds of mW, the chemiresistive devices shown in this work required approximately 100 μ W in their benchtop test setting. Thus, these chemiresistive sensors may serve as a low-power alternative, to be used in wireless sensing, and more densely distributed CO₂ sensor networks in buildings.

Table 2.1. A comparative study among other PEI-based CO₂ sensors

Sensing Materials	Sensor Type	Operating Conditions	Dynamic Range (CO ₂ Concentration)	Sensitivity (ppm ⁻¹)	Selectivity	Reference
PEI/CNT/ EMIM-BF ₄	CNT-FET	Not reported	12-25%	Not reported	Expected to be cross-sensitive with NH ₃	[67]
PEI/PVA	Optical Fabry-Perot interferometer	Room temperature; dry gas	7.6-86.9%	2.81x10 ⁻⁵ nm	Not reported	[68]
PEI	Dielectric photonic crystal slab	Room temperature	20-600 ppm	Not reported	Not reported	[69]
PEI/CNT/ starch	CNT-FET	Room temperature 80% RH	500-100,000 ppm	1x10 ⁻³ %, estimated	Not reported	[70]
PEI/PANI	Chemiresistive	25°C 50% RH	500-5,000 ppm	7.14x10 ⁻³ %	Not sensitive to 50 ppm CO, 5 ppm NH ₃ , 50,000 ppm CH ₄ , and 50 ppb NO ₂	[95]
PEI/PEG/ graphene	Chemiresistive	Room temperature 60% RH	500-5,000 ppm	6.4x10 ⁻³ %	Not reported	[71]
PEI/PEG/ CNT	Chemiresistive	22-26°C 20-80% RH	400-20,000 ppm	2x10 ⁻⁴ %	Not sensitive to 500 ppm acetone, ethanol, methanol, and CO	This work

3. A RESONANT CO₂ SENSOR FUNCTIONALIZED WITH A POLYMERIZED IONIC LIQUID

The following chapter is reprinted, in part, from Z.A. Siefker *et al.* “A Resonant CO₂ Sensor Functionalized with a Polymerized Ionic Liquid” from the proceedings of the *2019 IEEE Sensors Conference* [89]. This chapter was a shared effort in which Z.A. Siefker designed, conducted, and analyzed experiments and data for the sensing system. A.K. Murray assisted in the design of sensing experiments. X. Zhao designed, conducted, and analyzed experiments associated with the materials preparation, performance, and characterization. N. Bajaj designed the oscillator circuit and electronic platform. G.T. Chiu, B.W. Boudouris, and J.F. Rhoads conceived the project, designed experiments, and directed the research.

3.1 Introduction

Carbon dioxide (CO₂) gas is extensively monitored in applications such as in building heating, ventilation, and air conditioning systems to measure indoor air quality, as well as in laboratory and industrial environments to measure process conditions. There are many successful commercial CO₂ sensors on the market, most of which are based upon non-dispersive infrared (NDIR), photoacoustic, electroacoustic, and electrochemical technologies; however, few low-cost and low-power systems are available for monitoring CO₂ at concentrations relevant to advanced building applications. It is imperative that this technical gap is filled in order to make advanced applications (such as building occupancy monitoring) both practical and economical.

One particularly promising approach for CO₂ monitoring is the use of small-scale resonant sensors [104]–[106]. Such devices leverage microscale resonators that have surfaces functionalized for selective binding with various analytes of interest. These resonant elements can be based upon microcantilevers [107]–[109], other microbeam structures [110], bulk acoustic wave (BAW) transducers [104], [111], surface acoustic wave (SAW) transducers, or a number of alternate technologies.

For bulk acoustic model resonators, such as those in quartz crystal microbalances, the added mass due to analyte/sensor interactions (averaged over the active area) induces a shift

in the device’s resonant frequency, which can be estimated by the Sauerbrey equation [111], [112]:

$$\Delta f = \frac{-2f_0^2 \Delta m}{A\sqrt{\rho\mu}}, \quad (3.1)$$

where Δf is the resulting frequency shift, f_0 is the initial resonant frequency of the device, Δm is the mass change, A is the active area, ρ is the density of the resonator material, and μ is the shear modulus. Thus by measuring a given frequency shift, one can measure the presence of a given analyte [113].

Ionic liquids offer utility in the detection of environmental CO₂ concentrations [59], [114], [115] due to the affinity of CO₂ towards many of their ionic moieties. As such, they are interesting candidates for use as functional layers to make the resonant elements selective for CO₂. The sensors developed herein specifically leverage polymerized ionic liquids (PILs) [52], [53], which are polymerized, solid-state variants of the low-viscosity ionic liquids. Compared to the ionic liquids, PILs are mechanically robust enough to be of practical use. The sensing elements used in this work are commercially available 16 MHz BAW quartz crystal timing references. These devices prove to be reliable while remaining low-cost and low-power. After removing the tops of the device packages, the surface of these devices were functionalized with the PILs to enable sensitivity to CO₂ adsorption down to the 100 ppm range. To minimize drift and improve accuracy, reference resonant elements were placed adjacent to the functionalized resonators in order to understand signal drift attributable to extraneous environmental fluctuations, such as temperature variations.

3.2 Material Synthesis

A PIL was synthesized according to the reaction procedure shown in Figure 3.1. An imidazolium cation functionality with a hexafluorophosphate anion chemistry (poly(1-methyl-3-(4-vinylbenzyl)-1H-imidazol-3-ium)) hexafluorophosphate [PMVBI-PF₆]) was added to the polystyrene backbone motif, as this combination has previously shown significant CO₂ interactions when utilized as a sorbent material for the capture of carbon dioxide from the atmosphere [116]. This material interacted readily with carbon dioxide when the PIL was

printed into a thin film. The synthesis of the PMVBI- PF_6 followed the procedure detailed in [60].

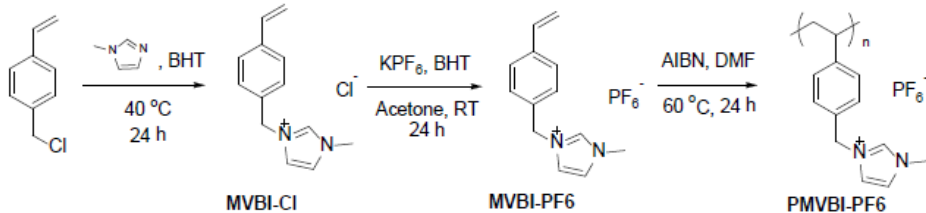


Figure 3.1. Synthesis of the imidazolium-based PIL, PMVBI- PF_6 .

3.3 Device Fabrication

Pierce oscillator circuits were implemented using Texas Instruments crystal oscillator integrated circuits (SN74LVC1GX04), with an inverter, two load capacitors ($C_1 = 22 \text{ pF}$ and $C_2 = 22 \text{ pF}$), a feedback resistor ($R_1 = 2 \text{ M}\Omega$), and an isolation resistor ($R_2 = 510 \text{ }\Omega$), as shown in Figure 3.2. The 16 oscillator circuits, aside from their crystal resonators, were built on an “instrumentation” circuit board. A separate resonator board allowed resonators to be functionalized and processed without affecting the oscillator feedback circuit. During testing, the two boards were connected via spring-pin connectors. A representation of a 16-resonator circuit board is shown within Figure 3.3. Frequency counters were implemented in a field programmable gate array (FPGA) within a National Instruments myRIO system and provided a readout accurate to $\pm 1 \text{ Hz}$. These frequency counters were implemented using digital logic (LabVIEW FPGA) that sampled rising edges of the oscillator output at a 120 MHz clock rate. The FPGA fabric accommodated 16 frequency counters, allowing simultaneous measurement and data logging.

Functional inks were developed by dissolving 100 mg of PMVBI- PF_6 into 1 mL of dimethylformamide (DMF), in order to produce a solution suitable for the deposition process. Resonators were functionalized by printing with a BioFluidix PipeJet P9 piezoelectrically actuated pipette with a $200 \text{ }\mu\text{m}$ diameter nozzle deposition system, mounted above a AeroTech PlanarDL-200-XY two-axis stage with submicron accuracy. The printing system was also

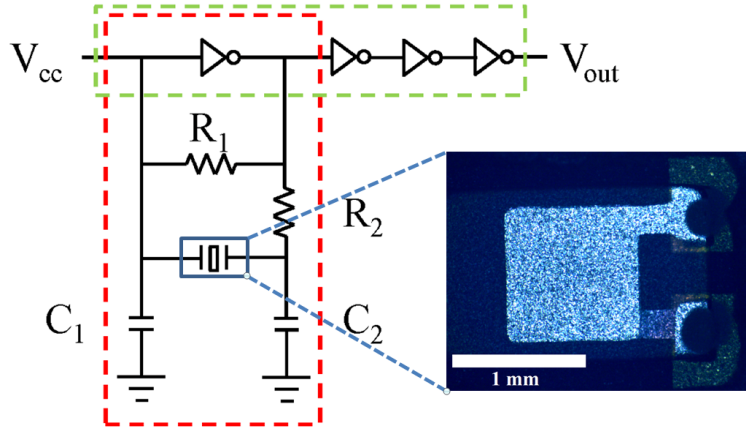


Figure 3.2. The Pierce oscillator topology used for each resonant mass sensor circuit, with the Kyocera CX3225 resonant element shown after the package cap has been removed.

outfitted with a downward-looking telecentric lens (Edmund Optics CompactTL™ 2x with 65 mm working distance) and camera (Edmund Optics EO-1312) system, which was used for the registration of drop placement on the printing substrate. It was shown in previous work that the position of the functional material affects the effective sensitivity of each device [117]. Therefore, a single 5 nL droplet was placed near the center of each resonator, in order to maximize the sensitivity. The sixteen resonator printed circuit board was functionalized with four resonators left unfunctionalized to serve as reference sensors capable of compensating for thermal effects during testing. The resonator circuit board was then left in a vacuum oven for 12 hours at 40°C to evaporate the DMF solvent, leaving behind the PIL on each resonator.

3.4 Testing Procedure

The testing chamber was secured with an inline flow distribution system with three gas sources: pure nitrogen, pure carbon dioxide, and dry air. The gas sources were connected to three mass flow controllers (MFC). The dilution flow streams (nitrogen or dry air) were connected to 500 ccm rated MFCs (MKS Instruments 1179C). The CO₂ analyte stream was connected to a 40 ccm rated MFC (MKS Instruments 1480A) in parallel. These were

connected to a manifold, the output of which was connected to the test chamber inlet. A schematic of the gas distribution system can be seen in Figure 3.3. Given the chamber volume of 163 cm^3 , complete gas exchange could be achieved in less than one minute at 280 ccm, allowing for relatively fast responses when the concentration was changed.

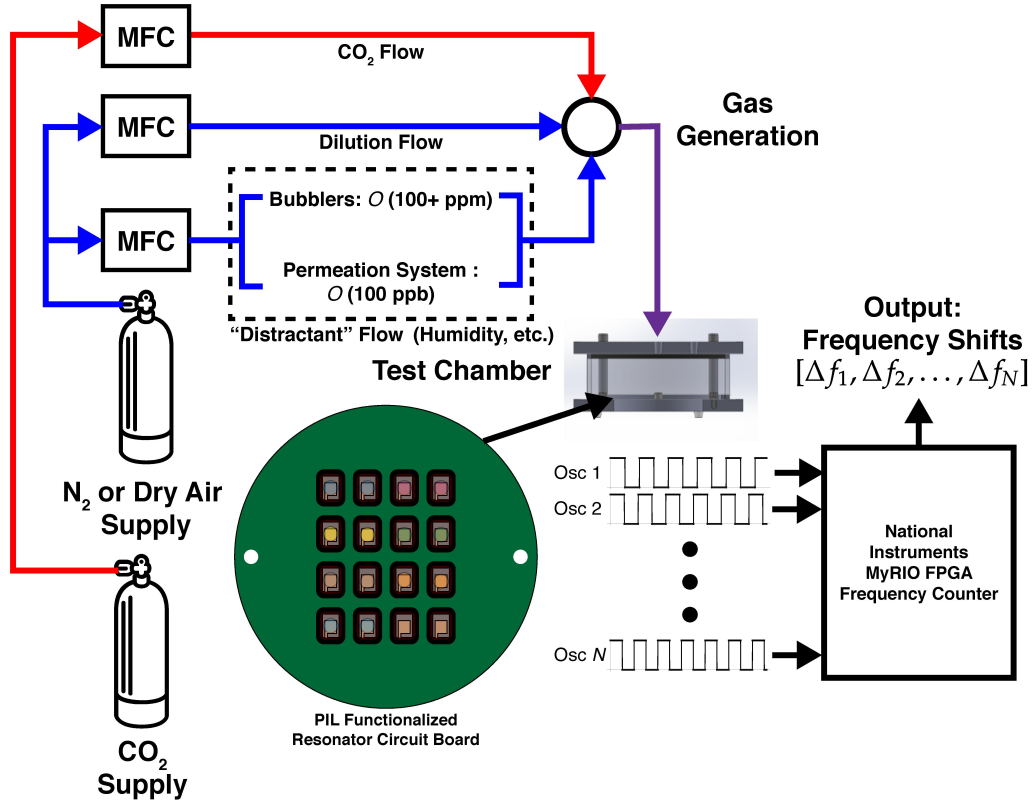


Figure 3.3. Schematic of gas distribution system and test chamber for PIL functionalized resonator testing.

Immediately prior to testing, the functionalized resonator board was secured to the instrumentation board and the chamber was sealed. The chamber was flushed with pure nitrogen at 280 ccm to create an inert environment as a baseline reference. Carbon dioxide was then introduced to the chamber at prescribed concentrations, alternated with nitrogen every 30 minutes, while maintaining the overall volumetric flow rate constant at 280 ccm for each concentration change.

3.5 Results and Discussion

Figure 3.4 shows a representative response of an unfunctionalized oscillator and an oscillator functionalized with PMVBI-PF₆ to stepped changes of CO₂ concentration. The frequency change is shown relative to baseline conditions of pure nitrogen at a flow rate of 280 ccm once steady state was achieved. A distinguishable response to CO₂ was shown across a wide range of concentration levels. It can be seen, especially at high concentrations, that the responsive change in frequency is proportional to the exposed CO₂ concentration (Figure 3.5). The reference device does not have a response to CO₂ exposure, indicating the effectiveness of the PIL functionalization. As well, during low concentration pulses (100 ppm) it can be seen that the functionalized device has a markedly larger response to CO₂ exposure than the reference device (Figure 3.6).

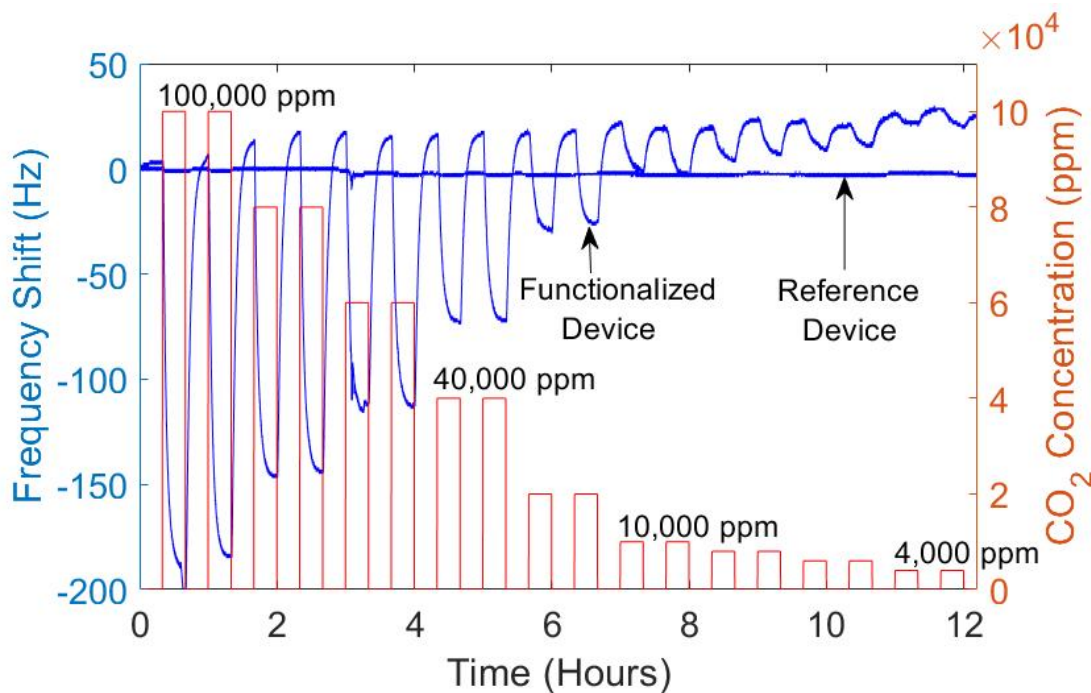


Figure 3.4. A representative oscillator response to a high concentration test range (4,000 to 100,000 ppm) with stepped CO₂ concentration changes for a functionalized oscillator and a reference channel. This concentration range corresponds to applications, such as industrial processes and human respiration monitoring.

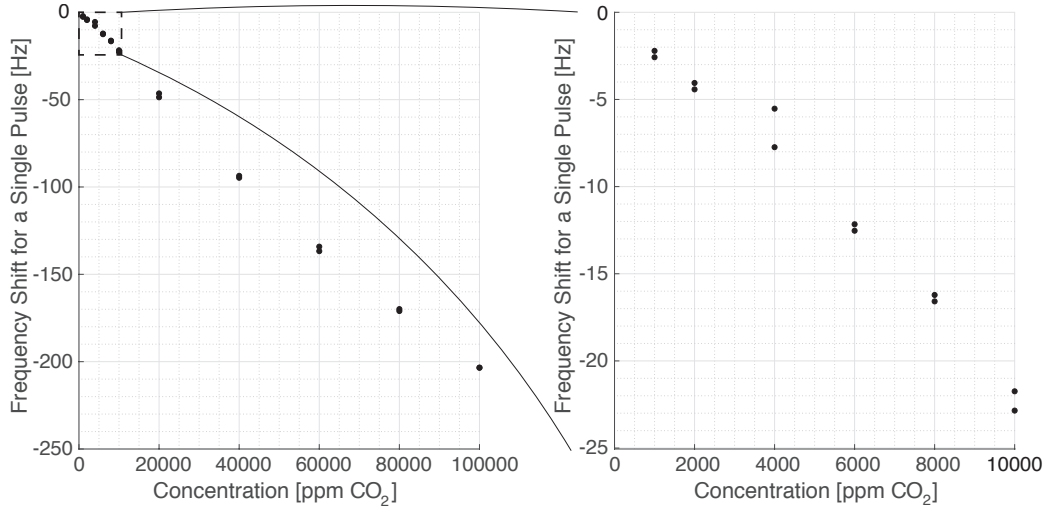


Figure 3.5. (left) Sensor response (frequency shifts) over the 1,000 ppm to 100,000 ppm range, showing relatively linear response in the high concentration (10,000 ppm to 100,000 ppm) range and (right) some deviation from linear response in the low concentration (less than 10000 ppm) range .

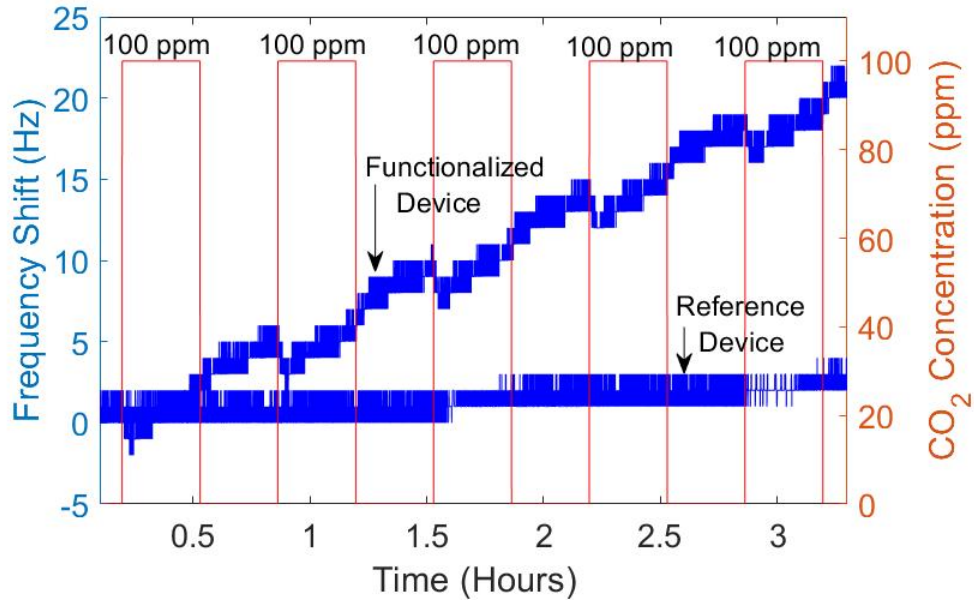


Figure 3.6. A representative oscillator response to a lower concentration test range (100 ppm) with stepped CO₂ concentration changes for a functionalized oscillator and a reference channel. This accuracy range corresponds to concentrations relevant in building occupancy and indoor air quality monitoring.

There is some long term drift present in Figure 3.6, as the effect of temperature change has not yet been compensated for [118]. There are also a number of potential concerns with the sensors, as the observed sensitivity does change from device to device. This is likely due to a combination of variability in functionalization drop placement accuracy [117], the amount of material deposited, and variation in the parameters describing the resonators and other circuit components. Future work should explore quantifying and accounting for these variations such that a consistent and accurate sensor can be developed, in addition to increasing the overall sensitivity of the device. As well, future work should consider vapor distractants (e.g., humidity, carbon monoxide, ozone and nitrogen dioxide) and accelerated life testing, to verify the durability of the PIL functionalized sensor. Given the relatively low cost and power consumption of MEMS oscillator circuits, PIL functionalized MEMS resonators may serve as an attractive alternative to current commercially available CO₂ sensors and provide useful functionality for different applications.

4. MANIPULATING POLYMER COMPOSITION TO CREATE LOW-COST, HIGH-FIDELITY SENSORS FOR INDOOR CO₂ MONITORING

The following chapter is reprinted, in part, from Z.A. Siefker *et al.* “Manipulating Polymer Composition to Create Low-Cost, High-Fidelity Sensors for Indoor CO₂ Monitoring” which appeared in *Scientific Reports* [119]. This chapter was a shared effort in which Z.A. Siefker designed, conducted, and analyzed experiments and data for the sensing system. J.N. Hodul designed, conducted, and analyzed experiments associated with the materials preparation, performance, and characterization. X. Zhao assisted in the materials preparation. N. Bajaj designed the oscillator circuit and electronic platform. K.M. Brayton assisted in materials preparation and conducted DMA analysis experiments. C.F. Hansen acquired SEM images. W. Zhao acquired AFM images. G.T. Chiu, J.E. Braun, J.F. Rhoads, and B.W. Boudouris conceived the project, designed experiments, and directed the research.

4.1 Introduction

It is estimated that the average American and European spends nearly 90% [2], [120] of their time indoors, and consequently, CO₂ concentrations in buildings can range from those seen in outdoor environmental conditions (i.e., ~400 ppm) to 3,000 ppm, depending on the occupancy of the confined space [9], [10]. Moreover, CO₂ is regarded as a toxic contaminant with an OSHA time-weighted average (TWA) exposure limit of 5,000 ppm over an 8-hour workday or a short-term exposure limit of 15,000–30,000 ppm over 15 minutes [121]. Importantly, CO₂ exposure at as low of a concentration as 1,000 ppm negatively affects cognitive performance, including decision making and problem resolution [11]–[13]. Thus, appropriate indoor air quality monitoring and building ventilation systems, equipped with low-cost, high-fidelity CO₂ sensors, are required. However, many current sensing technologies suffer from limitations and drawbacks, such as arduous device fabrication techniques or high power consumption, which limit their practical and widespread implementation in residential, commercial, and industrial settings. Thus, there is a critical need for a low-cost, low-power CO₂ sensor that is easy to manufacture and can be seamlessly incorporated into existing buildings to upgrade these structures into “smart buildings” in a seamless manner.

State-of-the-art CO₂ detection methods have relied primarily on gas chromatography and spectroscopy methods, which are typically high-cost and require large instrumentation footprints [122]–[125]. In particular, there has been a large push to use infrared (IR) spectroscopy to detect CO₂ gas. Typically, CO₂ infrared sensors are nondispersive infrared (NDIR) sensors where a broadband lamp source and an optical filter are used to select a narrow band in the spectral region that overlaps with the absorption region of the gas of interest. However, NDIR detection of CO₂ is limited by spectral interference, a high detection limit, and interference from water vapor [97]. In fact, even many new NDIR CO₂ sensors have readings that deviate from actual CO₂ concentrations by more than 75 ppm [40], [41] and potentially even greater if not regularly calibrated [100]. Additionally, the infrared light inherent to NDIR sensors, often results in bulky instrument size due to the length of the light path (> 1 cm), and high power consumption (> 200 mW), which limits their use in embedded applications, such as internet-of-thing-based (IoT-based) smart buildings. Recently, there has been work in creating a handheld, low-power (i.e., < 1 W), and sensitive (i.e., 50 ppm) CO₂ NDIR sensor capable of performing breath analysis [126]. Though intriguing, this device is not being manufactured for indoor air quality monitoring, and therefore lags in areas of testing and performance typical of indoor environments [126]. Thus, current NDIR CO₂ sensors do not meet the power, size, and selectivity metrics necessary for a practically scalable sensor that can meet the demands of smart building technologies suitable for the indoor monitoring of CO₂.

Microelectromechanical systems-based (MEMS-based) resonant mass sensors are a promising sensor paradigm for this application space as they exhibit high performance metrics in gas detection due to their compact size, low cost, low power, fast response times, and high sensitivity [89], [106], [127]–[129]. Importantly, when microresonators are functionalized with specific surface chemistries, target analytes non-covalently bind, or otherwise chemo-mechanically interact, with the sensor. This change in mass on the surface induces a shift in the resonant frequency of the device, which can be readily and precisely quantified. In fact, cantilevered-type resonant mass sensors are sensitive enough to detect bacteria and a single virus in air [130], [131]. Therefore, MEMS-based devices are an ideal platform for smart building integration, if they can be functionalized with the appropriate and selective

chemistry in a low-cost, high-throughput manner [132]. Given this potential, we fabricated a resonant mass sensor with a solution-processable polymer blend of poly(ethylene oxide) (PEO) and poly(ethyleneimine) (PEI) coated atop the resonant platform. The selection of these two materials was rather straightforward. First, PEI contains multiple amine groups that have been shown to effectively perform reversible acid-base reactions with CO₂ [133]–[136]. However, due to the viscous nature of PEI, diffusion of the CO₂ into the material to perform such reactions is limited. Thus, we employed a hydrophilic, semi-crystalline polymer, PEO, [137] in the blend with PEI to enhance the sensitivity and response rate of CO₂ uptake. The PEO has two roles when being incorporated into the PEI. First, it disrupts intrachain and interchain PEI entanglement at the molecular level and the surface morphology at the nanoscale level. Both of these positive disruptions facilitate increased interactions between accessible amines and CO₂. Second, the hydrophilic nature of PEO attracts water into the blended thin film; in turn, this water converts the reversible acid-base formed carbamates (i.e., the product of CO₂ reacting with primary and secondary amines) into bicarbonates freeing amines to enhance the adsorption and uptake of CO₂. This critical addition of the PEO moiety allows for the macromolecular blend to have selective and significantly enhanced detection of CO₂ relative to previous efforts. This synergetic chemical blending and subsequent polymer processing, in combination with the resonant mass sensor platform, allows for the fabrication of a low-cost and effective CO₂ sensor. In comparison to other CO₂ sensing counterparts, this sensor is compact, with a footprint of less than 25 mm², and offers high sensitivity (i.e., at a detection limit of CO₂ as low as 5 ppm). Moreover, these sensors detect CO₂ selectively over other polar compounds (e.g., methanol and acetone), as well as non-polar compounds (e.g. xylene and propane). Thus, this sensing platform offers an easily functionalized, low-cost, low-power, multi-channel sensing array capable of quick and reliable detection.

4.2 Experimental Methods

4.2.1 Materials

All of the chemicals were purchased from Sigma-Aldrich, and they were used as received unless otherwise noted. The PEI utilized had a reported weight average molecular weight of 25 kg mol⁻¹. The PEO utilized was purchased from Alfa Aesar, and it had a reported weight average molecular weight of 100 kg mol⁻¹. The methanol utilized to prepare the polymer samples was anhydrous grade and stored under nitrogen. Polished silicon dioxide substrates utilized for imaging were purchased from Silicon Valley Microelectronics.

4.2.2 General Methods

A Veeco Dimension 3100 Atomic Force Microscope (AFM) in tapping mode was utilized for AFM imaging. For these images, the polymer samples were fabricated by depositing 1.0 μ L of a 1 mg mL⁻¹ polymer blend in methanol on a polished silicon dioxide substrate. Then, the sample wafers were dried under vacuum ($P \leq 0.4$ Torr) overnight to remove solvent. The images for the 3:1 PEO:PEI, 1:1 PEO:PEI, PEO-only, and PEI-only films were acquired using this protocol. A Hitachi S-4800 Field Emission scanning electron microscope (SEM) was utilized to image the PEO:PEI. For these images, 1.0 μ L of a 1 mg mL⁻¹ polymer blend in methanol solution were drop cast on polished silicon dioxide substrates and dried overnight under vacuum. All of the polymer films were then coated with 20 nm of conducting carbon using a SPI carbon sputter coater prior to imaging. The images for the 3:1 PEO:PEI, 1:1 PEO:PEI, PEO-only, and PEI-only films were acquired using this protocol. X-Ray diffraction (XRD) measurements were measured with a Rigaku Cu-K source ($\lambda = 1.54056$ Å) in parallel beam mode. These samples were acquired while under ambient conditions. The polymer film samples were fabricated using a 240 mg mL⁻¹ solution of the polymer blend in methanol pipetted into a metal mold and then annealed at 80 °C while being pressed for at least 10 min. After pressing, these films were dried overnight under vacuum ($P \leq 0.4$ Torr) prior to XRD analysis being performed. A Thermo-Nicolet Nexus Fourier Transform Infrared Spectroscopy (FTIR) with a KBr beam splitter with a 800 cm⁻¹ - 4500 cm⁻¹ spectra range was utilized for

FTIR analysis of the PEO:PEI polymer films. The polymer films were fabricated utilizing the same protocol as discussed for XRD analysis. For Dynamic Mechanical Analysis (DMA) of the polymer films, a TA Instruments DMA Q800 with a film tension clamp was utilized. These experiments were conducted at a temperature ramp of $0.5\text{ }^{\circ}\text{C min}^{-1}$ and at a constant frequency of 1 Hz. The polymer films were fabricated utilizing the same general protocol as discussed for XRD analysis.

4.2.3 Device Testing

Testing of the devices was performed using the experimental setup shown in Figure 4.1a. Gas tanks of nitrogen, air, and carbon dioxide were connected to a series of mass flow controllers (MFC; MKS, 1179C) in parallel. A subset of nitrogen-supplied MFCs was connected to bubblers (ChemGlass, AF-0085) for introducing humidity or select vapor distractants (i.e., acetone, ethanol, toluene, and xylene). The gas lines converged to a mixing manifold, the output of which was connected directly to the test chamber inlet. A 95 mm diameter and 23 mm in height cylindrical aluminum testing chamber was used for evaluating the sensors. A 6.4 mm gas inlet port was centrally-located on the top of the test chamber and two 6.4 mm exhaust ports were located on opposite sides of the test chamber. The small chamber volume allowed for complete gas exchange in less than one minute, facilitating quick sensor responses upon changing MFC flow rates.

Prior to sensor testing, the resonator board was attached to the instrumentation board. The test chamber was flushed with nitrogen or air to create an inert environment as the baseline for experimentation. Subsequently, the analyte gases were injected into the chamber to achieve the reported concentrations. A frequency counter was developed in LabVIEW to monitor the oscillation frequency of each oscillator with a 1 Hz resolution. To facilitate parallel monitoring, the frequency counter was synthesized and executed on an NI myRio Field Programmable Gate Array (FPGA). An FPGA consists of a collection of logic elements between which electrical paths can be created and allows for parallel computing. Thus, each of the 16 frequency counting loops could run simultaneously.

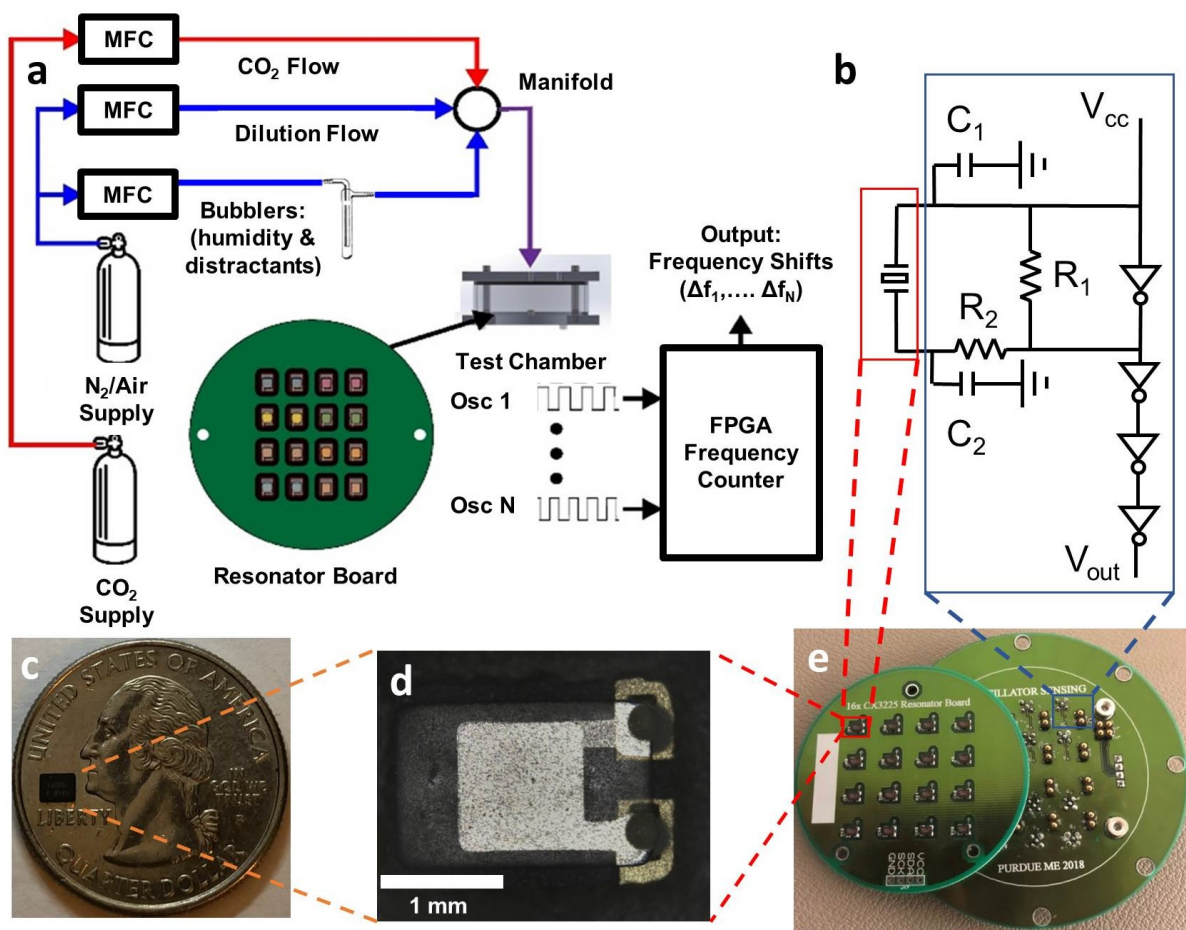


Figure 4.1. (a) Schematic of the gas distribution system used for sensor testing. Mass flow controllers (MFCs) modulated supply gases to the test chamber containing functionalized oscillators. Bubblers connected to a MFC were used to moderate distractant analytes and humidity levels inside the testing chamber. A frequency counter, executed on a MyRIO FPGA monitored the frequency of each oscillator in parallel. (b) A schematic of the Pierce oscillator used. The resonant element, outlined by the red box, is shown on the left of the circuit diagram. The remainder of the oscillator circuit, which is contained on the instrumentation board, is outlined by the blue box. This portion of the diagram contains two load capacitors (C_1 and C_2), a feedback resistor (R_1), and an isolation resistor (R_2). A series of inverters between the supply voltage (V_{cc}) and the output voltage (V_{out}) are used to square-off the oscillator output signal to facilitate frequency counting. (c) A single packaged resonant element shown on a US quarter for scale. (d) An exposed quartz crystal resonant element. (e) A resonant mass sensing system with 16 Pierce oscillators. A resonator board (left) containing 16 resonant elements is shown offset from the instrumentation board (right) which completes the Pierce oscillator circuit.

4.2.4 Device Instrumentation

An array of 16 Pierce oscillators was used as the sensing platform. Figure 4.1 shows the Pierce oscillator circuit, which consisted of an inverter, two load capacitors ($C_1 = 22$ pF and $C_2 = 22$ pF), one feedback resistor ($R_1 = 2$ M Ω), one isolation resistor ($R_2 = 510$ Ω), and a 16 MHz quartz crystal resonator (Kyocera Corp., CX3225). The crystal oscillator driver (Texas Instruments, SN74LVC1GX04) provided the circuit with the Pierce oscillator inverter as well as three additional inverters, which effectively squared the oscillator output signal. The hardware implementation of the oscillator circuit resulted in two printed circuit boards: (i) a board containing only an array of resonators and (ii) an instrumentation board containing the 16 sets of oscillators with spring pin connectors in place of the resonators (Figure 4.1e). As such, the resonator boards could be functionalized independent of the rest of the oscillator circuit and easily interchanged without incurring high component costs.

A single crystal resonator has a small footprint (8 mm²) and low power requirement (< 200 μ W) during operation. Figure 4.1c shows a single packaged crystal resonator on top of a United States quarter, for scale. The small size and low power requirement of a single resonant sensor is particularly promising when considering wireless and distributed sensing in buildings [14], [138], [139]. The resonant element of the Kyocera CX3225 is shown in Figure 4.1d, after the package cap has been removed. Functional materials were applied directly to this exposed element.

4.2.5 Device Functionalization

PEI and PEO were dissolved in methanol to generate a solution of 0.1% (by volume) of PEI and 0.3% (by volume) of PEO. Then, 1 μ L of this solution was deposited onto each resonator using a micropipette. The resonator board was then placed under vacuum at 70 $^{\circ}$ C for 12 hours to remove any residual methanol, leaving behind a 3:1 PEO:PEI blend film (by weight). Unless otherwise specified, the devices utilized in the tests were all functionalized with the 3:1 PEO:PEI (by weight). Prior to testing, the resonator board was allowed to equilibrate back to room temperature.

4.3 Results

4.3.1 Sensor Response and Dynamic Range

Resonant mass sensors functionalized with a PEI-PEO polymer blend were able to detect CO₂ across an extended range of concentrations relevant to indoor air quality monitoring (Figure 4.2). Critically, these sensors demonstrated a highly linear response at CO₂ concentrations relevant to the targeted application of buildings. This range is roughly defined by a lower bound of 400 ppm (i.e., the concentration that is typical for air outdoors, located in unoccupied spaces) and an upper bound of 2,000 ppm. A building with well-controlled ventilation will have CO₂ concentrations around 1,100 ppm, which is the central region of interest [8]. Figures 4.2a-c highlight sensor responses at CO₂ concentrations that are relevant to indoor environments. These data demonstrate sensor performance in a background of nitrogen and a background of air (i.e., ~78% nitrogen, ~21% oxygen, and ~0.12% carbon dioxide). In both the nitrogen and air backgrounds, the sensor response was linear and proportional to the increase in CO₂ concentrations above the background concentrations with an interpolated sensitivity of approximately 0.12 Hz ppm⁻¹ CO₂ (Figure 4.2c). The time series data (Figures 4.2a-b) show the resonators decreasing in frequency as CO₂ is adsorbed on top of the resonator. The added CO₂ mass on the resonator decreases its resonant frequency, as described, for example, by the Sauerbrey equation [111], [112]. The magnitude of the frequency shift is greater at higher concentrations due to an increased amount of CO₂ adsorbing onto the resonator. Thus, the change in CO₂ concentration induces a clear shift in resonant frequency of the sensor.

Moreover, this sensor has a large dynamic range and can detect CO₂ at concentrations well beyond what is relevant to indoor air monitoring (Figure 4.2d). Unlike the relatively linear response demonstrated below 2,000 ppm CO₂, when extended to higher concentrations, a nonlinear response is apparent as the frequency shift per ppm of CO₂ decreases asymptotically. This is consistent with a Langmuir sorption model where the rate of adsorption decreases as the available surface binding sites are filled [140]. Nevertheless, this sensor can discriminate CO₂ concentrations well beyond toxic levels for human occupancy [141].

Conversely, under inert backgrounds this sensor can detect as low as 5 ppm, highlighting its broad range and sensitivity.

4.3.2 Performance in Indoor Environments

Even in a relatively well-controlled, indoor environment, air conditions can drastically vary in both temperature and humidity level. Thus, it is important to account for these variables and demonstrate sensor performance across a span of potential environmental conditions. A ‘comfort zone’, which describes indoor air conditions that most people find comfortable, has been defined by the engineering society ASHRAE [98]. This region is outlined on the psychrometric chart (Figure 4.3a) based on indoor air temperatures and humidity levels. Using the comfort zone as a guide, a test region was developed spanning approximately 0%-80% relative humidity (at a given temperature) and 22–26 °C, and testing was performed near the extremes of this region, as well as near the center.

Previously, PEI has been used to effectively detect and capture CO₂ [62], [65], [133], [134], [144]. This is because CO₂ reacts with the primary and secondary amines of PEI readily to form carbamates that can be stabilized by other primary amines or with water and create bicarbonate ions [135]. When PEI is mixed with PEO and supported onto mesoporous oxides, PEI is a powerful adsorbent of CO₂ [145], [146]. However, few studies have evaluated the adsorption of CO₂ onto blended films of PEO and PEI without a mesoporous substrate for the purpose of measurement under indoor air conditions. PEO, when blended with PEI enhanced the frequency response and sensitivity of the sensor to CO₂ (Figure 4.3b). Under dry air conditions (i.e., 0% RH) the frequency response of the polymer blend is more than twice that of PEI alone. Additionally, when increasing the background relative humidity level to 10% and then to 80% at a constant temperature, the frequency shift response to CO₂ is nearly tripled and then quadrupled, respectively, relative to the resonator functionalized with PEI only. Furthermore, the PEO and PEI blends have shown promising performances in both elevated temperature and elevated humidity conditions, simultaneously (Figures 4.3c-d).

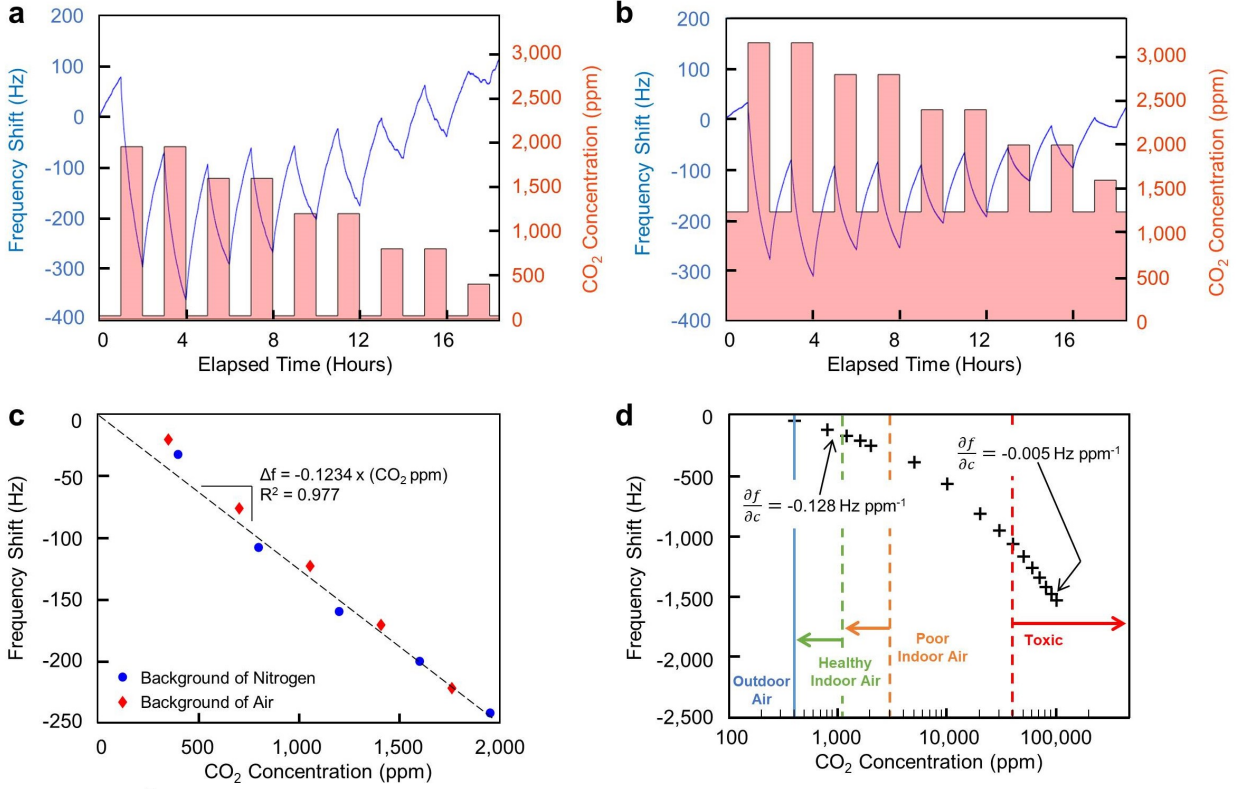


Figure 4.2. Sensor response to CO₂ shown as a frequency shift of the resonant element. (a) Sensor response to CO₂ over time with a background of nitrogen. The resonant frequency shift response is indicated by the blue line (left vertical axis) and the red bars indicate when CO₂ is present (right vertical axis). (b) Sensor response to CO₂ over time with a background of air. The resonant frequency shift response is indicated by the blue line (left vertical axis), and the red bars indicate when CO₂ is present (right vertical axis). The use of air brought the baseline CO₂ concentration to 1,200 ppm. (c) Total frequency shift of the device after 1 hour of CO₂ at specified concentrations. Regardless of the baseline conditions, a similar linear response is obtained by the sensor, as demonstrated by the linear regression fit. (d) The dynamic range of the sensor is shown by plotting the resonant frequency shift in response to 1 hour of CO₂ in a background of nitrogen. For comparison, outdoor air CO₂ concentrations [142] are indicated by the solid blue line, healthy indoor air CO₂ levels [8] are indicated by the dashed green line, poor indoor air CO₂ levels [8], [143] are indicated by the dashed orange line, and toxic CO₂ levels [141] are indicated by the dashed red line. Additionally, the sensitivity (indicated by the change in frequency per change in CO₂ concentration, $\frac{\partial f}{\partial c}$) is shown at both low and high concentrations.

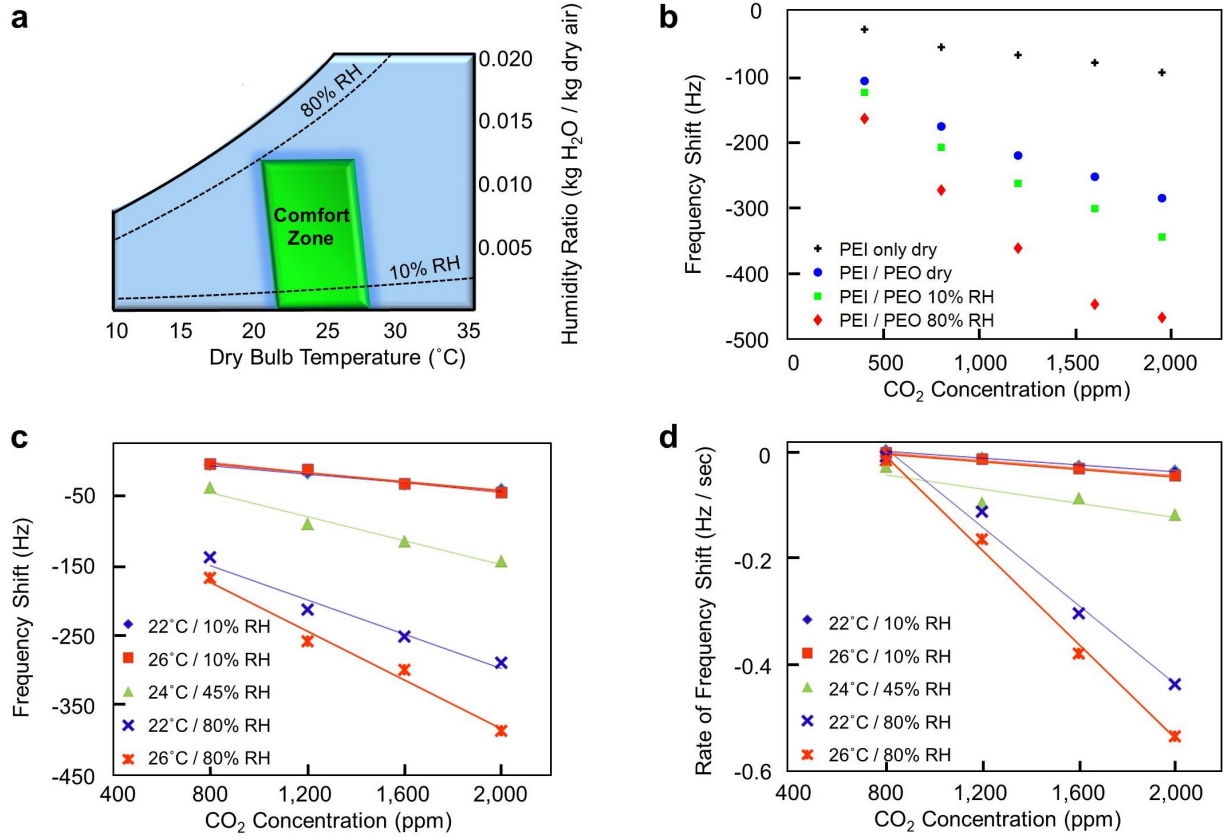


Figure 4.3. (a) Psychrometric chart defining the ‘Comfort Zone’ air temperature and humidity range, as defined by the engineering association, ASHRAE. Testing was performed across this region to simulate environmental conditions expected in high performance buildings. (b) Frequency response of devices functionalized with PEI only, and a 3:1 PEO:PEI blend ranging from 0 to 80% relative humidity (RH). Tests were performed holding temperature at 24 $^{\circ}\text{C}$. (c) Sensor response to CO_2 while varying temperature from 22–26 $^{\circ}\text{C}$ and relative humidity from 10–80% to cover the indoor air comfort zones [98]. A baseline condition of 400 ppm CO_2 in nitrogen was used to simulate outdoor air conditions and a linear response is obtained at each condition, as demonstrated by the linear regression fits. (d) The rate of change in frequency shift after each increase in CO_2 concentration from a background of 400 ppm. A similar linear response is obtained at each condition, as demonstrated by the linear regression fits.

4.3.3 Sensor Selectivity

These sensors showed a high level of selectivity to CO₂ even when other interfering gases (i.e., distractant gases) were introduced into the chamber (Figure 4.4). Specifically, these tests were performed with a variety of confounding species including propane, carbon monoxide, acetone, ethanol, toluene, and xylene. Each test alternated between 30 minute pulses of analyte gases and a nitrogen purge of the test chamber. CO₂ and the selected interfering gases were each introduced at concentrations of 1,000 ppm for comparison. It should be noted that 1,000 ppm is a common CO₂ level for indoor environments; however, for the distractants considered, this concentration is well above what is considered safe [136]. Thus, these distractant gases tested are on the extreme side of what could potentially confound the sensors under practical operating conditions. Tests were performed to show a CO₂ pulsed alone, the distractant vapor pulsed alone, CO₂ and the distractant pulsed together, and CO₂ pulsed with a background distractant level. Testing in this manner allowed for a direct comparison of the sensor response to CO₂ and the distractant, as well as any interacting effects on the sensor when CO₂ and the distractant are presented together. For all of the distractants tested, the sensor had a distinguishable response to CO₂ and a lesser response (if any) to the distractant vapor. Acetone, for example, induced an average shift of 128 Hz during a 30 minute pulse, whereas CO₂ induced an average shift of 734 Hz for the same time period (Figure 4.4a). Thus, the influence of acetone, at a relatively high concentration for indoor environments, was nearly 6 times less than the sensor’s response to CO₂ at the same concentration.

4.3.4 Polymer Film Properties Impact CO₂ Detection

The optimal and reliable detection of CO₂ using a 3:1 PEO:PEI blend film is due to the ability of the semi-crystalline nature of PEO to disrupt the intermolecular interactions of the hyperbranched PEI. PEI, a polymer with many amine branches ranging from primary to tertiary amines, is an amorphous material that has a relatively low glass transition temperature (i.e., in our hands, it was -50 °C for a molecular weight of 25 kg mol⁻¹). Thus, branched PEI at room temperature exists as a highly viscous liquid due to the strong non-covalent

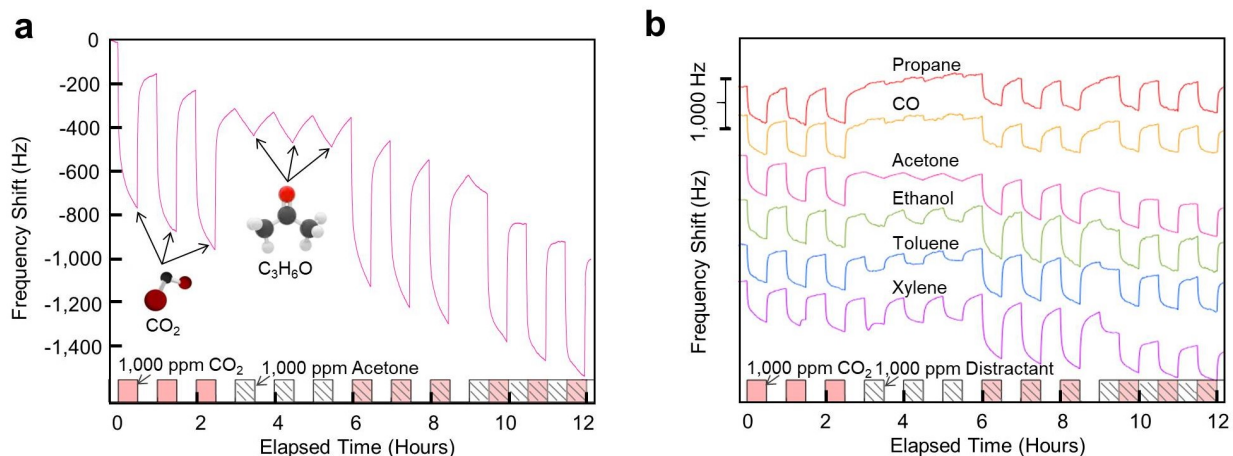


Figure 4.4. Sensor response to 1,000 ppm pulses of CO_2 and various distrac-tants. (a) Zoomed frequency shift response of a sensor in response to CO_2 in the presence of acetone. The time series data shows 30 minute pulses of CO_2 with a background of nitrogen, followed by pulses of acetone, pulses of CO_2 and acetone together, and finally pulses of CO_2 with a constant background of acetone. (b) Frequency shift responses of a sensor in the presence of various interfering gas analytes.

interchain amine interactions and polymer entanglements [147]. PEI, when drop cast onto a substrate and dried under vacuum, remains a uniform polymer film with minor surface defects or disruptions (Figures 4.5a-b) on the PEI surface until another material or polymer is introduced into the PEI casting solution. A pristine PEI thin film has difficulty detecting CO_2 due to the high viscosity and nanostructural uniformity caused by the hyperbranched amine interchain interactions of a PEI film (Figure 4.3b), which can hydrogen bond and become highly entangled with each other. These entangled amines, many of which are primary amines, prevent the ready diffusion of CO_2 into the material to interact, which ultimately limits the CO_2 uptake and subsequent sensor response.

When PEO is blended in a 3:1 ratio with PEI, surface features and nanoscale disruptions in the blended polymer film were observed (Figures 4.6a-b). This surface segregation also occurred to a lesser degree in the 1:1 PEO:PEI blend film (Figures 4.5c-d). These defects and disruptions in the PEI film are indicative of altering macromolecular interactions when PEO is incorporated into a PEI matrix. This macromolecular rearrangement promotes CO_2 adsorption because CO_2 can now diffuse into the PEI material and interact readily with

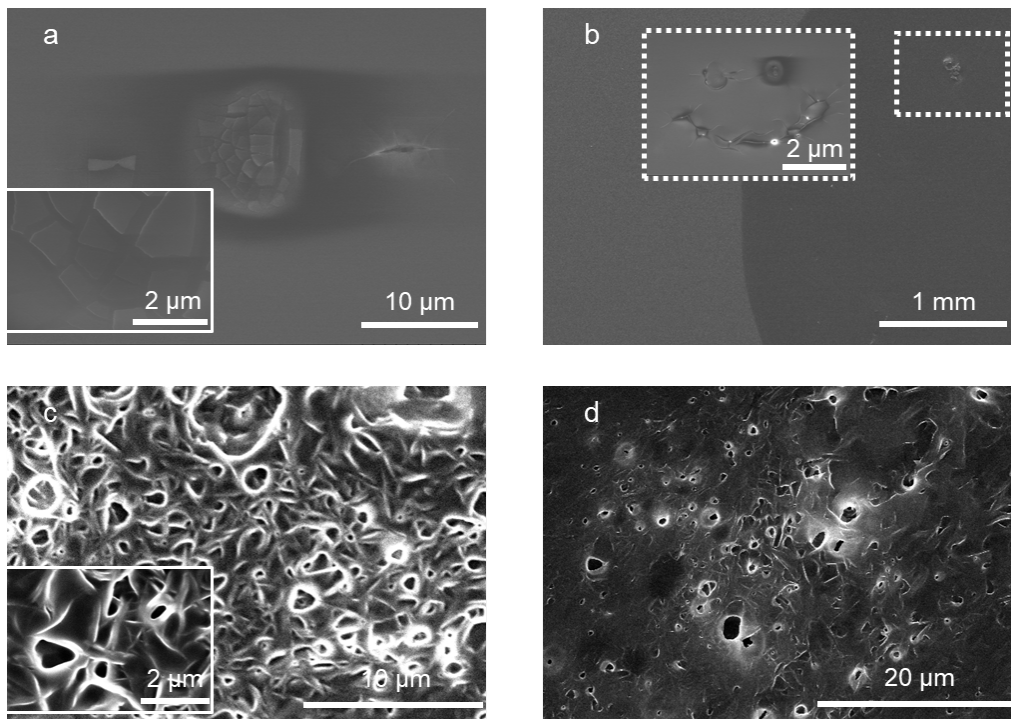


Figure 4.5. (a) and (b) SEM images of a PEI film after being drop cast onto a silicon wafer and dried for 12 hours under vacuum. The two panels show the same film at two different magnification levels. (c) and (d) SEM images of a 1:1 PEO:PEI (by weight) blend film after being drop cast onto a silicon wafer and dried for 12 hours under vacuum. The two panels show the same film at two different magnification levels.

accessible primary and secondary amines which were not accessible prior to the addition of PEO. Moreover, when incorporating the PEO into the PEI matrix there was an observed crystal structure as seen in X-ray diffraction (XRD) (Figure 4.6c) with characteristics reflections at $q = 1.3 \text{ \AA}^{-1}$ and $q = 1.65 \text{ \AA}^{-1}$, which is consistent with the monoclinic crystal structure of PEO [148], [149].

When PEO is added to the amorphous PEI, PEO tries to maintain order, and this ordering of PEO disrupts the PEI entanglements. In turn, this reduces the side chain amines from interacting with other interchain amines. As a result, there is polymer phase separation and surface morphology alterations in the film. When these alterations occurred, CO_2 more effectively diffused into the PEI matrix such that larger uptake occurred. Thus, as seen in a 0% relative humidity environment, the PEO:PEI blended film can interact better with CO_2

than PEI alone (Figure 4.3b). This surface morphology alteration agrees with previous work with similar blends when the PEO molecules physically shielded the PEI chains from one another to reduce individual PEI-PEI chain interactions [145]. This PEO-induced physical disruption of interchain PEI amines from one another is in direct agreement that intrachain CO₂ adsorption events (i.e., rather than interchain) are a result of the PEO causing less PEI branched amine interchain interactions, resulting in less diffusional limitations and more reactivity between CO₂ and primary and secondary amines.

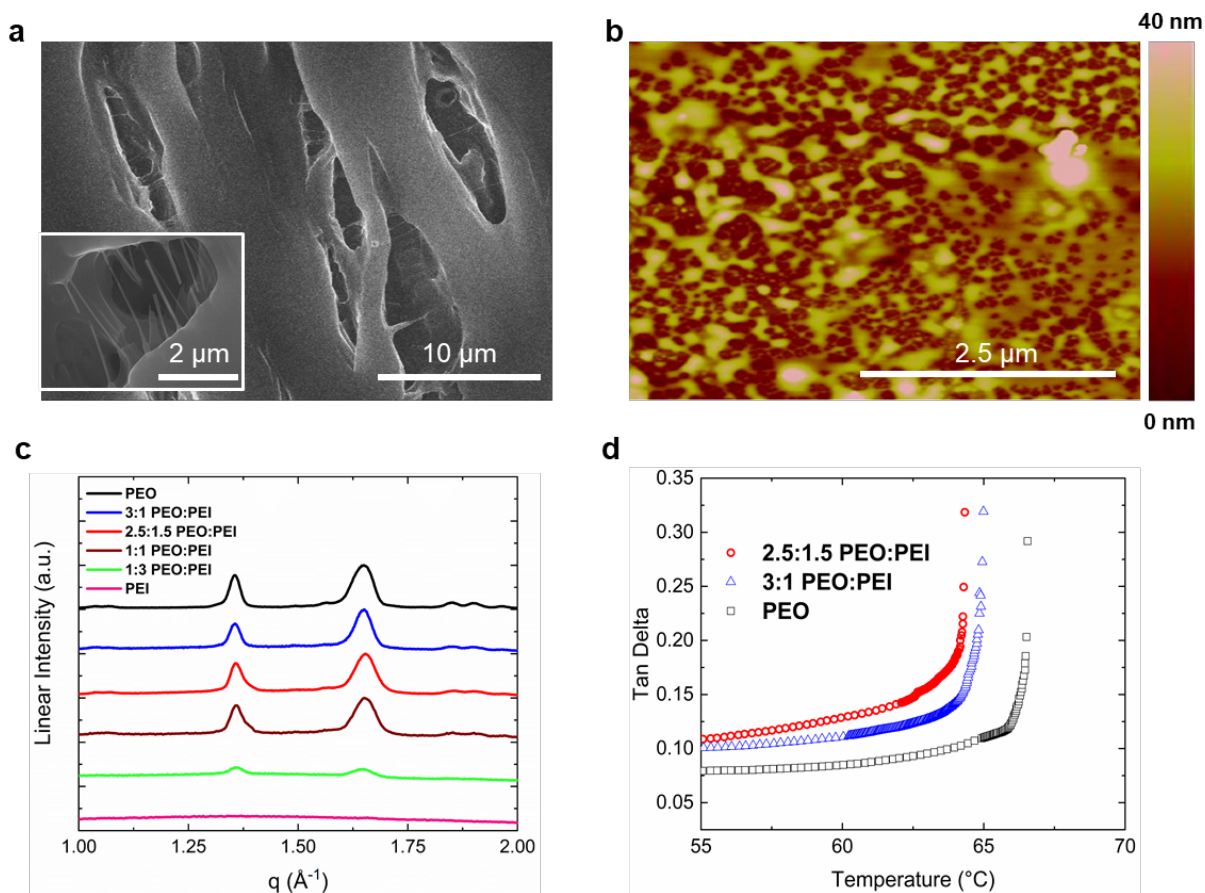


Figure 4.6. (a) SEM images of a 3:1 PEO:PEI blend film. Both images shown are of the same film but in different sections and zoom locations. (b) AFM images of a 3:1 PEO:PEI blend films. (c) XRD patterns of PEO, 3:1 PEO:PEI blend, 2.5:1.5 PEO:PEI blend, 1:1 PEO:PEI blend, 1:3 PEO:PEI blend, and PEI only films. (d) DMA of a 2.5:1.5 and 3:1 PEO:PEI, and PEO only blend films.

Furthermore, dynamic mechanical analysis (DMA) showed that a pure PEO film has a decreased $\tan \delta$ maximum value of 0.28 in comparison to films containing amorphous PEI. This increased storage modulus in PEO reinforces our observations in the XRD data showing that PEO maintains an ordered structure (Figure 4.6d). Unlike PEI, which behaves as a highly viscous liquid with many entangled amines, PEO has a low $\tan \delta$ due to the crystalline order in the material. When PEO is added into the PEI material, at 2.5:1.5 and 3:1 PEO:PEI blend films, the $\tan \delta$ maximum was 0.32. As the ratio of PEO to PEI increases, the $\tan \delta$ signal decreased due to the physical disruptions of PEO solvating and shielding branched PEI amines as PEO tries to maintain its crystal structure. As a result, this orders the polymer matrix, creates less amine entanglements, and increased the storage modulus in the blended material. This ordering of the PEI by PEO at the 3:1 PEO:PEI ratio produces a $\tan \delta$ maximum in the material capable of interacting with CO₂. More specifically, this $\tan \delta$ maximum caused by the PEO allows for less amine entanglements, which causes more surface area for CO₂ to adsorb into the material to interact with PEI. Thus, more CO₂ can interact with PEI intrachain amines and yield a better response on the sensor device. Therefore, due to the ability of PEO to provide some structural order to the amorphous PEI, there is detection of CO₂ on a 3:1 PEO:PEI blended film.

4.3.5 PEO Hydrophilic Properties Further Enhance CO₂ Detection

In addition to providing structural changes in the PEI matrix, PEO facilitates water uptake into the polymer matrix, and this allows for more reversible acid-base reactions to occur between the PEI amines and CO₂. When the 3:1 and 1:1 PEO:PEI blend films were exposed to a humid environment and had their Fourier Transform Infrared Spectroscopy (FTIR) spectra acquired, there was observed water uptake into the blend films (Figure 4.7). This water uptake in the 3:1 PEO:PEI films is important when detecting CO₂ because these films showed a frequency shift response to CO₂ that was significantly enhanced relative to the resonator functionalized with PEI only (Figure 4.3b-d).

PEI is a highly branched polymer with primary, secondary and tertiary amino groups, and these different chemical environments interact with CO₂ in distinct manners [150], [151].

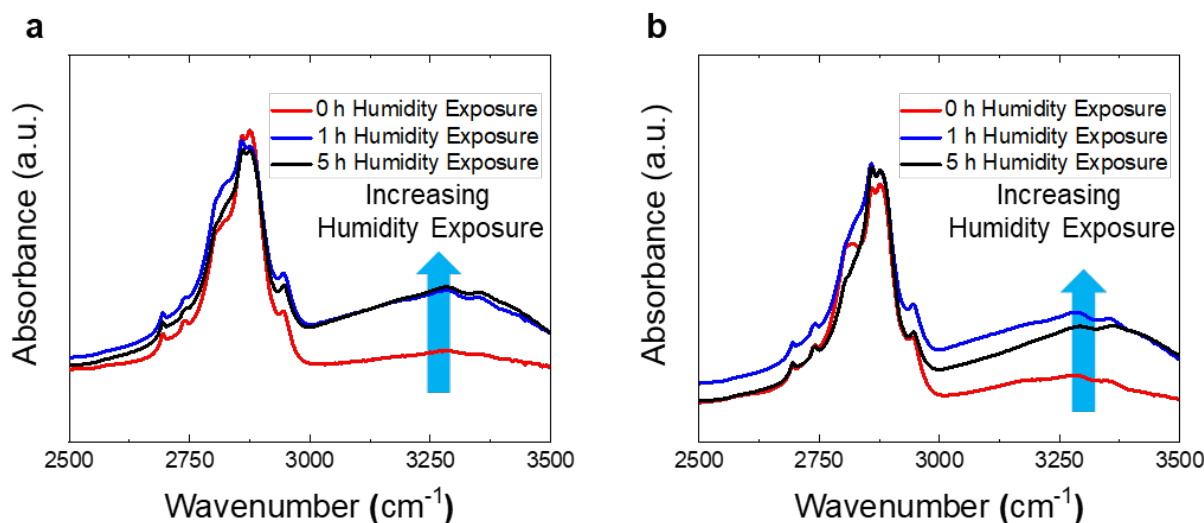


Figure 4.7. (a) FTIR spectra of a 1:1 PEO:PEI polymer blend film after being annealed and dried under vacuum to remove any excess solvent and exposed to 40% relative humidity at room temperature for up to 5 hours. (b) FTIR spectra of a 3:1 PEO:PEI polymer blend film after being annealed and dried under vacuum to remove any excess solvent and exposed to 40% relative humidity at room temperature for up to 5 hours. The broad OH stretch is observed at 3300 cm^{-1} .

That is, primary and secondary amino groups can directly react with CO_2 to form carbamate groups by a reversible acid-base reaction. More specifically, direct nucleophilic attack on a free CO_2 by a primary or secondary amine forms a zwitterion, which rapidly rearranges to carbamic acid via intramolecular proton transfer. In the presence of another free amine, which now acts as a Brønsted base, the carbamic acid may be converted into a carbamate via intermolecular proton transfer. Thus, these carbamates are stabilized by another amine that becomes protonated to form an ammonium ion. Under dry conditions the reaction stops here; however, the availability of water can further convert the carbamate into stable bicarbonate (Figure 4.8).

As a result, this frees an amine that then can react with more available CO_2 gas. Tertiary amines do not directly react with CO_2 without water. However, there is the possibility that water and CO_2 can form carbonic acid which can be deprotonated by all of the types of substituted amines to form bicarbonate as well. In this alternative route, carbonic acid groups are typically deprotonated at neutral pH by a single amine (i.e., any substitution)

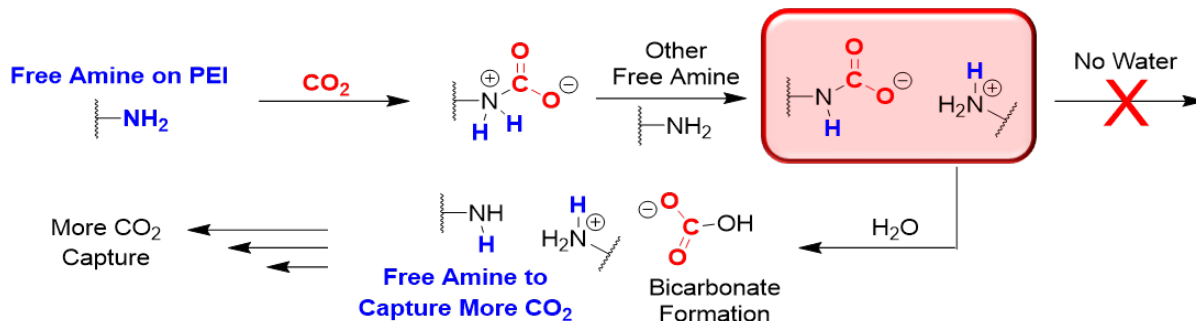


Figure 4.8. Proposed mechanisms of CO₂ capture by PEI with and without the presence of water. The intermediate step indicated in red is the key step in this reaction process. Without the presence of water the reaction does not proceed and the amine does not become accessible. With the presence of water the reaction can proceed forward due to a free amine which can capture more CO₂.

instead of multiple amines. Due to a single amine being involved in the deprotonation on the carbonic acid this allows for another amine to be available to attack other carbonic acids that may be present. Regardless of which route is occurring (i.e., direct CO₂ attack or deprotonation of carbonic acid), water does have a major impact on how the polymer matrix can interact with CO₂. Therefore, PEO in addition to providing order to the PEI and increasing the accessibility of the amines to reversibly react with CO₂ also increases the abundance of water in the polymer matrix when under humid conditions, and this increases the adsorption capacity of CO₂ in the blended film.

4.4 Discussion

Here, a resonant mass sensor treated with a polymer blend of PEO and PEI was presented for the sensitive and selective detection of CO₂. The synergetic blending of PEO and PEI provided an enhanced materials platform for reversible sorption of CO₂. This, combined with a MEMS-based resonant mass sensing platform, created an exceptional sensor for indoor CO₂ monitoring. The small size and low power requirement of these sensors provides the necessary qualifications for wireless and distributed sensing in buildings [14], [138], [139]. Further, the readily accessible materials used to manufacture this sensor renders a device that is easy to

procure at a low cost. Thus, this unique combination of well-known materials allows for a novel CO₂ sensor that can be seamlessly integrated into smart building environments.

5. SORPTION KINETICS OF POLY(ETHYLENEIMINE)-POLY(ETHYLENE OXIDE) BLENDS AND THE IMPLICATION FOR LOW-COST, SMALL-SCALE CO₂ SENSORS

The following chapter was a shared effort in which Z.A. Siefker designed, conducted, and analyzed experiments and data for the sensing system. J.N. Hodul designed, conducted, and analyzed experiments associated with the materials preparation and characterization. C.F. Hansen acquired SEM images and assisted in XPS analysis. G.T. Chiu, J.E. Braun, J.F. Rhoads, and B.W. Boudouris conceived the project, designed experiments, and directed the research.

5.1 Introduction

It has been estimated that people spend about 90% of their time in indoor locations in modern society, even prior to the start of the current global pandemic [152]. This time inside involves private and public indoor environments, such as homes, gyms, schools, and workplaces. However, these interior locations can contain elevated concentrations of deleterious gas analytes, especially when they are poorly ventilated, which can impact the indoor air quality (IAQ) of these locations [153]. Carbon dioxide (CO₂) is a deleterious gas analyte that, in poorly ventilated spaces, can exist at concentrations of upwards of several thousand parts per million (ppm) [9]. At these concentrations, CO₂ can have substantial effects on human cognitive performance with statistically significant and meaningful reductions in decision-making performance [12], [154], [155]. However, even at significantly lower concentrations, CO₂ is a useful IAQ metric, because it serves as a proxy measure for human occupancy and the proportional impacts on IAQ [8], [156]. Thus, there is an increasing interest in developing low-cost IAQ sensors for smart and connected buildings to monitor the concentration of CO₂ while being seamlessly integrated with existing ventilation systems. Among the potential gas sensing technologies available, microelectromechanical systems (MEMS) gas sensors (i.e., electrochemical, acoustic, and optical sensors) are a promising avenue for low-cost and small-scale gas sensing applications [89], [157]–[160]. In particular, adsorption-based electrochemical and electromechanical gas sensors have demonstrated potentials for carbon dioxide

(CO₂) monitoring in buildings [119], [161]–[165], which is a market that has historically been dominated by optical non-dispersive infrared (NDIR) sensors [32], [35], [40], [97], [166]. In principle, in electrochemical and electromechanical gas sensor devices, the adsorption of a target gas analyte onto a chemically selective recognition layer induces a physical property change in the material, which is then transduced into a signal by the gas sensor. This physical property change can be a change in conductivity (i.e., electrochemical devices) or a change in mechanical behavior (i.e., resonance frequency). Thus, the careful selection of a chemical selective recognition layer allows for a selective gas sensor for CO₂ that is compatible with modern IAQ monitoring needs (e.g., low-power devices).

Among the potential chemically selective materials for CO₂ sensing, poly(ethyleneimine) (PEI) is an intriguing polymer as PEI can capture, and even store, CO₂ [62], [63], [65], [66], [99], [167]–[169]. This viability, in part, is because PEI contains primary and secondary amines that reversibly interact with CO₂ via acid-base redox reactions [133], [135], [136]. The ability of PEI to reversibly adsorb CO₂ makes it an attractive candidate for sensing applications [49], [68], [70], [95], [134], [161], [170]–[173]. Further, the blending of additives into a PEI matrix can enhance the uptake of CO₂ in the materials system [70], [71], [134], [145], [146]. This is thought to occur because the additives disrupt intrachain and inter-chain amine entanglements in the PEI matrix, which increases the available number of PEI surface sites that interact with CO₂ molecules. For example, PEI combined with starch is more effective than PEI alone for developing CO₂ sensors [70], [134]. Additionally, PEI and poly(ethylene oxide) (PEO) blends have enhanced CO₂ uptake relative to pristine PEI thin films [119]. These results are important as they provide performance metrics relevant to CO₂ monitoring for a conditioned indoor environment. However, the sensing of CO₂ with a PEI-PEO polymer blend is still limited for IAQ monitoring because the materials system was only evaluated across a limited temperature range of 4° C, whereas a much larger temperature range is appropriate for indoor applications. Furthermore, data across a larger temperature range is desirable for determining temperature-related sensor dependencies and optimizing sensing material performance. Thus, characterizing the temperature-dependent adsorption kinetics of CO₂ for this polymer platform provides critical information for this polymer system in terms of a promising end-use application.

Here, we evaluate the role of temperature on the sorption kinetics of CO₂ into PEI-PEO blends that have been deposited on a small-scale electromechanical resonant mass sensor to determine the underlying environmental factors that impact the practical application of the sensor. To achieve this aim, measurements were made across an extended temperature range, to better understand and characterize the polymer blend response. Using these data, the temperature-dependent kinetics of the resonant mass sensor functionalized with a PEI-based material were determined in a manner similar to other quartz crystal microbalance-based (QCM-based) adsorption kinetic studies [174]–[177]. In this way, this study establishes the robust performance of PEI-based polymer blends, quantifies key sorption characteristics, and provides a means by which to further develop low-cost and small-scale CO₂ sensors for indoor environments.

5.2 Experimental Methods

5.2.1 Materials

All of the chemicals used in this study were purchased from Sigma-Aldrich, and they were used as received unless otherwise noted. The hyperbranched PEI utilized has a reported weight-average molecular weight of 25 kg mol⁻¹. The PEO utilized was purchased from Alfa Aesar, and the weight-average molecular weight of the PEO was 100 kg mol⁻¹. The methanol utilized to prepare the polymer samples was anhydrous grade and stored under nitrogen.

5.2.2 General Methods

A Hitachi S-4800 Field Emission scanning electron microscope (SEM) was utilized to image the polymer samples. For these images, 1.0 μL of a 1 mg mL⁻¹ polymer blend in methanol solution were drop-cast on polished silicon dioxide substrates and dried overnight under vacuum. The films were then coated with 20 nm of carbon prior to imaging using a SPI carbon sputter coater to prevent charging during image acquisition. For the samples that were heated, the polymer films were heated to greater than 343 K (with a maximum temperature of 423 K) and held to isotherm for 15 minutes. The samples were then im-

mediately sputter coated with 20 nm of carbon prior to imaging. Attenuated total internal reflectance-Fourier transform infrared (ATR-FTIR) spectroscopy was performed using a diamond substrate of a Thermo-Nicolet Nexus FTIR, using a deuterated triglycine sulfate KBr detector with a KBr beam splitter. Under a dry nitrogen purge, 100 scans were acquired over a range of $800\text{ cm}^{-1} \leq \nu \leq 4500\text{ cm}^{-1}$ for each sample. X-ray diffraction (XRD) measurements were measured with a Rigaku Cu-K α source ($\lambda=1.54056\text{ \AA}$) in parallel beam mode. These samples were acquired while under ambient conditions. The polymer film samples were fabricated using a 240 mg mL^{-1} solution of the polymer blend (by weight ratio) in methanol pipetted into a metal mold and then annealed at 353 K while being pressed for at least 10 minutes. After pressing, these films were dried overnight under vacuum ($P \leq 0.4$ Torr) prior to XRD analysis being performed. A TA Instruments Q20 Series differential scanning calorimeter (DSC) was used for thermal transition analysis. The samples were sealed in Tzero hermetic pans, were first annealed at 348 K under a nitrogen gas purge, and then cooled to 213 K, before the trace that started at 213 K and ended at 348 K at a scan rate of 1.1 K min^{-1} was collected.

5.2.3 Experimental Adsorption Apparatus and Procedure

The testing protocols utilized in this work are similar to those previously reported [119]. Experiments were performed using the setup shown in Figure 5.1. Gas tanks of nitrogen and 1% CO₂ and 99% nitrogen were connected to a series of mass flow controllers (MFC; MKS, 1179C) in parallel. The polymer blend-based resonant mass sensors were enclosed in a test chamber with an approximate volume of 163 cm^3 . A recirculating chiller (Thermo Fisher; Polar Series Accel 500 LT) and custom thermal blanket were utilized for temperature control of the test chamber. The recirculating chiller provided a working temperature range of 248 K to 353 K. Prior to data collection at each test condition, the test chamber was flushed with nitrogen for 3 hours at each reported temperature to allow the chamber to reach a steady-state baseline condition. Then, CO₂ gas was injected into the chamber to achieve the reported concentrations. A frequency counter was developed in LabVIEW to monitor the oscillation frequency of each oscillator with a 1 Hz resolution.

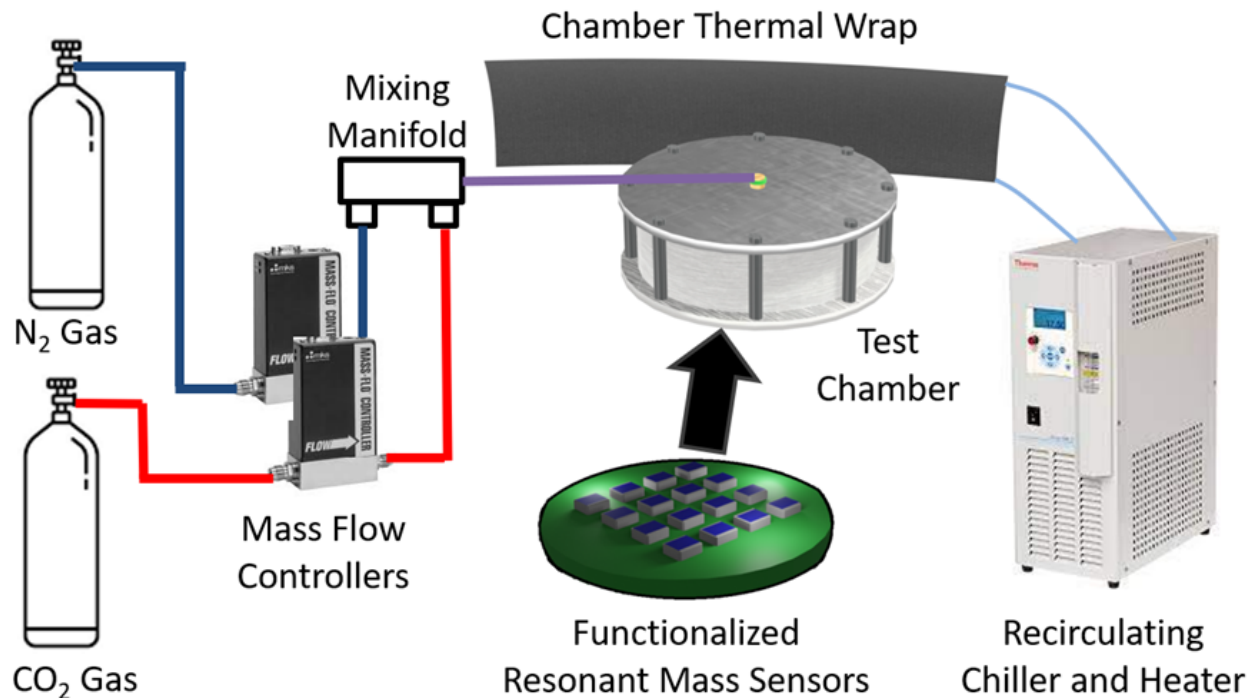


Figure 5.1. Schematic of the experimental setup used for sensor characterization. The mass flow controllers (MFCs) modulated supply gases to the test chamber containing the functionalized resonators. A recirculating heater/chiller and a thermal wrap were used to regulate the temperature of the test chamber at the reported conditions.

5.2.4 Device Fabrication

The device instrumentation utilized in this work was previously reported [119]. This included a small-scale resonator (Kyocera Corp., CX3225) and a crystal oscillator driver (Texas Instruments, SN74LVC1GX04) implemented in a Pierce oscillator circuit. Upon construction of the oscillator circuit, the cap on the resonator packaging was removed to expose the resonant element for functionalization. To coat a pristine PEI thin film, a solution of 0.1% (by volume) of PEI in methanol was created. For creating the 3:1 PEO:PEI thin films, PEI and PEO were dissolved in methanol to generate a solution of 0.1% (by volume) of PEI and 0.3% (by volume) of PEO. Then, 1 μ L of each solution was deposited onto each respective resonator. The resonators were then placed under vacuum at 343 K for 24 hours

to remove any residual methanol leaving behind PEI and the 3:1 PEO:PEI blend, on each respective substrate.

5.2.5 Adsorbed Mass and Resonance Frequency Correlation

Resonance frequency measurements of the small-scale resonators were employed to monitor the CO₂ sorption process. As CO₂ adsorbs on the resonator (increasing the total mass) the oscillation frequency of the resonator decreases, allowing real-time monitoring of the sorption kinetics. The observed frequency shift is correlated to the deposited mass by [117], [178]:

$$\Delta m = \frac{\Delta f}{S_m f_0}, \quad (5.1)$$

where Δm is the change in mass, S_m is the mass sensitivity of the sensor, f_0 is the resonance frequency of the unloaded resonator, and Δf is the change in resonance frequency. Thus, an increase in the mass of CO₂ adsorbed would result in a proportional decrease in resonance frequency.

5.3 Results and Discussion

5.3.1 Characterization of Polymer Blend

As shown previously, a 3:1 PEO:PEI polymer blend, when drop cast and dried on a resonant mass sensor, yields a nanoscale structure that affords high-performing, robust, and reliable CO₂ gas detection sensors [119]. This detection is possible due to the crystalline features of PEO which can induce pores into a PEI matrix by disrupting the strong intermolecular amine interactions that can limit the interaction of CO₂ with the polymer matrix. When the amines are disrupted, the CO₂ gas can then better interact with primary and secondary amines in PEI and transduce a response to the resonator. This pore formation, occurring at ambient temperatures, is observed via SEM imaging (Figure 5.2a). However, it is important to note that this detection of CO₂ gas is reliant on PEO maintaining its crystalline structure and keeping the interchain and intrachain amines accessible to interact with

CO₂. At elevated temperatures (i.e., $T > 343$ K), there is a loss of the porous features in the polymer film as observed in SEM imaging (Figure 5.2b). This implies that the polymer film at elevated temperature conditions is entering a melt state in which there is a disappearance of PEO crystalline features and the reformation of strong amine intermolecular forces in the polymer matrix. Thus, it is important to maintain an operation temperature in which the polymer is not melted, and the porous structure is maintained, as it allows for CO₂ to diffuse into the polymer matrix and interact with free amine moieties.

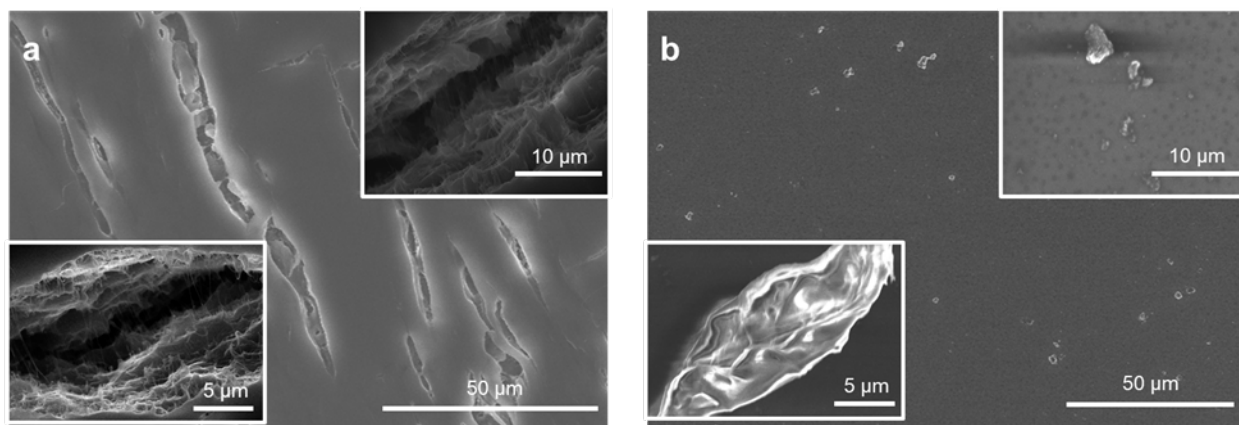


Figure 5.2. SEM images of a 3:1 PEO:PEI blend film. (a) Room temperature image of the polymer film. These images are highlighting the micron-sized pores formed in the polymer matrix. All of the images shown are of the same film but in different sections and locations. (b) A polymer film exposed to temperature greater than 343 K, isotherm for 15 minutes, and then imaged. These images are highlighting the melting of the polymer film and the loss of porous structure. All of the images shown are of the same film but in different sections and locations.

FTIR analysis showed that there were distinct features of both PEI and PEO expressed in the 3:1 PEO:PEI polymer film (Figure 5.3a). PEI N-H stretching (3270 cm^{-1}), PEO C-H stretching (2880 cm^{-1}), PEI N-H bending (1580 cm^{-1}), PEO C-C stretching (1475 cm^{-1}), PEO O-H bending (1380 cm^{-1}), PEO CH₂ wagging (1310 cm^{-1}), and PEO C-O-C stretching (1090 cm^{-1}) were observed. These spectra peak locations are consistent with previous FTIR analysis studies of PEO and PEI [168], [179]–[181]. The combination of PEO and PEI features expressed in the 3:1 PEO:PEI film without any shifts or alterations in peak locations implied that there were no chemical bond formations occurring in the polymer blend; rather,

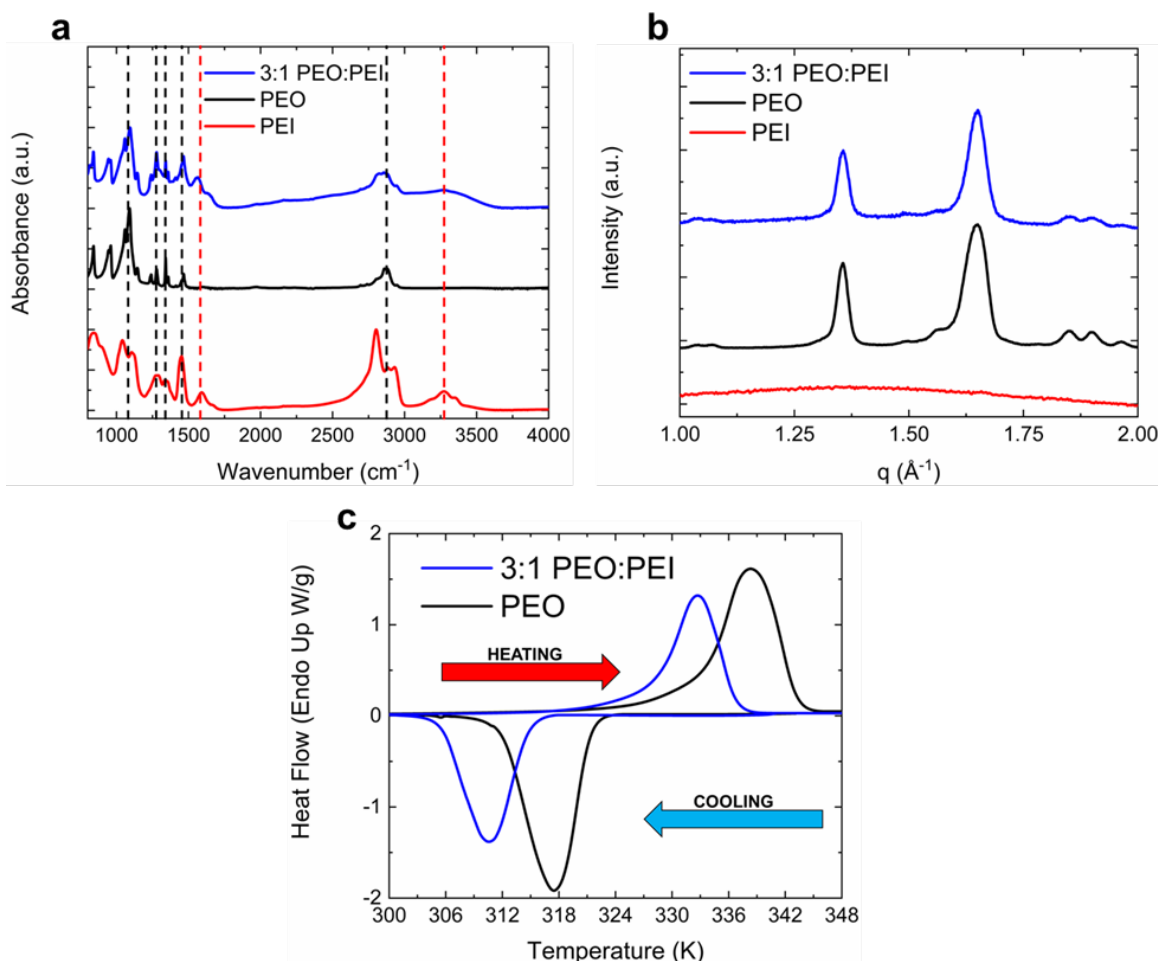


Figure 5.3. (a) FTIR spectra of PEI, PEO, and 3:1 PEO:PEI polymer films. Dashed lines highlight the spectrum peaks at 3270 cm^{-1} , 2880 cm^{-1} , 1580 cm^{-1} , 1475 cm^{-1} , 1380 cm^{-1} , 1310 cm^{-1} , and 1090 cm^{-1} , which occur in the 3:1 PEO:PEI polymer sample corresponding to the peaks in PEO and PEI. (b) XRD patterns of PEI, PEO, 3:1 PEO:PEI blend films. Highlighting the crystal structure of PEO expressed in the 3:1 PEO:PEI polymer film. (c) DSC heating and cooling traces of PEO and 3:1 PEO:PEI polymer films, highlighting that PEO has a T_m of 338.15 K and T_c of 317.15 K while a 3:1 PEO:PEI film has a T_m of 331.15 K and a T_c of 310.15 K . Upon integration, 3:1 PEO:PEI heating and cooling peaks were 70% of the PEO peaks area, respectively.

this was a miscible polymer blend. XRD analysis showed that a 3:1 PEO:PEI film expressed the monoclinic crystal structure of PEO [148], [149]. These characteristics occurred at $q = 1.3 \text{ \AA}^{-1}$ and $q = 1.65 \text{ \AA}^{-1}$ (Figure 5.3b). There were no crystalline features observed in the PEI because the branched PEI was an amorphous polymer. Notably, the DSC traces of the materials showed features which correspond to the melting and crystalline properties of PEO and the 3:1 PEO:PEI polymer blend (Figure 5.3c). DSC heating traces of the polymer films showed that PEO has a melting point (T_m) of 338 K and 3:1 PEO:PEI has a T_m of 331 K. PEI, a hyperbranched polymer, when incorporated into PEO did not allow for PEO to pack its polymer chains as efficiently and thus this lowered the packing density and the melting point in the 3:1 PEO:PEI polymer blend. This is interesting as it corresponded to the SEM image (Figure 5.2b), which showed melting features as the 3:1 polymer film was heated past 333 K and lost its porosity in the polymer film.

Additionally, in the DSC cooling trace, PEO had a crystallization temperature (T_c) of 317 K while a 3:1 PEO:PEI film had a T_c of 310 K owing again to the hyperbranched nature of PEI being incorporated into the polymer blend. This hyperbranched structure of PEI did not allow for PEO to maintain its packing of polymer chains and thus it formed its crystalline structure at a lower temperature (Figure 5.3c). Upon integration of these heating and cooling traces, the 3:1 PEO:PEI showed an integration value of 70% of the intensity of PEO in both the heating and cooling traces, individually. Overall, a 3:1 PEO:PEI polymer blend showed chemical and structural features of both PEO and PEI. These features play a critical role in the performance of detecting and interacting with CO_2 . Additionally, it is important to note that a 3:1 PEO:PEI polymer blend offers optimal performance under conditions that are likely to be encountered in an interior location.

5.3.2 CO_2 Adsorption-Desorption Profiles

To determine if these structural characteristics were impacting sensor performance, the CO_2 adsorption-desorption performance was measured across CO_2 concentrations between 0% and 1% for both pristine PEI thin films and the 3:1 PEO:PEI blend thin films. A sample time-series depiction of the frequency data (Figure 5.4) shows the sorption characteristics of

the device and that it is a reversible process. The addition of CO₂ results in a rapid decrease in the resonance frequency of the device as CO₂ interacts with the PEI and increases the total mass of the resonator. Upon removal of CO₂, immediate desorption occurs, and the resonance frequency of the device increases, due to a decrease in total mass.

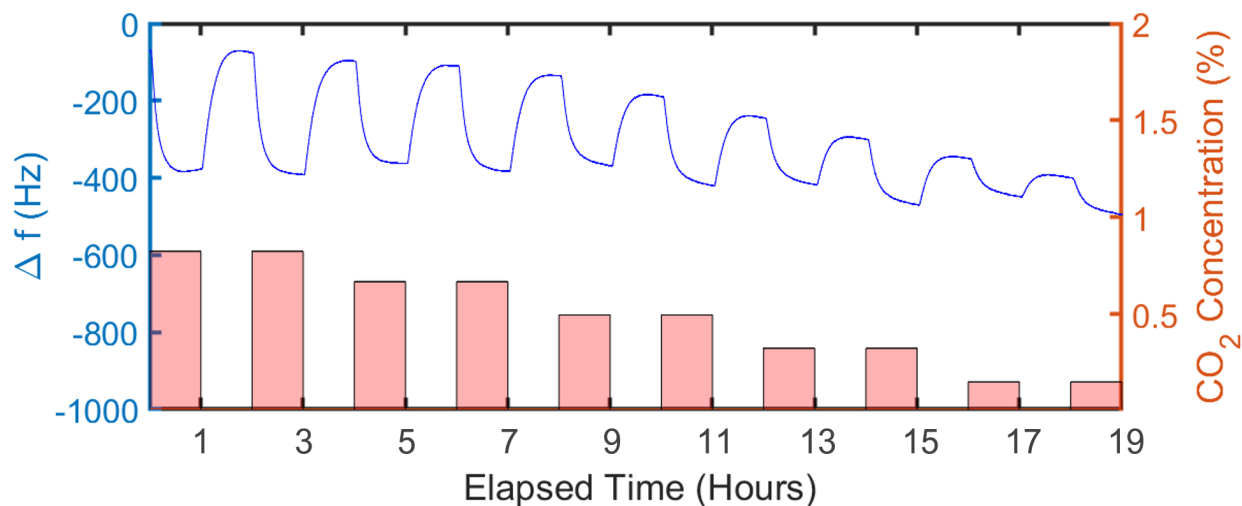


Figure 5.4. Representative time-series data showing the response of 3:1 PEO:PEI functionalized resonator to concentrations of CO₂ between 0% and 1% in a 325 K environment.

Figure 5.5a and Figure 5.6a show the adsorption-desorption profiles of a 3:1 PEO:PEI blend film and of a pristine PEI film, respectively, for 4 consecutive 1 hour cycles across a range of temperatures relevant to indoor CO₂ monitoring. A clear trend of increasing temperature causing a decrease in the net amount of CO₂ adsorbed, relative to the available PEI, is seen. Further, during the four consecutive adsorption-desorption cycles, there was no sign of deteriorating sorbent behavior. This stability is consistent with other studies on PEI-functionalized solid sorbents where materials persisted after numerous adsorption-desorption cycles [99], [182], [183]. As shown in Figure 5.5b and Figure 5.6b, this trend continued across a range of CO₂ concentrations for each temperature condition, as indicated by the small error bars (representing one standard deviation from the average).

Notably, the resonator coated with a 3:1 PEO:PEI blend (Figure 5.5) is more sensitive to both changes in CO₂ concentration and changes in temperature, as compared to the resonator coated with pristine PEI (Figure 5.6). The CO₂ concentration sensitivity is due, in part,

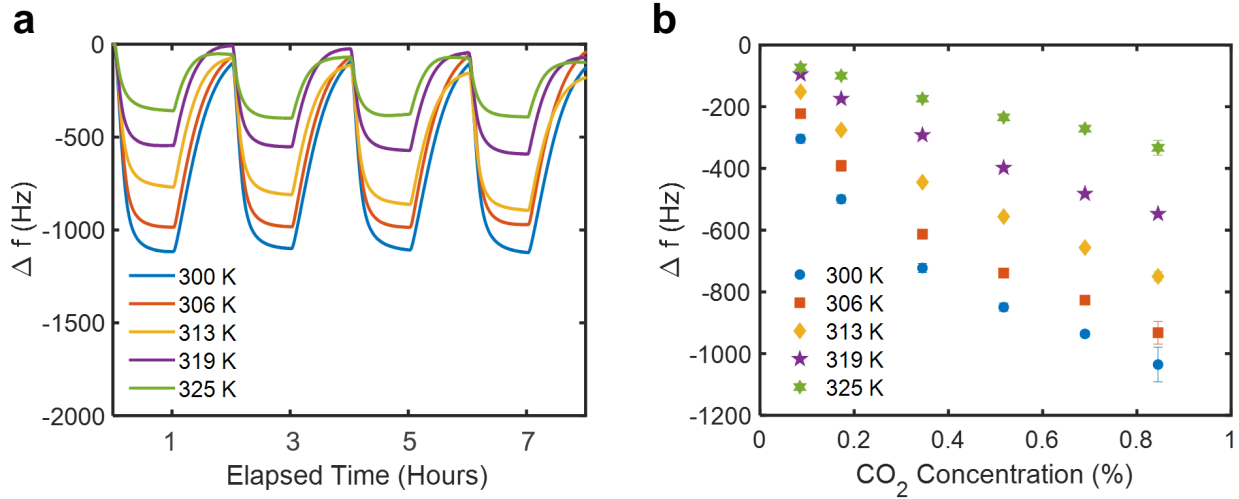


Figure 5.5. (a) CO_2 adsorption-desorption cycles at various temperatures for a 3:1 PEO:PEI functionalized resonator in response to 1 hour on/off pulses of CO_2 at a concentration of 0.84%. (b) The mean resonance frequency shift after 1 hour of CO_2 exposure at various concentrations for a 3:1 PEO:PEI functionalized resonator. The error bars represent one standard deviation of the data from the average value.

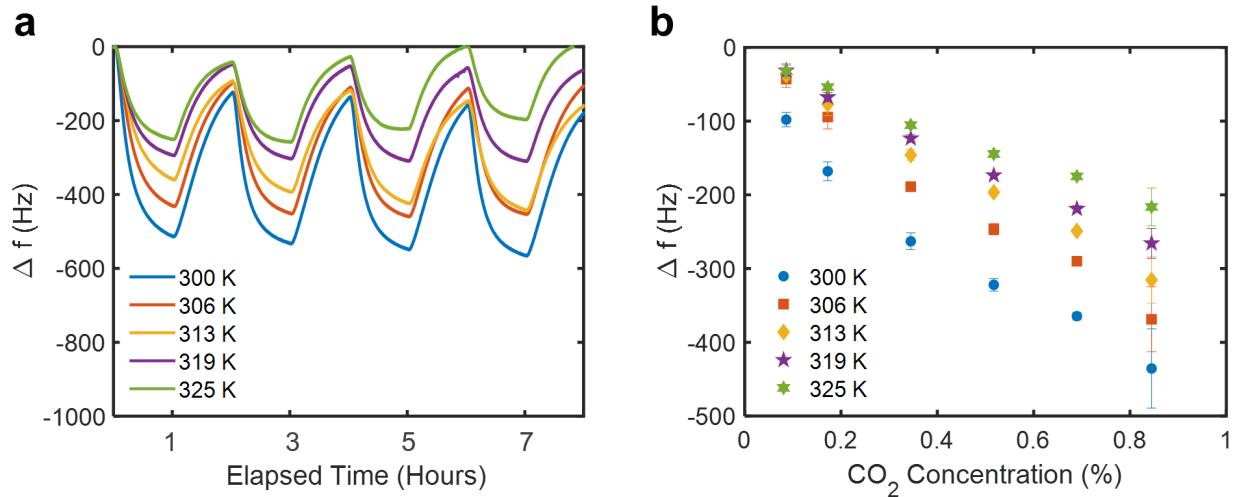


Figure 5.6. (a) CO_2 adsorption-desorption cycles at various temperatures for a PEI functionalized resonator in response to 1 hour on/off pulses of CO_2 at a concentration of 0.84%. (b) The mean resonance frequency shift after 1 hour of CO_2 exposure at various concentrations for a PEI-functionalized resonator. The error bars represent one standard deviation of the data from the average value.

to PEO disrupting intrachain and interchain PEI amine entanglement (Figure 5.2a). This disruption allows for the more accessible amines to interact with CO₂, resulting in increased sensitivity to available CO₂. Further, the temperature dependence can be corroborated with a starker decrease in accessible amines with increasing temperature [145]. As temperature increases in the system, the polymers begin to melt with an onset melting point as low as 322 K in a 3:1 PEO:PEI polymer blend (Figure 5.3c). This melting causes the porous structure in the polymer film to disappear (Figure 5.2b). Hence, the disruption PEO induced into the PEI polymer matrix no longer occurs because PEO has lost its crystalline texture (Figure 5.3c). This higher temperature sensitivity of the 3:1 PEO:PEI polymer blend compared to PEI alone indicates that the system may be thermodynamically controlled, and kinetic effects play less of a role in a PEI-dilute system.

5.3.3 Analysis of CO₂ Sorption Kinetics

As shown in Figures 5.4 and 5.5a, a 3:1 PEO:PEI coated resonator responds in a reversible manner with respect to changing CO₂ concentration (i.e., a certain partial pressure). The surface coverage of PEI-based materials is governed by a balance of the adsorption and desorption of CO₂, and fit well with a Langmuir model [184], [185]. Thus, the change of surface coverage θ of the molecules can be described by a Langmuir equation,

$$\frac{d\theta}{dt} = k_a(1 - \theta)C - k_d\theta, \quad (5.2)$$

where k_a and k_d are the adsorption and desorption rate constants (respectively) and C is the concentration of CO₂. Integrating Equation 5.2 we have

$$\theta(t) = \frac{C}{(C + k_d/k_a)}[1 - e^{-(k_a C + k_d)t}], \quad (5.3)$$

which illustrate the time dependence of the surface coverage after the concentration change, as a new equilibrium value is approached. In Equation 5.3, setting

$$k_{obs} = k_a C + k_d \quad (5.4)$$

and

$$k_q = \frac{C}{(C + k_d/k_a)}, \quad (5.5)$$

results in

$$\theta(t) = k_q(1 - e^{-k_{obs}t}). \quad (5.6)$$

Equation 5.6 shows that the surface coverage approaches the equilibrium value exponentially, which matches the time-series data shown in Figures 5.4 and 5.5a. As shown in Equation 5.1, the frequency shift of the resonator is proportional to the mass of adsorbed CO₂, and thus, may be assumed to be proportional to the change in fractional coverage on the polymer surface. Therefore, if the fractional surface coverage θ is measured as a function of time t , k_{obs} and k_q can be determined by fitting the (negative) frequency shift of the resonator to Equation 5.6 (Figure 5.7a). Further, considering Equation 5.4, a plot of k_{obs} vs. C (Figure 5.7b) yields a line with slope k_a and intercept of k_d . By definition, the equilibrium constant K_{eq} for this process is

$$K_{eq} = k_a/k_d. \quad (5.7)$$

Thus, the free energy of adsorption ΔG_{ads} at a given temperature can be found directly from the equilibrium constant

$$\Delta G_{ads} = -RT \ln K_{eq}. \quad (5.8)$$

Figure 5.7d shows the calculated free energy of adsorption for both a PEI functionalized resonator and a 3:1 PEO:PEI functionalized resonator. Because

$$\Delta G_{ads} = \Delta H_{ads} - T\Delta S_{ads}, \quad (5.9)$$

both ΔH_{ads} and ΔS_{ads} can be determined by carrying out this analysis over a range of temperatures and plotting ΔG_{ads} vs. T (Figure 5.7d). The negative values for ΔG_{ads} and ΔH_{ads} denote that the reaction occurs spontaneously and is exothermic; which is consistent with other CO₂-PEI adsorption studies [186]–[188].

Figure 5.8 shows Arrhenius plots for the adsorption and desorption constants (k_a and k_d) that were obtained from the data in Figures 5.7b and 5.7c. Notably, across the measured

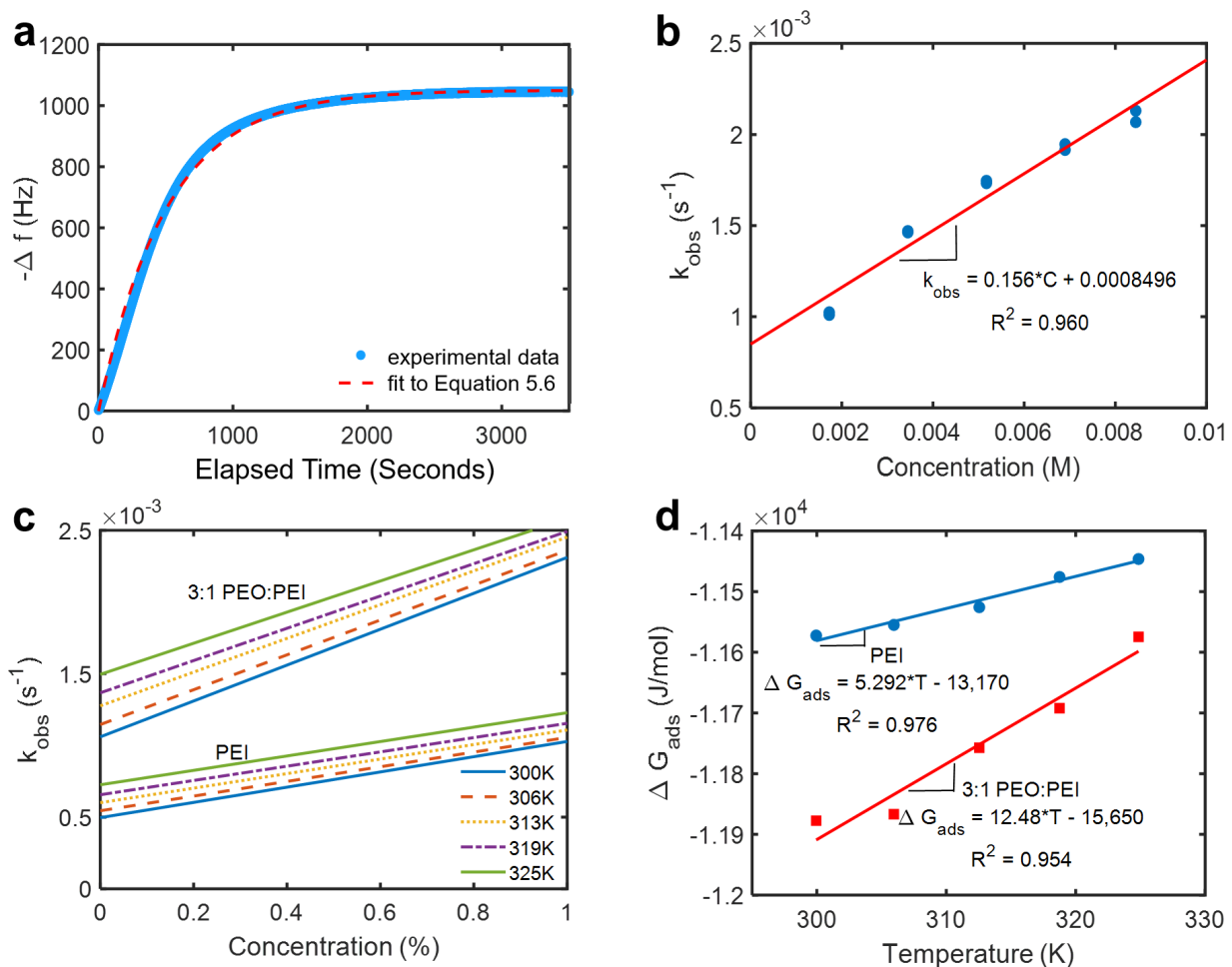


Figure 5.7. (a) A fit of the Langmuir adsorption isotherm (Equation 5.6) to frequency data of a 3:1 PEO:PEI functionalized resonator at a concentration of 0.84% CO_2 and in a 300 K environment. (b) Fit to calculated k_{obs} for a 3:1 PEO:PEI functionalized resonator in a 300 K environment. (c) Fitted relationship between k_{obs} and CO_2 concentration for pristine PEI and a 3:1 PEO:PEI blend for temperatures ranging from 300 K to 325 K. (d) Calculated Gibbs free energy at each temperature condition for pristine PEI and a 3:1 PEO:PEI blend.

temperatures, k_a is relatively constant while k_d increases with increasing temperature. This suggests that the decrease in sensor response is due, in part, to a faster desorption rate at higher temperatures. Further, the rate constants for the PEI and 3:1 PEO:PEI blend functionalized resonators showed similar trends with respect to temperature. However, the trends are slightly shifted owing to the shorter time response of the 3:1 PEO:PEI functionalized resonator relative to the resonator functionalized with only PEI. This is, in part, due to PEO disruption of the intermolecular chains of PEI, which makes the free amines more readily available to interact with CO_2 .

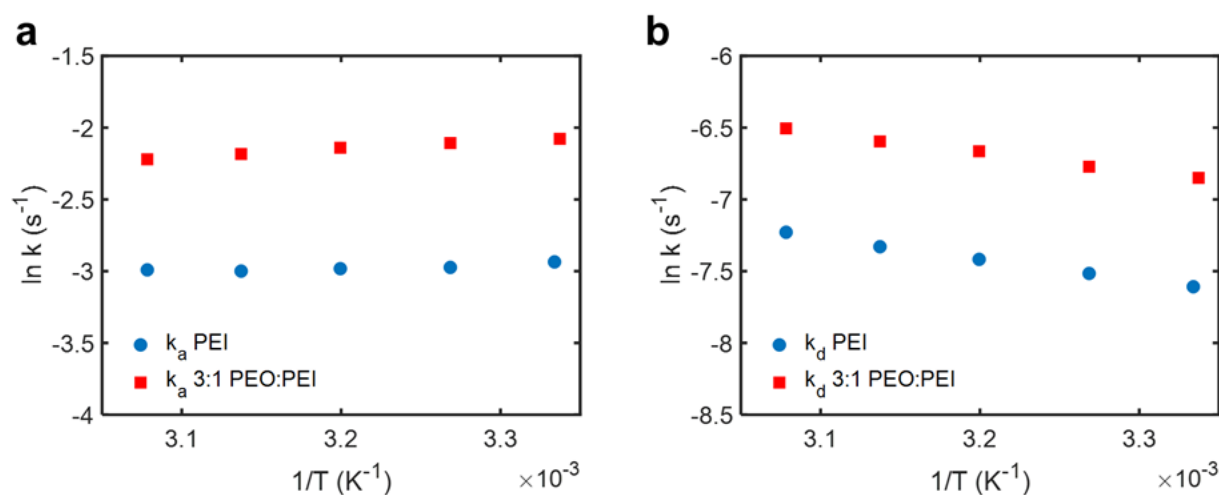


Figure 5.8. Arrhenius plot showing (a) k_a and (b) k_d for PEI alone and a 3:1 PEO:PEI functionalized resonator. Notably, k_a is relatively constant while k_d increases with increasing temperature. Thus, the decrease in response can partly be attributed to a faster desorption rate at higher temperatures.

6. IMPLEMENTING CO₂ SENSORS IN THE BUILT ENVIRONMENT AND DIRECTIONS FOR FUTURE WORK

6.1 Introduction

When considering CO₂ sensing in smart building applications, there are a number of open questions as to how to effectively capture data. The effectiveness of CO₂-based demand controlled ventilation or other CO₂-informed smart building controls, can be limited by the speed and accuracy that CO₂ data is obtained. This problem can be investigated at several scales; in particular, at the sensor level (small-scale) and the room level (large-scale). The work presented thus far was primarily conducted at the sensor level. As detailed in Chapters 2-5, metrics such as the sensor response time and sensitivity were investigated under different environmental conditions in a well-controlled benchtop testing system. While the initial development of these sensors has primarily focused on sensor-level characteristics, the room-level characteristics have been largely ignored. Thus, next steps should investigate how to integrate these sensors into the built environment.

At the room level, air-flow dynamics, diffusion, and the distance between a CO₂ generation source and the sensor become important. Things like sensor location and the number of installed sensing nodes can largely influence how a space is characterized. Further, given recent CO₂ sensor developments (including those presented in Chapters 2-5), new heuristics can be developed that consider the use of a CO₂ sensor in buildings that is truly low-cost and low-power. Therefore, future work should investigate the nuances of sensor location and the number of sensors necessary to define a space.

Next, it is recognized that the real-world implementation of sensing instruments can be messy. In particular, gas sensors are prone to external influences, such as dust, air-flow dynamics, temperature, humidity, and pressure. Therefore, it is recommended that appropriate compensation of these factors is considered for the practical implementation of the sensors developed herein. To do so, it is necessary to perform live and at-scale testing of these devices, and compare them head-to-head with commercial sensing technologies.

Finally, with the advent of smart buildings and internet of things (IoT) connected sensors, there are new opportunities to improve building operation and safety [14]. For example, CO₂

sensing for occupancy detection has been suggested as a means of providing localized comfort control [17]–[19]. Further, with recent advancements in the development of low-cost and low-power gas sensors for building applications (including those described in Chapters 2-5) there are new opportunities for monitoring indoor air spaces. Namely, IAQ can be cost-effectively monitored via wireless sensor networks (WSNs) with a high degree of resolution; which is particularly applicable for gas source identification and localization. In particular, CO₂ monitoring can be implemented as a non-discriminatory means of occupancy recognition, counting, and localization. Thus, the appropriate use of CO₂ sensor networks may be a promising avenue for occupant localization indoors.

The remainder of this chapter seeks to provide preliminary results to address these issues and provide suggested directions for future work in this space. To do so, data was collected in a full-scale environmental test chamber as a proof-of-concept reference point. Section 6.2 provides a brief literature review and suggestions for future research regarding the placement of CO₂ sensors in buildings. Section 6.3 presents a room-sized environmental test chamber and presents initial data on a PEI-PEO functionalized resonator (Chapters 4-5) operating in this space. Lastly, Section 6.4 demonstrates the basic feasibility of using CO₂ WSNs for occupant localization and informs future work on CO₂ sensor networks in the built environment.

6.2 Placement of CO₂ Sensors in the Built Environment

Placing a CO₂ sensor within a building is a non-trivial task with several constraints and considerations. To date, cost and sensor power have been the driving constraints to this problem, where cost limits the number of sensors used and sensor power requirements dictate that the sensors are located near a steady power source. With recent sensor developments, including those described in Chapters 2-5, these cost and power constraints are being relaxed, which creates opportunities for more detailed sampling of CO₂ in the built environment. Such details may be utilized for both modeling and control purposes. Furthermore, the addition of sensor nodes will reduce the time to obtain actionable information about the ventilation zone.

Several previous studies have developed heuristic rules for sensor placement, based on investigations of CO₂ distribution within a space. Stymne *et al.* performed a study on dispersion patterns in displacement ventilated rooms [189]. It was concluded that CO₂ sensors should preferably be positioned at a height slightly above the head of occupants to ensure acceptable air quality in the breathing zone. Pei *et al.* studied the effect of CO₂ sensor position in a room through the assistance of experimentally validated CFD modeling [190]. This study investigated the effects of ventilation strategy, air change rate, and the number of occupants on the distribution of CO₂ in a room. The study found that under mixing ventilation, the sensor location typically has marginal influence on the measurement due to a fairly uniform CO₂ distribution, both horizontally and vertically. However, under displacement ventilation, a vertical gradient in CO₂ distribution was evident, posing a significant difference in measurements based on sensor location. This result is in agreement with the study performed by Stymne *et al.* which similarly found a vertical distribution with displacement ventilation. Similarly, Rackes *et al.* used airflow simulations to explore the advantages of multiple sensors to capture spatial variation in small offices. The study found additional sensors lead to minimal reductions in overall sensing error unless there was low supply airflow [191].

Alternative to heuristic sensor placement, several studies have developed methods which optimally place sensors based on computational constraints. Fontanini *et al.* developed an algorithm for determining optimal sensor location for contaminant tracking. The study considered three air flow fields simulated with CFD to maximize the coverage of 1-4 sensors [192]. Rather than physics-based CFD models, data-driven approaches have also been used for tackling the optimal sensor placement problem. Yoganathan *et al.* utilized clustering algorithms to determine optimal sensor placement for office buildings [193]. This study utilized an exhaustive number of temperature, relative humidity, and luminance sensors to completely cover the space and obtain the necessary data. However, CO₂ measurements were not considered in this study.

Though several studies have touched on optimal sensor placement, there are still opportunities to address this issue. Heuristic rules for sensor placement are generally helpful, but often breakdown in atypical situations. Computational strategies can be employed to

determine optimal sensor placement in a specific and well-defined space; however, the tools necessary to perform such optimization calculations are often not available to the average building owner. Data-driven optimization of sensor placement via low-cost wireless CO₂ sensors may be a promising pathway but, as of this writing, has not been fully investigated. Further, regardless of the optimization process, the optimal placement of a CO₂ sensor will likely depend on the specific sensing technology employed. More precisely, different sensing technologies differ in how external factors interfere with their output (e.g., heat, humidity, vibrations, etc.). Therefore it is recommended that the effect of sensor placement in indoor environments is further explored. More specifically, it is recommended that these effects are studied for the sensors described in Chapters 2-5, as their suitability may be significantly affected by their location in a building. Thus, along with full-scale testing, future work might consider investigating the location dependencies of these sensors.

6.3 Full-Scale Sensor Testing

The sensors developed herein performed well in a benchtop testing system, however, they were not fully characterized in a larger environment. Therefore, to begin testing these sensors in a more realistic environment, a room-sized (16 ft x 14 ft 2 in. x 9 ft) indoor air quality chamber (IAQC) was used (Figure 6.1). The IAQC had complete control of all heating, ventilation, and air conditioning (HVAC) parameters including air flow, temperature, and humidity. The IAQC was constructed with a well-insulated ceiling, floor, and walls to isolate the indoor environment from any potential effects of external temperature fluctuation. Additionally, the chamber was equipped with a 500 cfm (14 m³/min) supply fan and return fan. This configuration simulated a small and simple room, with one supply duct near the floor and one return duct in the ceiling.

A prototype version of the PEI-PEO functionalized resonant mass sensing system (Chapter 4) was installed in the IAQC for more realistic, at-scale testing (Figure 6.2). To prepare the prototype sensors for implementation in the IAQC, a paper filter was placed over the sensing elements to remove air contaminants (oil, dirt, etc.), and to protect against dust and



Figure 6.1. Indoor air quality chamber (IAQC) utilized for full-scale sensor testing.

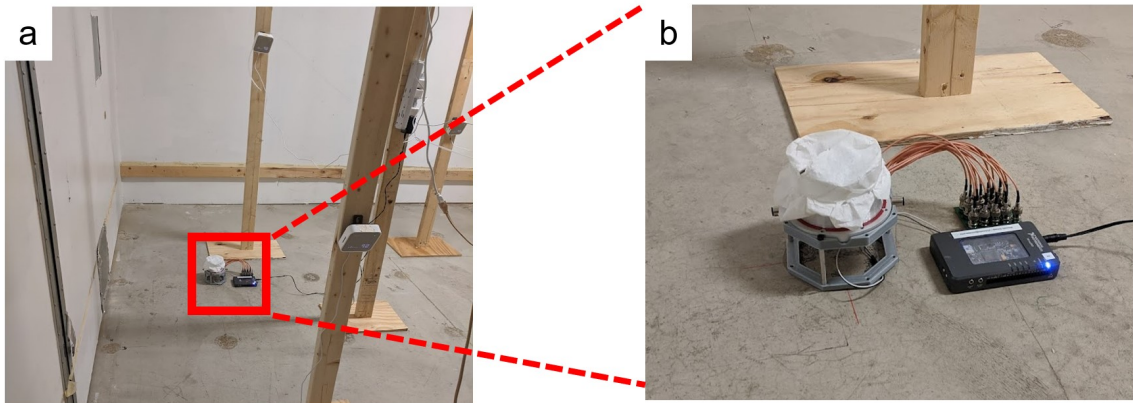


Figure 6.2. (a) A zoomed out and (b) zoomed in picture of the prototype CO₂ sensing system and commercial CO₂ sensors in the IAQC. A paper filter was placed over the prototype sensing elements to serve as a protective dust shield.

unstable airflow. For direct comparison, two commercial CO₂ sensors (Sensirion SCD41, Telaire T6713) were co-located with the prototype sensors.

For initial testing, the IAQC was regulated to circulate outdoor air at a rate of 3 ACH. CO₂ was then injected into the IAQC in 1 hour on/off pulses. This provided a wide range

of indoor CO₂ concentrations, alternating from fresh, outdoor air (the low end of expected indoor CO₂ concentrations), to nearly 2,000 ppm (the upper end of expected indoor CO₂ concentrations). A time-series plot of this test is shown in Figure 6.3. Here, the left axis and blue line correspond to the raw frequency shift of a prototype CO₂ sensor and the right axis and red lines indicate the measured CO₂ concentration of the two commercial CO₂ sensors that were co-located with the prototype sensor. Prior to any signal filtering, the raw frequency data of the prototype sensor demonstrated a similar response time and stability to the co-located commercial CO₂ sensors, which is a promising result.

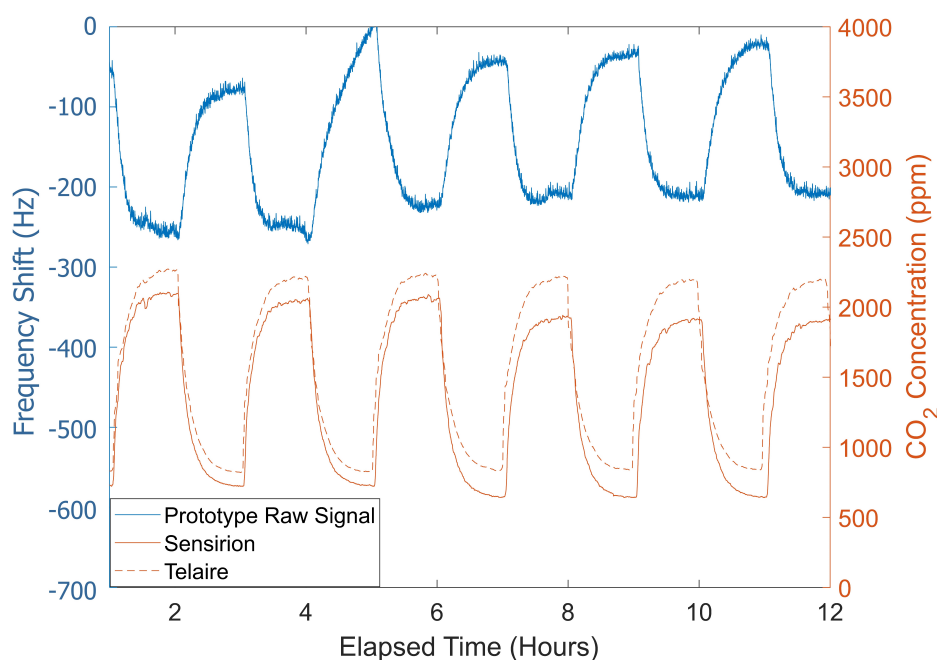


Figure 6.3. Comparison of prototype sensor with commercial CO₂ sensors in the IAQC. The left axis and blue line correspond to the frequency shift of the prototype CO₂ sensor. The right axis and red lines indicate the measured CO₂ concentration of two commercial CO₂ sensors that were co-located with the prototype sensor.

Although promising, these data simply show a first-level proof of viability for the PEI-PEO functionalized resonant mass sensors in a full-scale environment. Therefore, the next step on the path to commercial viability for these sensors is to perform full-scale testing across a range of temperature, humidity, and CO₂ concentrations, similar to the bench top experiments described in Chapters 2-5. These tests should be performed for both the

chemiresistive and resonant mass sensors, to discover and appropriately compensate for any nuances associated with full scale environments. Such data is necessary to ensure a robust and accurate sensor in the final phase of development.

6.4 Occupant Localization via CO₂ Sensor Networks

With recent advancements in the development of low-cost, low-power gas sensors for building applications, including those described in Chapters 2-5, there are new opportunities for monitoring indoor air spaces. Namely, CO₂ can be cost-effectively monitored via wireless sensor networks (WSNs) with a high degree of resolution; which is particularly applicable for gas source identification and localization. Prior gas source isolation efforts have typically relied on inverse modeling along with computational fluid dynamics (CFD) analysis [194]–[197]. Though promising, such methods can be computationally expensive and access to CFD software remains a barrier for many building operators. Sensor-based methods of gas source isolation have been utilized; however, such approaches have generally focused on applications for mobile robotics [198]–[200]. The work presented herein utilizes a series of stationary wireless IAQ sensors for gas source localization via classification algorithms. Experimental data was collected via wireless CO₂ sensors distributed throughout the IAQC (Figure 6.1). This preliminary research seeks to 1) demonstrate gas source classification via WSNs, 2) inform optimal sensor placement at the room-level, and 3) elucidate the duration of data necessary to characterize an indoor space. Ultimately, this study demonstrates the general feasibility for utilizing low-cost, low-power, wireless CO₂ sensors for high-resolution CO₂ sensing and serves to inform future studies on CO₂ sensor networks in the built environment.

6.4.1 Source Localization Approach

The proposed methodology is illustrated in Figure 6.4a. A two-stage approach is utilized which first seeks to identify a CO₂ disturbance at the room level and then, if a disturbance is detected, isolate the precise CO₂ source location within the room, via classification algorithms. Each stage of this approach provides valuable and progressively more precise information on the location of an indoor air pollutant. The first step involves identifying

a room-level CO₂ disturbance. For an enclosed space, this can be done by utilizing a CO₂ disturbance observer as illustrated in Figure 6.4b. This approach follows a mass-balance logic that monitors the inlet (supply air) and outlet (return air) of an enclosed space. This assumes that any changes measured between the inlet and outlet of the room are due to a disturbance that occurs within the enclosed space. Thus, a CO₂ disturbance can be estimated by subtracting the supply air duct (inlet) CO₂ concentration measurement from the return air duct (outlet) CO₂ concentration measurement.

Once a CO₂ disturbance has been determined to originate within a room, the second step involves further defining the exact internal source location. At the room-level, gas source isolation with high resolution can be particularly challenging when utilizing stationary sensors. This is especially so for small rooms with no gas constraining boundaries (e.g., walls, bookshelves, large furniture, etc). However, this problem can be reduced by defining zones within a room (e.g., separate into quadrants) in which a gas source could reside. In doing so, each region can be categorically separated and classification-type algorithms can be utilized to identify source locations (Figure 6.4c).

6.4.2 Experimental Procedure

To mimic an indoor environment, this work used the IAQC to collect experimental data. Wireless IAQ sensors (AWAIR Omni) were deployed in a grid-like pattern in the test chamber as shown in Figure 6.5. Sensors were placed in the supply duct (S1), the return duct (S11), and approximately 4 ft (1.2 m) above the floor on sensor trees throughout the room (S2-S10). For the purposes of gas source classification, the room was artificially separated into four quadrants, as labeled in Figure 6.5b. Thus, there were 5 potential CO₂ disturbance states for the room; namely, an ‘external’ source or an internal source in one of 4 quadrants in the room (Q1-Q4).

Experiments were performed using CO₂, which can be detected and measured by the installed IAQ sensors. To simulate gas emissions at different source locations, CO₂ gas was injected into the upstream supply duct (external source) and in the center of each of the four quadrants in the test chamber (Q1-Q4 source). For each trial CO₂ gas was injected

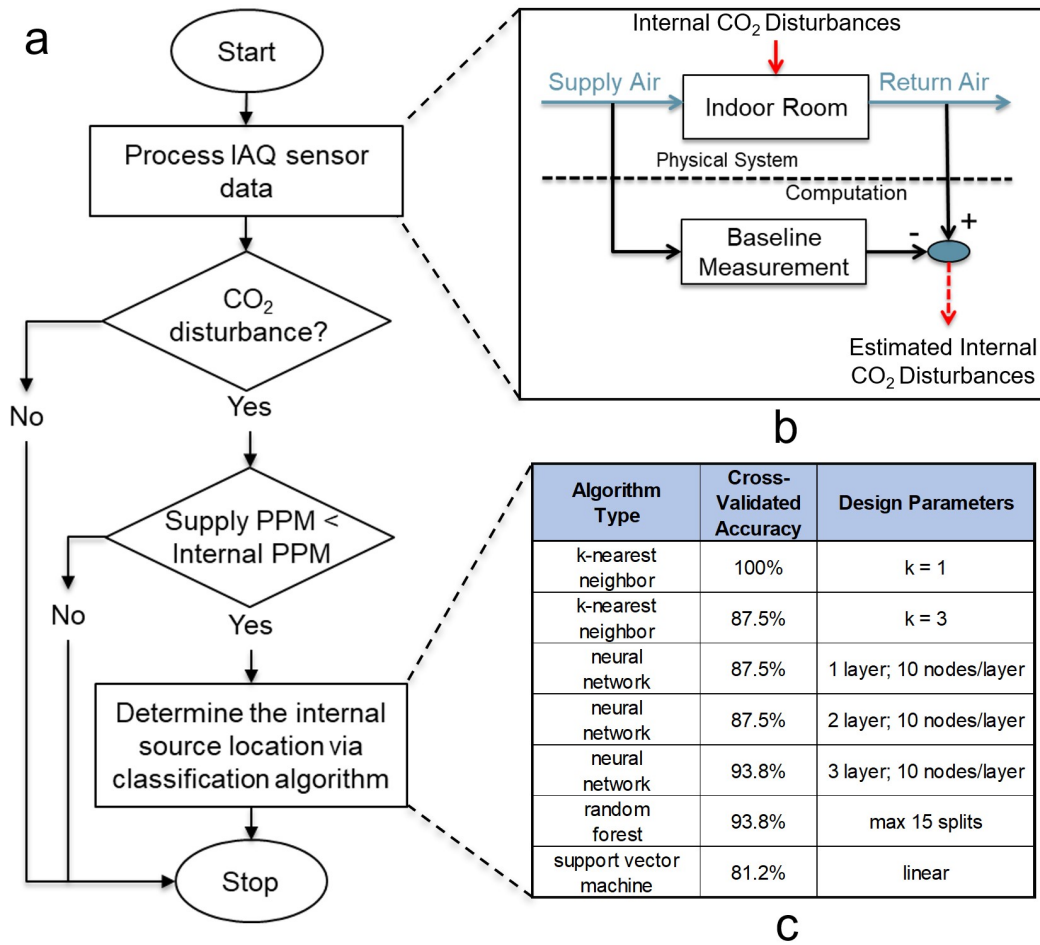


Figure 6.4. (a) A two-stage logical approach to gas source isolation. (b) A disturbance observer to estimate CO₂ disturbances in a closed room. (c) Classification algorithms to determine a gas source location within the enclosed space.

via a mass flow controller (MKS Instruments 1179C) for 1 hour at a rate of 350 ccm; which is approximately the CO₂ generation rate from human respiration [8]. Following each trial, the room was continuously ventilated with fresh outdoor air until a steady-state baseline was obtained (~ 420 ppm CO₂). Throughout the experiments, the supply and return fans maintained constant set points and circulated outdoor air at a rate of approximately 75 cfm ($2.1 \text{ m}^3 \text{ min}^{-1}$; ~ 2.2 ACH).

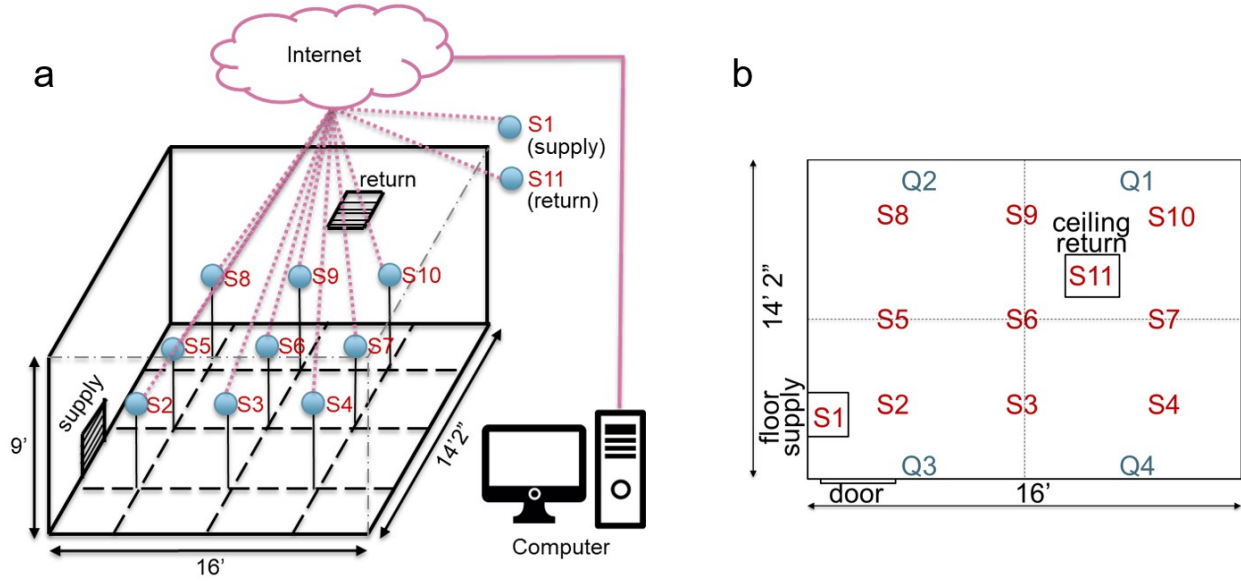


Figure 6.5. (a) Commercial IoT air quality sensors installed in the environmental test chamber for propagation modeling and source isolation experiments. (b) A top-down view of sensor placement within the environmental test chamber.

6.4.3 Event Window and Data Preparation

Implementation of a gas source localization algorithm requires real-time identification of a gas source release. Additionally, in order to develop classification models based on experimental data, the data set needs to be divided and labeled according to each gas source release location. Therefore, a window approach was utilized to both identify when a CO₂ release occurred as well as to bound and label the data for classification modeling purposes. To identify a sensor response to a gas source release, a 5 minute sliding window was utilized, which identified a release event as a 25 ppm rise above baseline CO₂ conditions. Once an

event was triggered, an event window was used for source localization. This event window began at the start of the 5 minute trigger. For initial studies reported herein, a 30 minute event window was utilized, and the length of this time window was explored, as reported in Section 6.4.5. Based on this window, features were extracted for each labeled event, such as each sensor’s mean CO₂ measurement, the rate of change in CO₂ concentration, and the order in which the sensors respond to CO₂.

6.4.4 Experimental Results

To start, it is helpful to understand each sensor’s time response to gas injected at each of the 5 source locations. Such data can be useful for both distinguishing (classifying) each of the different gas source locations and defining the minimum amount of time necessary to obtain actionable data from each sensor. Table 6.1 compares the average time response of each sensor to CO₂ injected at each potential source location. All of the recorded times are relative to the first sensor that responded to CO₂, where a response is defined as a 25 ppm rise above baseline conditions. Notably, the closest sensor to the gas source release was not always the first to respond (Figure 6.5). This is likely due to the forced air dynamics of the space, along with CO₂ being denser than air and accumulating near the floor. For nearly all of the sensors, the longest response times were to an external gas source. Sensor S1 (supply) was an obvious exception and responded first to an external source of CO₂, but did not respond to any of the internal gas source releases. The longest recorded response was more than 15 minutes for the return air duct sensor (S11) in response to an external gas source. Thus, some disturbance information was available to all of the sensors in the space within an approximately 15 minute time window. These data demonstrate the approximate length of time it takes a gas to disperse through a small room with forced ventilation at relatively low airflow rates. Thus, a larger room would likely increase the length of the response time and higher ventilation rates would likely decrease the length of the response time.

Further comparison can be made by considering a time series sample of the experimental data. Figure 6.6 depicts a time series representation of CO₂ being injected in the supply duct and in quadrant Q3 of the room. This illustration clearly shows how the supply side sensor

Table 6.1. The average time to respond to a CO₂ release event, relative to the first sensor that responded. The time response is defined as a 25 ppm rise above baseline conditions.

Sensor Number	External Source (sec)	Q1 Source (sec)	Q2 Source (sec)	Q3 Source (sec)	Q4 Source (sec)
S1	0 (first)	NA	NA	NA	NA
S2	600	267	405	220	390
S3	352	47	385	0 (first)	315
S4	520	350	315	130	0 (first)
S5	325	0 (first)	227	195	320
S6	425	205	155	265	400
S7	425	195	145	192	427
S8	667	55	0 (first)	370	470
S9	250	92	252	185	322
S10	602	415	97	272	490
S11	922	585	267	535	640

(S1) can be used as a point of comparison for distinguishing an internal source location (i.e. Q3 source) from an external source location. As shown in Figure 6.6, compared to all other sensors, a distinctly higher concentration is measured on the supply side sensor (S1) when gas was injected into the upstream supply duct (simulating an external gas source). This is not a particularly surprising result as an external gas source will likely be more concentrated in the supply duct and less concentrated after diffusing through a room. Whereas, for the representative example of an internal source location (Q3 source), the supply side sensor measured a significantly lower concentration than the rest of the room (~ 420 ppm CO₂). Thus, a gas source external to the room can easily be characterized by comparing the supply air duct measurement with any other sensor measurement internal to or exiting the room (i.e. return duct). So, as part of the two-stage approach to gas source isolation described herein (Figure 6.4a), once a CO₂ disturbance is detected, the gas source can be identified as internal if $S1 < S2:S11$.

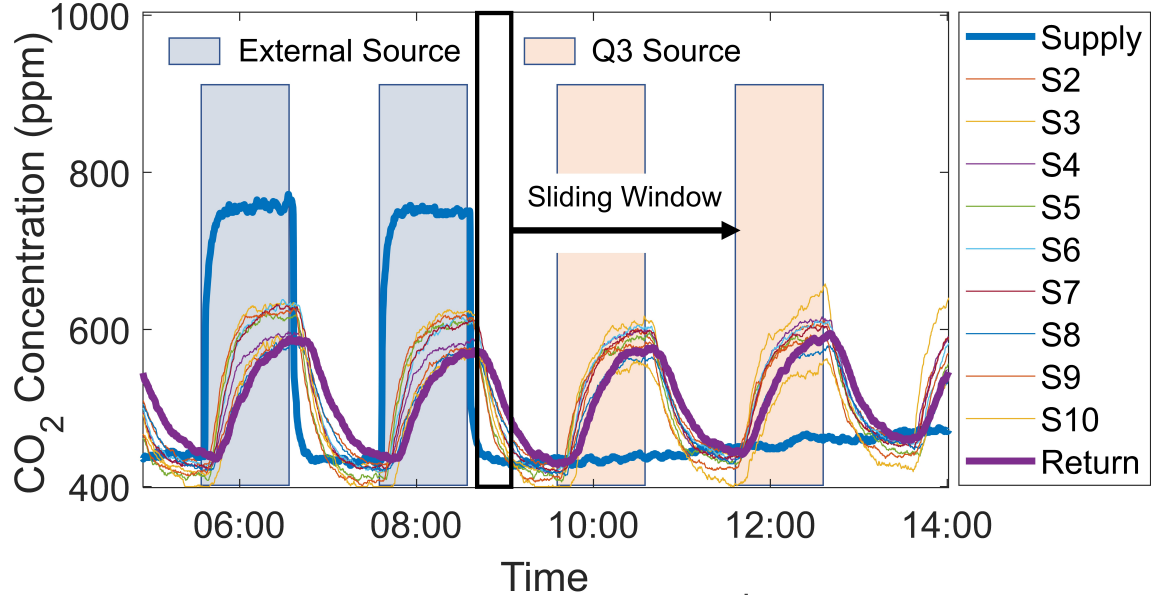


Figure 6.6. Time series representation of CO₂ injected into two different locations of the IAQC. As annotated in the figure, these pulses show CO₂ being released in the upstream supply duct (external source) and in quadrant Q3. A sliding window approach was utilized to identify a gas source release and to bound the data for feature extraction.

6.4.5 Classification Modeling

Utilizing the sliding window approach previously described, features were extracted and explored for a 30 minute window of each CO₂ source release. Among these extracted features, the mean CO₂ concentration recorded by sensors S4 and S8 provided a clear separation between the data classes. Notably, these two sensors are on opposite corners of the room (Figure 6.5) and are not in the quadrants that include the supply or return diffusers. Plotting these values in a 2-D feature space (Figure 6.7a), one can clearly see the separation between the source releases in each of the room quadrants.

Given the clear class separation provided by this highly-reduced feature space, basic classification models were developed and explored using just these two features. The cross-validated accuracy of select models are compared in Figure 6.4c. These models were assessed based on 4-fold cross validation between a total of 16 samples. So, 12 samples were used for training and the remaining 4 were used for validation in each fold. Among the tested model

types, a k-nearest neighbor model (kNN; $k=1$) performed particularly well. Thus, employing this model-type, the time dependency of the sliding window utilized for feature extraction was explored. As shown by the series of plots in Figure 6.7, decreasing the size of the window decreased the cross-validated accuracy of the classification model. A model based on a 15 minute time window retained a relatively low misclassification rate. However, when using a time window of 5 minutes or less, the model accuracy quickly diminished. These observations can be further corroborated by the time response data in Table 6.1, where the CO₂ gas is shown to propagate throughout the entire room within approximately 15 minutes.

6.4.6 Limitations

Although promising, these data and classification models were developed under a very specific set of experimental conditions. These experiments were performed with a single, non-moving point source of gas injection. In addition, data was collected for only one ventilation scenario which had a single supply and return diffuser in the room, in a single configuration (floor and ceiling, respectively). To be utilized in a ‘real-world’ application, a more rigorous study would need to be completed which considered different ventilation scenarios. As well, data would likely need to be collected in the specific space where the model would be deployed. Further, these data only represent room-temperature CO₂ gas, whereas a warmer and less-dense gas may disperse differently in a room. Finally, given the expense of collecting experimental data, these models were constructed on a relatively lean data set (4 samples per class). So, a more robust model might be developed based on classification of a larger data set. However, despite these limitations, the described efforts demonstrate the basic feasibility and potential for utilizing a sensor network and black box modeling approach to gas source isolation in an enclosed space.

6.4.7 Discussion

A framework was presented for utilizing low-cost, wireless gas sensors for high-resolution CO₂ monitoring in buildings. The use of wireless sensor networks for CO₂ source localization was demonstrated based on experimental data collected in a well-controlled indoor

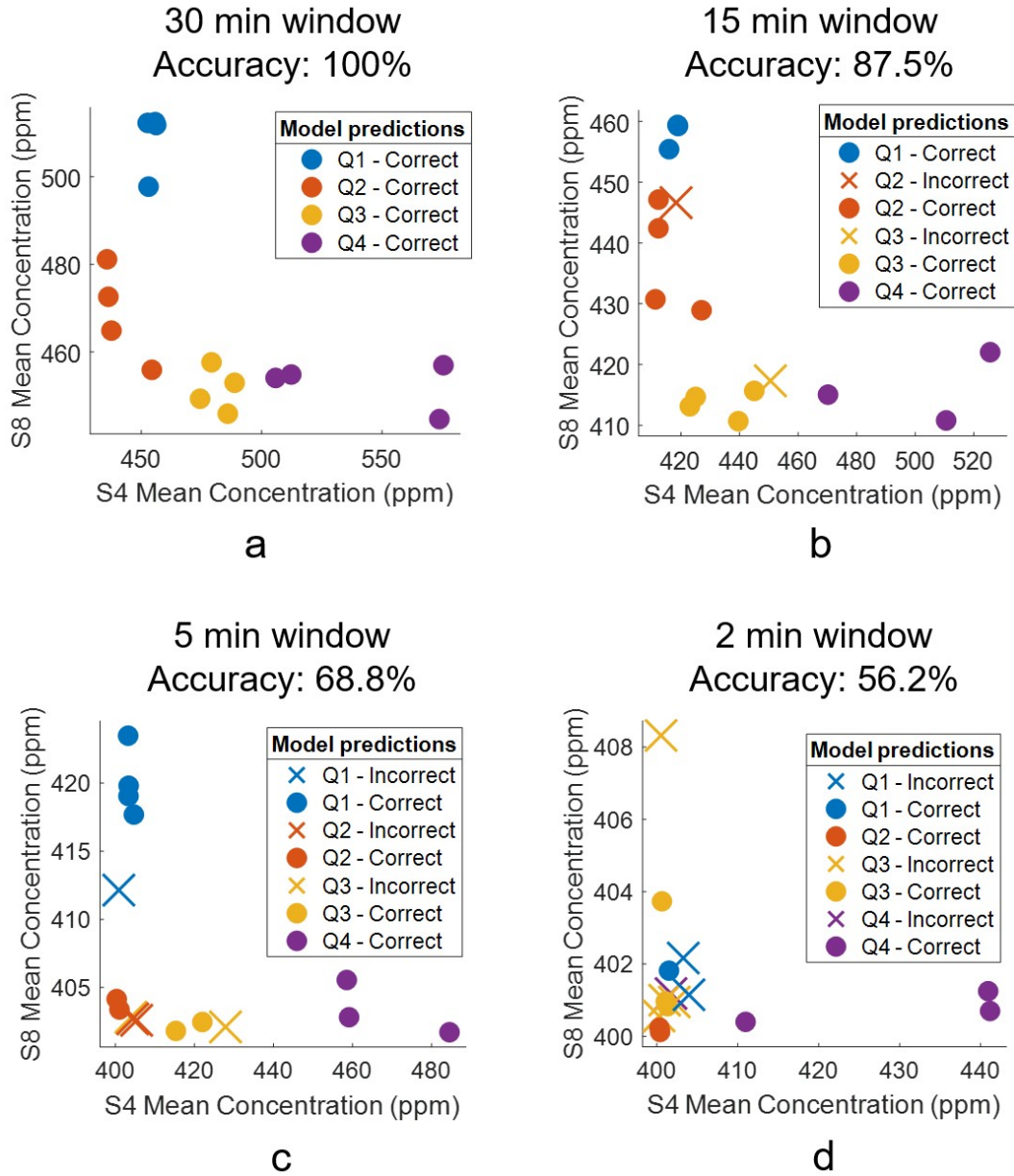


Figure 6.7. Feature space representing the mean CO₂ concentration at sensors S4 and S8 in a (a) 30-min, (b) 15-min, (c) 5-min, and (d) 2-min time window. As the length of the time window for feature extraction decreases, the cross-validated model accuracy diminishes while utilizing a kNN (k=1) classification approach.

environmental test chamber. In these experiments, the closest sensor to the CO₂ generation source was not necessarily the first to respond, nor the sensor with the largest response. Additionally, just two sensors provided enough information to locate a CO₂ emission source, that was at approximately the rate of human respiration, within 30 minutes. Thus, two sensors (one in each specified location) are necessary for characterizing this particular air space for occupant localization. Though limited in scope, these results are particularly promising as they demonstrate the fundamental feasibility of occupant localization via wireless CO₂ sensor networks.

7. SUMMARY AND CONCLUSIONS

The work presented herein demonstrated a series of novel CO₂ sensors capable of indoor CO₂ monitoring. Each of these sensors has the potential to be manufactured at a low cost and operate at relatively low power, making them a potentially attractive alternative to CO₂ sensors that are currently commercially available. Further, this work presented a set of methodologies for CO₂ sensor evaluation in both benchtop and full-scale environments. These methods may be used to inform CO₂ sensor performance and some of the nuances anticipated in building applications.

Chapter 2 presented a polymer composite-based chemiresistive CO₂ sensor that leveraged branched poly(ethylenimine) (PEI) and poly(ethylene glycol) (PEG) as the CO₂ absorbing layer. This polymer blend was incorporated with single wall carbon nanotubes (CNT), which served as the charge carriers. Prototype sensors were assessed in a bench-top environmental test chamber which varied temperatures (22-26 °C), relative humidity levels (20-80%), CO₂ concentrations (400-20,000 ppm), as well as other gas constituents to simulate typical and extreme indoor conditions. The results indicated that the proposed system could ultimately serve as a low-power alternative to current commercially available technologies for indoor CO₂ monitoring. The potential of such a low-power sensor is particularly promising when considering wireless deployment of sensors, which are inherently power constrained. In addition, the solid-state architecture of this device may provide advantages for long-term reliability.

Chapters 3-5 presented MEMS-based sensors utilizing similar resonant mass sensing platforms, but differed in the functional materials and scope. The sensors in Chapter 3 were functionalized with a polymerized ionic liquid via an inkjet printing technique. An imidazolium cation functionality with a hexafluorophosphate anion chemistry (poly(1-methyl-3-(4-vinylbenzyl)-1H-imidazol-3-ium) hexafluorophosphate [PMVBI-PF₆]) was added to a polystyrene backbone motif, as this combination has previously shown significant CO₂ interactions when utilized as a sorbent material for the capture of carbon dioxide from the atmosphere. Assessments were performed in a bench-top environmental test chamber, similar to that used for the chemiresistive sensor in Chapter 2. The oscillation frequency was

measured using a custom digital logic-based frequency counter circuit implemented in a field-programmable gate array (FPGA). The results show that the proposed approach, with additional development, could serve as an alternative to current commercially available CO₂ sensing technologies.

Chapter 4 presented a resonant mass sensor treated with a solution-processable polymer blend of poly(ethylene oxide) (PEO) and poly(ethyleneimine) (PEI) for the selective and significantly enhanced detection of CO₂, relative to the PIL in Chapter 3. When semi-crystalline PEO was blended with PEI, a physical separation of interchain amine interactions occurred. In turn, this separation facilitated diffusion of CO₂ into the material and more interactions between intrachain amines and CO₂ gas. Moreover, the hydrophilic properties of PEO prompted water uptake into the polymer matrix which allowed for reversible acid-base reactions between the CO₂ and PEI amines to occur which facilitated mass uptake on the mass resonator. This macromolecular blend led to highly-selective and highly-responsive sensors.

Similarly, Chapter 5 presented a study on the temperature-dependent kinetics of the PEI-PEO functionalized resonators. This research measured performance across an extended temperature range (relative to Chapter 4) to better understand the capabilities and boundaries of the sensing system. A Langmuir model was fit to the data, from which adsorption rate constants and basic thermodynamic parameters were calculated to describe the sorption of CO₂ on the sensor. Throughout a range of temperatures relevant to indoor CO₂ monitoring, these polymer materials adsorbed less and desorbed more CO₂ with increasing temperature. This was due, in part, to the melting of the polymer materials. Specifically, in a 3:1 PEO:PEI polymer blend, such melting decreases the crystalline features of PEO in the PEI matrix and ultimately causes a loss of porosity in the polymer films. Further, the 3:1 PEO:PEI blended material adsorbed more CO₂, at a faster rate, than PEI alone due to the crystalline features of PEO disrupting strong interchain and intrachain amine interactions which limit the interaction of CO₂ gas into the polymer matrix. Thus, the 3:1 PEO:PEI blended polymer system provides higher sensitivity and faster response times for indoor sensing applications over PEI alone and will perform well until the PEO moiety melts.

Finally, Chapter 6 discussed full-scale implementation of CO₂ sensors in the built environment and suggested pathways for extending the research presented herein. This included discussion on the placement of sensors in buildings and presentation of preliminary data on prototype resonant mass sensors in a room-sized environmental test chamber. Lastly, a methodology was presented, along with experimental data, that demonstrated the basic feasibility of using CO₂ sensor networks for occupant localization in the built environment.

Overall, the resonant mass sensors (Chapters 3-5) were found to be more sensitive than their chemiresistive counterpart (Chapter 2). However, this was achieved at the cost of slightly higher power consumption and reduced signal clarity at high humidity levels. Nevertheless, the power consumption and footprint of both of these sensors is much smaller than most commercial sensors currently available. Such metrics make wireless and ubiquitous CO₂ sensing in buildings relevant, which presents new opportunities in smart building controls. With further development, these sensors may serve not only as an alternative to currently available commercial CO₂ sensors, but provide new data nodes throughout buildings that were previously not economically viable. In such a case, Chapter 6 demonstrates the basic feasibility and potential for utilizing a sensor network and black box modeling approach for gas source isolation in an enclosed space. Therefore, with further development, these sensors may also be a promising path toward cost-effective and non-discriminatory occupant localization via wireless sensor networks.

REFERENCES

- [1] EIA, “Frequently asked questions on buildings in the United States,” *United States Energy Information Administration*, 2010.
- [2] EPA, “Report to Congress on indoor air quality: Volume 2. EPA/400/1-89/001C,” *United States Environmental Protection Agency*, 2010.
- [3] D. Calí, P. Matthes, K. Huchtemann, R. Streblow, and D. Müller, “CO₂ based occupancy detection algorithm: Experimental analysis and validation for office and residential buildings,” *Building and Environment*, vol. 86, pp. 39–49, 2015.
- [4] N. Mahyuddin and H. Awbi, “A review of CO₂ measurement procedures in ventilation research,” *International Journal of Ventilation*, vol. 10, pp. 353–370, 2012.
- [5] K. Weekly, N. Bekiaris-Liberis, M. Jin, and A. Bayen, “Modeling and estimation of the humans’ effect on the CO₂ dynamics inside a conference room,” *IEEE Transactions on Control Systems Technology*, vol. 23, pp. 1770–1781, 2015.
- [6] A. Szczurek, M. Maciejewska, and T. Pietrucha, “Occupancy determination based on time series of CO₂ concentration, temperature and relative humidity,” *Energy and Buildings*, vol. 147, pp. 142–154, 2017.
- [7] F. Wang, Q. Feng, Z. Chen, *et al.*, “Predictive control of indoor environment using occupant number detected by video data and CO₂ concentration,” *Energy and Buildings*, vol. 145, pp. 155–162, 2017.
- [8] ASHRAE, “ASHRAE/ANSI standard 62.1-2019 ventilation for acceptable indoor air quality,” 2010.
- [9] A. Persily and J. Forfain, “Analysis of ventilation data from the U.S. Environmental Protection Agency building assessment survey and evaluation (BASE) study,” United States Environmental Protection Agency, Tech. Rep., 2004.
- [10] S. Shriram, K. Ramamurthy, and S. Ramakrishnan, “Effect of occupant-induced indoor CO₂ concentration and bioeffluents on human physiology using a spirometric test,” *Building and Environment*, vol. 149, pp. 58–67, 2019.
- [11] K. Azuma, N. Kagi, U. Yanagi, and H. Osawa, “Effects of low-level inhalation exposure to carbon dioxide in indoor environments: A short review on human health and psychomotor performance,” *Environment International*, vol. 121, pp. 51–56, 2018.

- [12] U. Satish, M. J. Mendell, K. Shekhar, *et al.*, “Is CO₂ an indoor pollutant? Direct effects of low-to-moderate CO₂ concentrations on human decision-making performance,” *Environmental Health Perspectives*, vol. 120, pp. 1671–1677, 2012.
- [13] B. Du, M. C. Tandoc, M. L. Mack, and J. A. Siegel, “Indoor CO₂ concentrations and cognitive function: A critical review,” *Indoor Air*, vol. 30, pp. 1067–1082, 2020.
- [14] B. Gunay and W. Shen, “Connected and distributed sensing in buildings: Improving operation and maintenance,” *IEEE Systems, Man, and Cybernetics Magazine*, vol. 3, pp. 27–34, Oct. 2017.
- [15] Y. You, C. Niu, J. Zhou, *et al.*, “Measurement of air exchange rates in different indoor environments using continuous CO₂ sensors,” *Journal of Environmental Sciences*, vol. 24, pp. 657–664, 2012.
- [16] L. C. Ng and J. Wen, “Estimating building airflow using CO₂ measurements from a distributed sensor network,” *HVAC&R Research*, vol. 17, pp. 344–365, 2011.
- [17] L. M. Candanedo and V. Feldheim, “Accurate occupancy detection of an office room from light, temperature, humidity and CO₂ measurements using statistical learning models,” *Energy and Buildings*, vol. 112, pp. 28–39, 2016.
- [18] T. Ekwevugbe, N. Brown, V. Pakka, and D. Fan, “Real-time building occupancy sensing using neural-network based sensor network,” in *2013 7th IEEE International Conference on Digital Ecosystems and Technologies (DEST)*, Jul. 2013, pp. 114–119.
- [19] M. Jin, N. Bekiaris-Liberis, K. Weekly, C. J. Spanos, and A. M. Bayen, “Occupancy detection via environmental sensing,” *IEEE Transactions on Automation Science and Engineering*, vol. 15, pp. 443–455, 2018.
- [20] N. Mizuno, T. Yoshioka, K. Kato, and M. Iwamoto, “CO₂-sensing characteristics of SnO₂ element modified by La₂O₃,” *Sensors and Actuators B: Chemical*, vol. 13, pp. 473–475, 1993.
- [21] A. Chapelle, F. Oudrhiri-Hassani, L. Presmanes, A. Barnabé, and P. Tailhades, “CO₂ sensing properties of semiconducting copper oxide and spinel ferrite nanocomposite thin film,” *Applied Surface Science*, vol. 256, pp. 4715–4519, 2010.
- [22] F. Juang, “Ag additive and nanorod structure enhanced gas sensing properties of metal oxide-based CO₂ sensor,” *IEEE Sensors Journal*, vol. 19, pp. 4381–4385, 2019.
- [23] F.-R. Juang and B.-Y. Chen, “Effect of adding ZHS microcubes on ZnO nanorods for CO₂ gas sensing applications,” *Solid-State Electronics*, vol. 164, p. 107 711, 2020.

- [24] K.-C. Hsu, T.-H. Fang, Y.-J. Hsiao, and C.-A. Chan, “Highly response CO₂ gas sensor based on Au-La₂O₃ doped SnO₂ nanofibers,” *Materials Letters*, vol. 261, p. 127144, 2020.
- [25] D. D. Trung, L. D. Toan, H. S. Hong, T. D. Lam, T. Trung, and N. Van Hieu, “Selective detection of carbon dioxide using LaOCl-functionalized SnO₂ nanowires for air-quality monitoring,” *Talanta*, vol. 88, pp. 152–159, 2012.
- [26] A. Chapelle, I. El Younsi, S. Vitale, *et al.*, “Improved semiconducting CuO/CuFe₂O₄ nanostructured thin films for CO₂ gas sensing,” *Sensors and Actuators B: Chemical*, vol. 204, pp. 407–413, 2014.
- [27] G. F. Fine, L. M. Cavanagh, A. Afonja, and R. Binions, “Metal oxide semi-conductor gas sensors in environmental monitoring,” *Sensors*, vol. 10, pp. 5469–5502, 2010.
- [28] D. F. Swinehart, “The Beer-Lambert law,” *Journal of Chemical Education*, vol. 39, pp. 333–335, 1962.
- [29] M. Marinov, G. Nikolov, E. Gieva, and B. Ganey, “Improvement of NDIR carbon dioxide sensor accuracy,” in *2015 38th International Spring Seminar on Electronics Technology (ISSE)*, 2015, pp. 466–471.
- [30] J. Park, H. Cho, and S. Yi, “NDIR CO₂ gas sensor with improved temperature compensation,” *Procedia Engineering*, vol. 5, pp. 303–306, 2010.
- [31] T. Yasuda, S. Yonemura, and A. Tani, “Comparison of the characteristics of small commercial NDIR CO₂ sensor models and development of a portable CO₂ measurement device,” *Sensors*, vol. 12, pp. 3641–3655, 2012.
- [32] J. Peterson, J. Kristensen, H. Elarga, and R. Anderson, “Accuracy and air temperature dependency of commercial low-cost NDIR CO₂ sensors: An experimental investigation,” in *4th International Conference on Building Energy, Environment, Melbourne*, 2018, pp. 203–207.
- [33] C. R. Martin, N. Zeng, A. Karion, *et al.*, “Evaluation and environmental correction of ambient CO₂ measurements from a low-cost NDIR sensor,” *Atmospheric Measurement Techniques*, vol. 10, pp. 2383–2395, 2017.
- [34] T. Labeodan, W. Zeiler, G. Boxem, and Y. Zhao, “Occupancy measurement in commercial office buildings for demand-driven control applications—A survey and detection system evaluation,” *Energy and Buildings*, vol. 93, pp. 303–314, 2015.
- [35] S. J. Emmerich and A. K. Persily, “State-of-the-art review of CO₂ demand controlled ventilation technology and application, NISTIR 6729,” *National Institute of Standards and Technology*, 2001.

- [36] S. Yi, Y. Park, S. Han, N. Min, E. Kim, and T. Ahn, “Novel NDIR CO₂ sensor for indoor air quality monitoring,” in *The 13th International Conference on Solid-State Sensors, Actuators and Microsystems, 2005. Digest of Technical Papers. TRANSDUCERS '05.*, vol. 2, 2005, pp. 1211–1214.
- [37] J. Kwon, G. Ahn, G. Kim, J. C. Kim, and H. Kim, “A study on NDIR-based CO₂ sensor to apply remote air quality monitoring system,” in *2009 ICCAS-SICE*, 2009, pp. 1683–1687.
- [38] L. Schibuola, M. Scarpa, and C. Tambani, “CO₂ based ventilation control in energy retrofit: An experimental assessment,” *Energy*, vol. 143, pp. 606–614, 2018.
- [39] M. O. Ng, M. Qu, P. Zheng, Z. Li, and Y. Hang, “CO₂-based demand controlled ventilation under new ASHRAE standard 62.1-2010: A case study for a gymnasium of an elementary school at West Lafayette, Indiana,” *Energy and Buildings*, vol. 43, pp. 3216–3225, 2011.
- [40] S. Shrestha, “Performance evaluation of carbon-dioxide sensors used in building HVAC applications,” Ph.D. dissertation, Iowa State University, Ames, IA, 2009.
- [41] W. Fisk, D. Sullivan, D. Faulkner, and E. Eliseeva, “CO₂ monitoring for demand controlled ventilation in commercial buildings,” *Lawrence Berkeley National Laboratory*, no. LBNL-3278E, 2010.
- [42] A. Mylonas, O. B. Kazanci, R. K. Anderson, and B. W. Olesen, “Capabilities and limitations of wireless CO₂, temperature and relative humidity sensors,” *Building and Environment*, vol. 154, pp. 362–374, 2019.
- [43] S. K. Pandey and K.-H. Kim, “The relative performance of NDIR-based sensors in the near real-time analysis of CO₂ in air,” *Sensors*, vol. 7, pp. 1683–1696, 2007.
- [44] L. Scholz, A. O. Perez, S. Knobelspies, J. Wöllenstein, and S. Palzer, “MID-IR LED-based, photoacoustic CO₂ sensor,” *Procedia Engineering*, vol. 120, pp. 1233–1236, 2015.
- [45] L. Scholz, A. O. Perez, B. Bierer, P. Eaksen, J. Wöllenstein, and S. Palzer, “Carbon dioxide sensor for mobile devices: A novel approach for low-power consuming, highly sensitive NDIR sensors,” in *2016 IEEE SENSORS*, 2016, pp. 1–3.
- [46] J. Hodgkinson, R. Smith, W. Ho, J. Saffell, and R. Tatam, “Non-dispersive infra-red (NDIR) measurement of carbon dioxide at 4.2 μm in a compact and optically efficient sensor,” *Sensors and Actuators B: Chemical*, vol. 186, pp. 580–588, 2013.
- [47] I. Fratoddi, I. Venditti, C. Cametti, and M. V. Russo, “Chemiresistive polyaniline-based gas sensors: A mini review,” *Sensors and Actuators B: Chemical*, vol. 220, pp. 534–548, 2015.

- [48] S. Waghuley, S. Yenorkar, S. Yawale, and S. Yawale, "Application of chemically synthesized conducting polymer-polypyrrole as a carbon dioxide gas sensor," *Sensors and Actuators B: Chemical*, vol. 128, pp. 366–373, 2008.
- [49] S. Bag and K. Pal, "A PCB based chemiresistive carbon dioxide sensor operating at room temperature under different relative humidity," *IEEE Transactions on Nanotechnology*, vol. 18, pp. 1119–1128, 2019.
- [50] W. Chuang, C. Wu, Y. Su, *et al.*, "A low-power PEDOT: PSS/EB-PANI for CO₂ sensing material integrated with a self-powered sensing platform," *IEEE Sensors Journal*, vol. 20, pp. 55–61, 2020.
- [51] Y. G. Ko, S. S. Shin, and U. S. Choi, "Primary, secondary, and tertiary amines for CO₂ capture: Designing for mesoporous CO₂ adsorbents," *Journal of Colloid and Interface Science*, vol. 361, pp. 594–602, 2011.
- [52] J. Tang, H. Tang, W. Sun, M. Radosz, and Y. Shen, "Poly(ionic liquid)s as new materials for CO₂ absorption," *Journal of Polymer Science Part A: Polymer Chemistry*, vol. 43, pp. 5477–5489, 2005.
- [53] J. Tang, Y. Shen, M. Radosz, and W. Sun, "Isothermal carbon dioxide sorption in poly(ionic liquid)s," *Industrial & Engineering Chemistry Research*, vol. 48, pp. 9113–9118, 2009.
- [54] J. Tang, W. Sun, H. Tang, M. Radosz, and Y. Shen, "Enhanced CO₂ absorption of poly(ionic liquid)s," *Macromolecules*, vol. 38, pp. 2037–2039, 2005.
- [55] J. E. Bara, S. Lessmann, C. J. Gabriel, E. S. Hatakeyama, R. D. Noble, and D. L. Gin, "Synthesis and performance of polymerizable room-temperature ionic liquids as gas separation membranes," *Industrial & Engineering Chemistry Research*, vol. 46, pp. 5397–5404, 2007.
- [56] S. Supasitmongkol and P. Styring, "High CO₂ solubility in ionic liquids and a tetraalkylammonium-based poly(ionic liquid)," *Energy environmental science*, vol. 3, pp. 1961–1972, 2010.
- [57] A. Blasig, J. Tang, X. Hu, Y. Shen, and M. Radosz, "Magnetic suspension balance study of carbon dioxide solubility in ammonium-based polymerized ionic liquids: Poly(p-vinylbenzyltrimethyl ammonium tetrafluoroborate) and poly([2-(methacryloyloxy)ethyl] trimethyl ammonium tetrafluoroborate)," *Fluid Phase Equilibria*, vol. 256, pp. 75–80, 2007.
- [58] J. Zhang, D. Xu, J. Guo, *et al.*, "CO₂ responsive imidazolium-type poly(ionic liquid) gels," *Macromolecular Rapid Communications*, vol. 37, pp. 1194–1199, 2016.

- [59] L. Zhang, Y. Chen, M. Rahimabady, *et al.*, “P(VDF-HFP) polymer as sensing material for capacitive carbon dioxide sensors,” *IEEE Sensors*, vol. 17, pp. 4349–4356, 2017.
- [60] C. Willa, J. Yuan, M. Niederberger, and D. Koziej, “When nanoparticles meet poly(ionic liquid)s: Chemoresistive CO₂ sensing at room temperature,” *Advanced Functional Materials*, vol. 25, pp. 2537–2542, 2015.
- [61] Y. Li, G. Li, X. Wang, *et al.*, “Poly(ionic liquid)-wrapped single-walled carbon nanotubes for sub-ppb detection of CO₂,” *Chemical Communications*, vol. 48, pp. 8222–8224, 2012.
- [62] W. Zhang, H. Liu, C. Sun, T. Drage, and C. Snape, “Capturing CO₂ from ambient air using a polyethyleneimine-silica adsorbent in fluidized beds,” *Chemical Engineering Science*, vol. 116, pp. 306–316, 2014.
- [63] A. Heydari-Gorji and A. Sayari, “CO₂ capture on polyethylenimine-impregnated hydrophobic mesoporous silica: Experimental and kinetic modeling,” *Chemical Engineering*, vol. 173, pp. 72–79, 2011.
- [64] J. Wang, H. Chen, H. Zhou, *et al.*, “Carbon dioxide capture using polyethylenimine-loaded mesoporous carbons,” *Chemical Engineering*, vol. 25, pp. 124–132, 2013.
- [65] K. Li, J. Jiang, F. Yan, S. Tian, and X. Chen, “The influence of polyethylenimine type and molecular weight on the CO₂ capture performance of PEI-nano silica adsorbents,” *Applied Energy*, vol. 136, pp. 750–755, 2014.
- [66] W. Choi, K. Min, C. Kim, *et al.*, “Epoxide-functionalization of polyethylenimine for synthesis of stable carbon dioxide adsorbent in temperature swing adsorption,” *Nature Communications*, vol. 7, p. 12 640, 2016.
- [67] N. Kiga, Y. Takei, A. Inaba, H. Takahashi, K. Matsumoto, and I. Shimoyama, “CNT-FET gas sensor using a functionalized ionic liquid as gate,” in *2012 IEEE 25th International Conference on Micro Electro Mechanical Systems (MEMS)*, 2012, pp. 796–799.
- [68] W. Ma, R. Wang, Q. Rong, *et al.*, “CO₂ gas sensing using optical fiber Fabry–Perot interferometer based on polyethylenimine /poly(vinyl alcohol) coating,” *IEEE Photonics Journal*, vol. 9, pp. 1–8, 2017.
- [69] Y. Chang, D. Hasan, B. Dong, *et al.*, “Surface-enhanced infrared absorption-based CO₂ sensor using photonic crystal slab,” in *2019 IEEE 32nd International Conference on Micro Electro Mechanical Systems (MEMS)*, 2019, pp. 141–144.
- [70] A. Star, T.-R. Han, V. Joshi, J.-C. P. Gabriel, and G. Grüner, “Nanoelectronic carbon dioxide sensors,” *Advanced Materials*, vol. 16, pp. 2049–2052, 2004.

- [71] M. Son, Y. Pak, S.-S. Chee, *et al.*, “Charge transfer in graphene/polymer interfaces for CO₂ detection,” *Nano Research*, vol. 11, pp. 3529–3536, 2018.
- [72] Z. A. Siefker, X. Zhao, N. Bajaj, *et al.*, “A carbon nanotube-functional polymer composite film for low-power indoor CO₂ monitoring,” *IEEE Sensors Journal*, pp. 1–1, 2021.
- [73] L. Morawska, J. W. Tang, W. Bahnfleth, *et al.*, “How can airborne transmission of COVID-19 indoors be minimised?” *Environment International*, vol. 142, p. 105832, 2020.
- [74] J. Nwanaji-Enwerem, J. Allen, and P. Beamer, “Another invisible enemy indoors: COVID-19, human health, the home, and United States indoor air policy,” *Journal of Exposure Science Environmental Epidemiology*, vol. 30, pp. 773–775, 2020.
- [75] O. Brittain, H. Wood, and P. Kumar, “Prioritising indoor air quality in building design can mitigate future airborne viral outbreaks,” *Cities & Health*, pp. 1–4, 2020.
- [76] I. Pirhonen, A. Nevalainen, T. Husman, and J. Pekkanen, “Home dampness, moulds and their influence on respiratory infections and symptoms in adults in Finland,” *European Respiratory Journal*, vol. 9, pp. 2618–2622, 1996.
- [77] M. Andersson, M. Nikulin, U. Kõljalg, *et al.*, “Bacteria, molds, and toxins in water-damaged building materials,” *Applied and Environmental Microbiology*, vol. 63, pp. 387–393, 1997.
- [78] B. Huang, C. Lei, C. Wei, and G. Zeng, “Chlorinated volatile organic compounds (Cl-VOCs) in environment — Sources, potential human health impacts, and current remediation technologies,” *Environment International*, vol. 71, pp. 118–138, 2014.
- [79] Y. Huang, S. S. H. Ho, K. F. Ho, S. C. Lee, J. Z. Yu, and P. K. Louie, “Characteristics and health impacts of VOCs and carbonyls associated with residential cooking activities in Hong Kong,” *Journal of Hazardous Materials*, vol. 186, pp. 344–351, 2011.
- [80] O. Seppänen, W. Fisk, and M. Mendell, “Association of ventilation rates and CO₂ concentrations with health and other responses in commercial and institutional buildings,” *Indoor Air*, vol. 9, pp. 226–252, 1999.
- [81] X. Zhang, P. Wargocki, Z. Lian, and C. Thyregod, “Effects of exposure to carbon dioxide and bioeffluents on perceived air quality, self-assessed acute health symptoms, and cognitive performance,” *Indoor Air*, vol. 27, pp. 47–64, 2017.
- [82] D.-H. Tsai, J.-S. Lin, and C.-C. Chan, “Office workers’ sick building syndrome and indoor carbon dioxide concentrations,” *Journal of Occupational and Environmental Hygiene*, vol. 9, pp. 345–351, 2012.

- [83] P. Wargocki, D. Wyon, Y. Baik, G. Clausen, and P. Fanger, “Perceived air quality, sick building syndrome (SBS) symptoms and productivity in an office with two different pollution loads,” *Indoor Air*, vol. 9, pp. 165–179, 1999.
- [84] D. Wyon, “The effects of indoor air quality on performance and productivity,” *Indoor Air*, vol. 7, pp. 92–101, 2004.
- [85] U. Haverinen-Shaughnessy, R. J. Shaughnessy, E. C. Cole, O. Toyinbo, and D. J. Moschandreas, “An assessment of indoor environmental quality in schools and its association with health and performance,” *Building and Environment*, vol. 93, pp. 35–40, 2015.
- [86] J. Russo, W. Ray II, and M. Litz, “Low light illumination study on commercially available homojunction photovoltaic cells,” *Applied Energy*, vol. 191, pp. 10–21, 2017.
- [87] F. Shaikh and S. Zeadally, “Energy harvesting in wireless sensor networks: A comprehensive review,” *Renewable and Sustainable Energy Reviews*, vol. 55, pp. 1041–1054, 2016.
- [88] A. Zribi, A. Knobloch, and R. Rao, “CO₂ detection using carbon nanotube networks and micromachined resonant transducers,” *Applied Physics Letters*, vol. 86, p. 203 112, 2005.
- [89] Z. A. Siefker, A. K. Murray, X. Zhao, *et al.*, “A resonant CO₂ sensor functionalized with a polymerized ionic liquid,” in *2019 IEEE SENSORS*, 2019, pp. 1–4.
- [90] M. Eberl, F. Jost, S. Kolb, *et al.*, “Miniaturized photoacoustic CO₂ gas sensors - a new approach for the automotive sector,” in *AmE 2019 - Automotive Meets Electronics; 10th GMM-Symposium*, 2019, pp. 1–5.
- [91] S. Mirabella, I. P. Oliveri, F. Ruffino, G. Maccarrone, and S. Di Bella, “Low-cost chemiresistive sensor for volatile amines based on a 2D network of a zinc(II) Schiff-base complex,” *Applied Physics Letters*, vol. 109, p. 143 108, 2016.
- [92] Z. D. O’Neill, Y. Li, H. C. Cheng, X. Zhou, and S. T. Taylor, “Energy savings and ventilation performance from CO₂-based demand controlled ventilation: Simulation results from ASHRAE RP-1747 (ASHRAE RP-1747),” *Science and Technology for the Built Environment*, vol. 26, pp. 257–281, 2020.
- [93] S. Masa, E. Hontañón, J. P. Santos, I. Sayago, and J. Lozano, “Chemiresistive sensors based on electrospun tin oxide nanofibers for detecting NO₂ at the sub-0.1 ppm level,” in *2019 5th Experiment International Conference*, 2019, pp. 310–314.
- [94] N. Marchand, T. Walewyns, D. Lahem, M. Debligny, and L. A. Francis, “Ultra-low-power chemiresistive microsensor array in a back-end CMOS process towards selective volatile compounds detection and IoT applications,” in *2017 ISOCs/IEEE International Symposium on Olfaction and Electronic Nose*, 2017, pp. 1–3.

- [95] S. Srinives, T. Sarkar, R. Hernandez, and A. Mulchandani, "A miniature chemiresistor sensor for carbon dioxide," *Analytica Chimica Acta*, vol. 874, pp. 54–58, 2015.
- [96] X. Li, Y. Jung, K. Sakimoto, T.-H. Goh, M. A. Reed, and A. D. Taylor, "Improved efficiency of smooth and aligned single walled carbon nanotube/silicon hybrid solar cells," *Energy & Environmental Science*, vol. 6, pp. 879–887, 2013.
- [97] T.-V. Dinh, I.-Y. Choi, Y.-S. Son, and J.-C. Kim, "A review on non-dispersive infrared gas sensors: Improvement of sensor detection limit and interference correction," *Sensors and Actuators B: Chemical*, vol. 231, pp. 529–538, 2016.
- [98] ASHRAE, "ASHRAE/ANSI standard 55-2010 thermal environmental conditions for human occupancy," 2020.
- [99] M. Al-marri, M. Khader, M. Tawfik, G. Qi, and E. Giannelis, "CO₂ sorption kinetics of scaled-up polyethylenimine-functionalized mesoporous silica sorbent," *Langmuir*, vol. 31, pp. 3569–3576, 2015.
- [100] M. G. Apte, "A review of demand controlled ventilation," in *Proceedings of Healthy Buildings 2006*, pp. 371–376.
- [101] C. Weisel, S. Alimokhtari, and P. Sanders, "Indoor air VOC concentrations in suburban and rural New Jersey," *Environmental Science Technology*, vol. 42, pp. 8231–8238, 2008.
- [102] A. Raysoni, T. Stock, J. Sarnat, *et al.*, "Evaluation of VOC concentrations in indoor and outdoor microenvironments at near-road schools," *Environmental Pollution*, vol. 231, pp. 681–693, 2017.
- [103] L. Al-Awadi, "Assessment of indoor levels of volatile organic compounds and carbon dioxide in schools in Kuwait," *Air Waste Management Association*, vol. 68, pp. 54–72, 2018.
- [104] N. Bajaj, A. B. Sabater, G. T.-C. Chiu, and J. F. Rhoads, "Design and implementation of a tunable, Duffing-like electronic resonator via nonlinear feedback," *Journal of Microelectromechanical Systems*, vol. 25, pp. 2–10, 2016.
- [105] B. DeMartini, J. Rhoads, S. Shaw, and K. Turner, "A single input–single output mass sensor based on a coupled array of microresonators," *Sensors and Actuators A: Physical*, vol. 137, pp. 147–156, 2007.
- [106] A. Zribi, A. Knobloch, W.-C. Tian, and S. Goodwin, "Micromachined resonant multiple gas sensor," *Sensors and Actuators A: Physical*, vol. 122, pp. 31–38, 2005.

- [107] G. Y. Chen, T. Thundat, E. A. Wachter, and R. J. Warmack, “Adsorption-induced surface stress and its effects on resonance frequency of microcantilevers,” *Journal of Applied Physics*, vol. 77, pp. 3618–3622, 1995.
- [108] T. Thundat, E. A. Wachter, S. L. Sharp, and R. J. Warmack, “Detection of mercury vapor using resonating microcantilevers,” *Applied Physics Letters*, vol. 66, pp. 1695–1697, 1995.
- [109] F. Battiston, J.-P. Ramseyer, H. Lang, *et al.*, “A chemical sensor based on a microfabricated cantilever array with simultaneous resonance-frequency and bending readout,” *Sensors and Actuators B: Chemical*, vol. 77, pp. 122–131, 2001.
- [110] A. Bouchaala, A. H. Nayfeh, N. Jaber, and M. I. Younis, “Mass and position determination in MEMS mass sensors: A theoretical and an experimental investigation,” *Journal of Micromechanics and Microengineering*, vol. 26, p. 105 009, 2016.
- [111] S. J. Martin, V. E. Granstaff, and G. C. Frye, “Characterization of a quartz crystal microbalance with simultaneous mass and liquid loading,” *Analytical Chemistry*, vol. 63, pp. 2272–2281, 1991.
- [112] G. Sauerbrey, “Verwendung von Schwingquarzen zur Wägung dünner Schichten und zur Mikrowägung,” *Zeitschrift für Physik*, vol. 155, pp. 206–222, 1959.
- [113] F. Aydemir and M. A. Ebeoglu, “A QCM sensor array-based electronic tongue with the optimized oscillator circuit using FPGA,” *IEEE Transactions on Instrumentation and Measurement*, vol. 67, pp. 431–438, 2018.
- [114] K. Behera, S. Pandey, A. Kadyan, and S. Pandey, “Ionic liquid-based optical and electrochemical carbon dioxide sensors,” *Sensors*, vol. 15, pp. 30 487–30 503, 2015.
- [115] K. Ishizu, Y. Takei, M. Honda, *et al.*, “Carbon dioxide gas sensor with ionic gel,” *2013 Transducers & Eurosensors XXVII: The 17th International Conference on Solid-State Sensors, Actuators and Microsystems.*, pp. 1633–1636, 2013.
- [116] M. Ramdin, T. W. de Loos, and T. J. Vlugt, “State-of-the-art of CO₂ capture with ionic liquids,” *Industrial & Engineering Chemistry Research*, vol. 51, pp. 8149–8177, 2012.
- [117] N. Bajaj, J. F. Rhoads, and G. T.-C. Chiu, “Characterizing the spatially dependent sensitivity of resonant mass sensors using inkjet deposition,” *Journal of Dynamic Systems, Measurement, and Control*, vol. 139, p. 114 505, 2017.
- [118] H. Zhou, C. Nicholls, T. Kunz, and H. Schwartz, “Frequency accuracy & stability dependencies of crystal oscillators,” *Technical Report SCE-08-12, Carleton University, Systems and Computer Engineering*, Nov. 2008.

- [119] Z. A. Siefker, J. N. Hodul, X. Zhao, *et al.*, “Manipulating polymer composition to create low-cost, high-fidelity sensors for indoor CO₂ monitoring,” *Scientific Reports*, vol. 11, pp. 1–10, 2021.
- [120] D. A. Sarigiannis, “Combined or multiple exposure to health stressors in indoor built environments,” *World Health Organization*, 2014.
- [121] A. Bhide, B. Jagannath, A. Tanak, R. Willis, and S. Prasad, “Carbon dioxide testing suitable for low power microelectronics and IOT interfaces using room temperature ionic liquid platform,” *Scientific Reports*, vol. 10, p. 2557, 2020.
- [122] G. Gerlach, A. Lambrecht, and W. Oelßner, “Analytical methods for the detection of gaseous CO₂,” in *Carbon Dioxide Sensing*. John Wiley Sons, Ltd, 2019, ch. 3, pp. 45–85.
- [123] J. Murray and J. Doe, “Gas chromatography method for traces of carbon dioxide in air,” *Analytical Chemistry*, vol. 37, pp. 941–942, 1965.
- [124] S. Qiao, “A sensitive carbon dioxide sensor based on photoacoustic spectroscopy with a fixed wavelength quantum cascade laser,” *Sensors*, vol. 19, p. 4187, 2019.
- [125] C. Chen, Q. Ren, and Y.-Z. Wang, “Review on multi gas detector using infrared spectral absorption technology,” *Applied Spectroscopy Reviews*, vol. 54, pp. 425–444, 2019.
- [126] T. Vincent and J. Gardner, “A low cost MEMS based NDIR system for the monitoring of carbon dioxide in breath analysis at ppm levels,” *Sensors Actuators B Chemical*, vol. 236, pp. 954–964, 2016.
- [127] B. E. DeMartini, J. F. Rhoads, M. A. Zielke, K. G. Owen, S. W. Shaw, and K. L. Turner, “A single input-single output coupled microresonator array for the detection and identification of multiple analytes,” *Applied Physics Letters*, vol. 93, p. 054 102, 2008.
- [128] V. Kumar, J. W. Boley, Y. Yang, *et al.*, “Bifurcation-based mass sensing using piezo-electrically-actuated microcantilevers,” *Applied Physics Letters*, vol. 98, p. 153 510, 2011.
- [129] J. D. Adams, G. Parrott, C. Bauer, *et al.*, “Nanowatt chemical vapor detection with a self-sensing, piezoelectric microcantilever array,” *Applied Physics Letters*, vol. 83, pp. 3428–3430, 2003.
- [130] A. Gupta, D. Akin, and R. Bashir, “Detection of bacterial cells and antibodies using surface micromachined thin silicon cantilever resonators,” *Journal of Vacuum Science Technology B: Microelectronics and Nanometer Structures Processing, Measurement, and Phenomena*, vol. 22, pp. 2785–2791, 2004.

- [131] A. Gupta, D. Akin, and R. Bashir, “Single virus particle mass detection using microresonators with nanoscale thickness,” *Applied Physics Letters*, vol. 84, pp. 1976–1978, 2004.
- [132] T. Swager, “Sensor technologies empowered by materials and molecular innovations,” *Angewandte Chemie International Edition*, vol. 57, pp. 4248–4257, 2018.
- [133] G.-Z. Xie, T. Kang, Y. Zhou, T. Xie, H.-L. Tai, and Y.-D. Jiang, “QCM sensors based on PEI films for CO₂ detection,” *Journal of Electronic Science and Technology*, vol. 13, pp. 181–187, 2015.
- [134] B. Sun, G. Xie, Y. Jiang, and X. Li, “Comparative CO₂-sensing characteristic studies of PEI and PEI/starch thin film sensors,” *Energy Procedia*, vol. 12, pp. 726–732, 2011.
- [135] S. Meth, A. Goeppert, G. Prakash, and G. Olah, “Silica nanoparticles as supports for regenerable CO₂ sorbents,” *Energy Fuels*, vol. 26, pp. 3082–3090, 2012.
- [136] E. Hampe and D. Rudkevich, “Exploring reversible reactions between CO₂ and amines,” *Tetrahedron*, vol. 59, pp. 9619–9625, 2003.
- [137] M. Ganji, M. Docter, S. Le Grice, and E. Abbondanzieri, “DNA binding proteins explore multiple local configurations during docking via rapid rebinding,” *Nucleic Acids Res*, vol. 44, pp. 8376–8384, 2016.
- [138] P. Oikonomou, “A wireless sensing system for monitoring the workplace environment of an industrial installation,” *Sensors Actuators, B Chem*, vol. 224, pp. 266–274, 2016.
- [139] F. Sutton, “The design of a responsive and energy-efficient event-triggered wireless sensing system,” in *Proc. 14th Int. Conf. Embed. Wirel. Syst. Networks (EWSN 2017)*, 2017, pp. 144–155.
- [140] R. Podoll and K. Irwin, “Sorption of cationic oligomers on sediments,” *Environmental Toxicology and Chemistry*, vol. 7, pp. 405–415, 1988.
- [141] S. Rice, “Human health risk assessment of CO₂: Survivors of acute high-level exposure and population sensitive to prolonged low-level exposure,” *Third Annu. Conf. Carbon Sequestration*, pp. 1–9, 2004.
- [142] Y. Cui, B. Schubert, and A. Jähren, “A 23 m.y. record of low atmospheric CO₂,” *Geology*, vol. 48, pp. 888–892, 2020.
- [143] USDL, “Occupational exposure limits,” *Safety, Occupational and Health Administration, United States Department of Labor*, 2019.

- [144] D. Wang, X. Wang, X. Ma, E. Fillerup, and C. Song, “Three-dimensional molecular basket sorbents for CO₂ capture: Effects of pore structure of supports and loading level of polyethylenimine,” *Catalysis Today*, vol. 233, pp. 100–107, 2014.
- [145] M. Sakwa-Novak, S. Tan, and C. Jones, “Role of additives in composite PEI/oxide CO₂ adsorbents: Enhancement in the amine efficiency of supported PEI by PEG in CO₂ capture from simulated ambient air,” *ACS Applied Material Interfaces*, vol. 7, pp. 24 748–24 759, 2015.
- [146] L. Wang, M. Al-Aufi, C. Pacheco, L. Xie, and R. Rioux, “Polyethylene glycol (PEG) addition to polyethylenimine (PEI)-impregnated silica increases amine accessibility during CO₂ sorption,” *ACS Sustainable Chemistry Engineering*, vol. 7, pp. 14 785–14 795, 2019.
- [147] S. Kobayashi, H. Shirasaka, K.-D. Suh, and H. Uyama, “Viscosity behaviors and gel properties of linear and branched polyethylenimines: Effects of micro-structures,” *Polymer Journal*, vol. 22, pp. 442–446, 1990.
- [148] Y. Takahashi and H. Tadokoro, “Structural studies of polyethers, $-(\text{CH}_2)_m\text{-O-})_n$. X. crystal structure of poly(ethylene oxide),” *Macromolecules*, vol. 6, pp. 672–675, 1973.
- [149] S. Yang, Z. Liu, Y. Liu, and Y. Jiao, “Effect of molecular weight on conformational changes of PEO: An infrared spectroscopic analysis,” *Journal of Materials Science*, vol. 50, pp. 1544–1552, 2015.
- [150] G. Couchaux, D. Barth, M. Jacquin, A. Faraj, and J. Grandjean, “Kinetics of carbon dioxide with amines. I. Stopped-flow studies in aqueous solutions. A review,” *Oil Gas Science and Technology*, vol. 69, pp. 865–884, 2014.
- [151] P. Kortunov, M. Siskin, M. Paccagnini, and H. Thomann, “CO₂ reaction mechanisms with hindered alkanolamines: Control and promotion of reaction pathways,” *Energy Fuels*, vol. 30, pp. 1223–1236, 2016.
- [152] M. Mannan and S. G. Al-Ghamdi, “Indoor air quality in buildings: A comprehensive review on the factors influencing air pollution in residential and commercial structure,” *International Journal of Environmental Research and Public Health*, vol. 18, p. 3276, 2021.
- [153] A. Cincinelli and T. Martellini, “Indoor air quality and health,” *International Journal of Environmental Research and Public Health*, vol. 14, p. 1286, 2017.
- [154] R. R. Scully, M. Basner, J. Nasrini, *et al.*, “Effects of acute exposures to carbon dioxide on decision making and cognition in astronaut-like subjects,” *NPJ microgravity*, vol. 5, p. 17, 2019.

- [155] J. A. Sayers, R. E. Smith, R. L. Holland, and W. R. Keatinge, “Effects of carbon dioxide on mental performance,” *Journal of Applied Physiology*, vol. 63, pp. 25–30, 1987.
- [156] X. Zhang, P. Wargocki, Z. Lian, J. Xie, and J. Liu, “Responses to human bioeffluents at levels recommended by ventilation standards,” *Procedia Engineering*, vol. 205, pp. 609–614, 2017, 10th International Symposium on Heating, Ventilation and Air Conditioning, ISHVAC2017, 19-22 October 2017, Jinan, China.
- [157] A. Collier-Oxandale, J. Thorson, H. Halliday, J. Milford, and M. Hannigan, “Understanding the ability of low-cost MOx sensors to quantify ambient VOCs,” *Atmospheric Measurement Techniques Discussions*, vol. 12, pp. 1–29, 2018.
- [158] J. N. Hodul, A. K. Murray, N. F. Carneiro, *et al.*, “Modifying the surface chemistry and nanostructure of carbon nanotubes facilitates the detection of aromatic hydrocarbon gases,” *ACS Applied Nano Materials*, vol. 3, pp. 10 389–10 398, 2020.
- [159] A. C. Lewis, J. D. Lee, P. M. Edwards, *et al.*, “Evaluating the performance of low cost chemical sensors for air pollution research,” *Faraday Discussions*, vol. 189, pp. 85–103, 2016.
- [160] M. Asri, M. Hasan, Y. Fuaad M.R.A.and Yunos, and M. Ali, “MEMS gas sensors: A review,” *IEEE Sensors Journal*, vol. 21, pp. 18 381–18 397, 2021.
- [161] Z. A. Siefker, A. Boyina, J. E. Braun, *et al.*, “A chemiresistive CO₂ sensor based on CNT-functional polymer composite films,” *Proceedings of IEEE Sensors*, vol. 2020-October, pp. 1–4, 2020.
- [162] S. Herberger, M. Herold, H. Ulmer, A. Burdack-Freitag, and F. Mayer, “Detection of human effluents by a MOS gas sensor in correlation to VOC quantification by GC/MS,” *Building and Environment*, vol. 45, pp. 2430–2439, 2010.
- [163] Y. Lin and Z. Fan, “Compositing strategies to enhance the performance of chemiresistive CO₂ gas sensors,” *Materials Science in Semiconductor Processing*, vol. 107, p. 104 820, 2020.
- [164] A. Molina, V. Escobar-Barrios, and J. Oliva, “A review on hybrid and flexible CO₂ gas sensors,” *Synthetic Metals*, vol. 270, p. 116 602, 2020.
- [165] S. Fanget, S. Hentz, P. Puget, *et al.*, “Gas sensors based on gravimetric detection—A review,” *Sensors and Actuators B: Chemical*, vol. 160, pp. 804–821, 2011.
- [166] E. Dervieux, M. Théron, and W. Uhring, “Carbon dioxide sensing- Biomedical applications to human subjects,” *Sensors*, vol. 22, p. 188, 2022.

- [167] K. Li, J. Jiang, S. Tian, F. Yan, and X. Chen, "Polyethyleneimine-nano silica composites: A low-cost and promising adsorbent for CO₂ capture," *Journal of Materials Chemistry A*, vol. 3, pp. 2166–2175, 2015.
- [168] F. Wang, P. Liu, T. Nie, H. Wei, and Z. Cui, "Characterization of a polyamine microsphere and its adsorption for protein," *International Journal of Molecular Sciences*, vol. 14, pp. 17–29, 2013.
- [169] E. R. Monazam, J. Spenik, and L. J. Shadle, "CO₂ desorption kinetics for immobilized polyethylenimine (PEI)," *Energy and Fuels*, vol. 28, pp. 650–656, 2014.
- [170] C. J. Chiang, K. T. Tsai, Y. H. Lee, *et al.*, "In situ fabrication of conducting polymer composite film as a chemical resistive CO₂ gas sensor," *Microelectronic Engineering*, vol. 111, pp. 409–415, 2013.
- [171] H. Wang, H. Wu, D. Hasan, T. He, Q. Shi, and C. Lee, "Self-powered dual-mode amenity sensor based on the water-air triboelectric nanogenerator," *ACS Nano*, vol. 11, pp. 10 337–10 346, 2017.
- [172] W. Lu, P. Xiao, J. Gu, *et al.*, "Aggregation-induced emission of tetraphenylethylene-modified polyethyleneimine for highly selective CO₂ detection," *Sensors and Actuators, B: Chemical*, vol. 228, pp. 551–556, 2016.
- [173] T. C. Doan, J. Baggerman, R. Ramaneti, H. D. Tong, A. T. Marcelis, and C. J. Van Rijn, "Carbon dioxide detection with polyethylenimine blended with polyelectrolytes," *Sensors and Actuators, B: Chemical*, vol. 201, pp. 452–459, 2014.
- [174] D. S. Karpovich and G. J. Blanchard, "Direct measurement of the adsorption kinetics of alkanethiolate self-assembled monolayers on a microcrystalline gold surface," *Langmuir*, vol. 10, pp. 3315–3322, 1994.
- [175] M. Yoshimoto, T. Matsunaga, M. Tanaka, and S. Kurosawa, "Determination of thermodynamic parameters for enolization reaction of malonic and methylmalonic acids by using quartz crystal microbalance," *Analytical Chemistry Research*, vol. 8, pp. 9–15, 2016.
- [176] B. Wu, K. Wu, P. Wang, and D. M. Zhu, "Adsorption kinetics and adsorption isotherm of poly(N-isopropylacrylamide) on gold surfaces studied using QCM-D," *Journal of Physical Chemistry C*, vol. 111, pp. 1131–1135, 2007.
- [177] V. Stavila, J. Volponi, A. M. Katzenmeyer, M. C. Dixon, and M. D. Allendorf, "Kinetics and mechanism of metal-organic framework thin film growth: Systematic investigation of HKUST-1 deposition on QCM electrodes," *Chemical Science*, vol. 3, pp. 1531–1540, 2012.

- [178] T. Thundat, P. I. Oden, and R. J. Warmack, "Microcantilever sensors," *Microscale Thermophysical Engineering*, vol. 1, pp. 185–199, 1997.
- [179] Y.-l. Su, J. Wang, and H.-z. Liu, "FTIR spectroscopic study on effects of temperature and polymer composition on the structural properties of PEO–PPO–PEO block copolymer micelles," *Langmuir*, vol. 18, pp. 5370–5374, 2002.
- [180] I. Pucić and T. Jurkin, "FTIR assessment of poly(ethylene oxide) irradiated in solid state, melt and aqueous solution," *Radiation Physics and Chemistry*, vol. 81, pp. 1426–1429, 2012.
- [181] S. Arabi, H. Akbari Javar, and M. Khoobi, "Preparation and characterization of modified polyethyleneimine magnetic nanoparticles for cancer drug delivery," *Journal of Nanomaterials*, vol. 2016, pp. 1–6, 2016.
- [182] G. Qi, Y. Wang, L. Estevez, *et al.*, "High efficiency nanocomposite sorbents for CO₂ capture based on amine-functionalized mesoporous capsules," *Energy and Environmental Science*, vol. 4, pp. 444–452, 2011.
- [183] G. Qi, L. Fu, B. H. Choi, and E. P. Giannelis, "Efficient CO₂ sorbents based on silica foam with ultra-large mesopores," *Energy and Environmental Science*, vol. 5, pp. 7368–7375, 2012.
- [184] M. Al Marri, K. Al Saad, M. Saad, D. Cortes, and M. Khader, "Thermodynamics of CO₂ adsorption on polyethyleneimine mesoporous silica and activated carbon," *Journal of Physical Chemistry Biophysics*, vol. 7, pp. 1–5, 2017.
- [185] W. Jung, J. Park, and K. S. Lee, "Kinetic modeling of CO₂ adsorption on an amine-functionalized solid sorbent," *Chemical Engineering Science*, vol. 177, pp. 122–131, 2018.
- [186] S. Satyapal, T. Filburn, J. Trela, and J. Strange, "Performance and properties of a solid amine sorbent for carbon dioxide removal in space life support applications," *Energy and Fuels*, vol. 15, pp. 250–255, 2001.
- [187] F. Liu, S. Chen, and Y. Gao, "Synthesis of porous polymer based solid amine adsorbent: Effect of pore size and amine loading on CO₂ adsorption," *Journal of Colloid and Interface Science*, vol. 506, pp. 236–244, 2017.
- [188] W. Yan, J. Tang, Z. Bian, J. Hu, and H. Liu, "Carbon dioxide capture by amine-impregnated mesocellular-foam-containing template," *Industrial & Engineering Chemistry Research*, vol. 51, pp. 3653–3662, 2012.

- [189] H. Stymne, M. Sandberg, and M. Mattsson, "Dispersion pattern of contaminants in a displacement ventilated room-implications for demand control," in *Proceedings of the 12th AIVC Conference*, Ottawa, Canada, 1991, pp. 24–27.
- [190] G. Pei, D. Rim, S. Schiavon, and M. Vannucci, "Effect of sensor position on the performance of CO₂-based demand controlled ventilation," *Energy Buildings*, vol. 202, p. 109 358, 2019.
- [191] A. Rackes, T. Ben-David, and M. S. Waring, "Sensor networks for routine indoor air quality monitoring in buildings: Impacts of placement, accuracy, and number of sensors," *Science and Technology for the Built Environment*, vol. 24, pp. 188–197, 2018.
- [192] A. Fontanini, U. Vaidya, and B. Ganapathysubramanian, "A methodology for optimal placement of sensors in enclosed environments: A dynamical systems approach," *Building and Environment*, vol. 100, pp. 145–161, 2016.
- [193] D. Yoganathan, S. Kondepudi, B. Kalluri, and S. Manthapuri, "Optimal sensor placement strategy for office buildings using clustering algorithms," *Energy and Buildings*, vol. 158, pp. 1206–1225, 2018.
- [194] Z. J. Zhai and X. Liu, "Principles and applications of probability-based inverse modeling method for finding indoor airborne contaminant sources," *Building Simulation*, vol. 1, pp. 64–71, 2008.
- [195] X. Liu and Z. Zhai, "Protecting a whole building from critical indoor contamination with optimal sensor network design and source identification methods," *Building and Environment*, vol. 44, pp. 2276–2283, 2009.
- [196] T. Zhang, H. Zhou, and S. Wang, "Inverse identification of the release location, temporal rates, and sensor alarming time of an airborne pollutant source," *Indoor Air*, vol. 25, pp. 415–427, 2015.
- [197] L. Zeng, J. Gao, L. Lv, *et al.*, "Markov-chain-based inverse modeling to fast localize hazardous gaseous pollutant sources in buildings with ventilation systems," *Building and Environment*, vol. 169, p. 106 584, 2020.
- [198] Y. A. Prabowo, R. Ranasinghe, G. Dissanayake, B. Riyanto, and B. Yulianto, "A Bayesian approach for gas source localization in large indoor environments," in *2020 IEEE/RSJ International Conference on Intelligent Robots and Systems (IROS)*, 2020, pp. 4432–4437.

- [199] T. Wiedemann, D. Shutin, and A. J. Lilienthal, “Model-based gas source localization strategy for a cooperative multi-robot system—A probabilistic approach and experimental validation incorporating physical knowledge and model uncertainties,” *Robotics and Autonomous Systems*, vol. 118, pp. 66–79, 2019.
- [200] K. Kamarudin, A. Y. M. Shakaff, V. H. Bennetts, *et al.*, “Integrating SLAM and gas distribution mapping (SLAM-GDM) for real-time gas source localization,” *Advanced Robotics*, vol. 32, pp. 903–917, 2018.

VITA

Zachary A. Siefker received his B.S. and M.S. degrees in mechanical engineering from the University of Dayton in 2017 and 2018, respectively. While there, Zachary worked in the Industrial Assessment Center, researching and consulting on energy efficient manufacturing. Following this, Zachary joined Purdue University's Ray W. Herrick Laboratories where his research focused on gas sensors for building applications, which included: the development of novel gas sensors, gas sensor evaluation protocols, and the integration of gas sensors in the built environment. Zachary is also involved in the ASHRAE and IEEE technical communities where his interests lie at the intersection of smart-connected technologies and energy efficiency.